WASM: Minerals, Energy and Chemical Engineering

Hydrodynamics of Bubbling Fluidized Bed

Vaibhav Agrawal

This thesis is presented for the Degree of

Doctor of Philosophy

of

Curtin University

November 2018

Declaration

To the best of my knowledge and belief this thesis contains no material previously published by any other person except where due acknowledgment has been made. This thesis contains no material which has been accepted for the award of any degree or diploma in any university.

Signature : Vaibhav

Date : 15 MAY 2019

Author's Biography

Vaibhav Agrawal completed his bachelor in chemical engineering from Vellore Institute of Technology, Vellore in 2010. Then after, he worked in Tata Consultancy Services as a system engineer for two years and subsequently went to pursue master in chemical engineering from Malaviya National Institute of Technology, Jaipur in 2012. After completing his master degree in 2014, he commenced Ph.D. study in the department of chemical engineering at Curtin University, Western Australia. His research interest includes computational and experimental investigation of multiphase flows in process systems. His research has already been acknowledged by peer-reviewed journals and conference publications, which are listed below.

Journal publications:

1) V. Agrawal, Y.H. Shinde, M.T. Shah, R.P. Utikar, V.K. Pareek, J.B. Joshi, Estimation of Bubble Properties in Bubbling Fluidized Bed Using ECVT Measurements, Industrial Engineering & Chemistry Research 57 (2018) 8319–8333.
2) V. Agrawal, Y.H. Shinde, M.T. Shah, R.P. Utikar, V.K. Pareek, J.B. Joshi, Effect of drag models on CFD–DEM predictions of bubbling fluidized beds with Geldart D particles, Advanced Powder Technology 29 (2018), 2658–2669.
3) V. Agrawal, M.T. Shah, R.P. Utikar, V.K. Pareek, J.B. Joshi, Effect of Initial Bed Condition on Mixing of bi-Dispersed Solids in Bubbling Fluidized Bed. *To be submitted*

Conference proceedings:

1) V. Agrawal, M.T. Shah, R.P. Utikar, V.K. Pareek, CFD–DEM simulations of mixing of bi–dispersed solids in biomass fluidized bed, Proceedings of 25th International Symposium on Chemical Reaction Engineering Conference, Florence, Italy (2018).
2) V. Agrawal, Y.H. Shinde, M.T. Shah, R.P. Utikar, Estimation of Bubble Size in Bubbling Fluidization using ECVT Measurement, Proceedings of 1st One Curtin International Postgraduate Conference, Miri, Malaysia (2017).

Abstract

Many industrial processes such as pyrolysis, gasification, polymerization, combustion, drying, etc. employ gas-solid bubbling fluidized beds (BFBs), where mixing between the two phases and/or different type and size of solids is a critical parameter that governs the performance. The present research investigates gas-solid hydrodynamics in BFBs having mono- and bi-dispersed solids by conducting both computational fluid dynamic (CFD) simulations and experiments. Effect of drag models on the predictions of CFD–DEM (discrete element model) simulations and the effect of initial bed configuration on the predictions of mixing/segregation of solids in a bi-dispersed BFB were investigated using CFD simulations while bubble properties were experimentally measured using electrical capacitance volume tomography (ECVT).

The study on the effect of drag models revealed that out of six different drag models, none was able to predict the flow properties at different flow conditions consistently. The Di Felice model and Ayeni model reasonably predicted the mean values of flow properties. However, a wide discrepancy in the predictions of granular temperature was observed. The study on the effect of initial bed configuration on the mixing of two solids showed that an initial bed configuration does not affect the steady-state mixing achieved after a reasonably long time. However, initial bed configurations significantly affect the time required to achieve the steady-state mixing. The experimental study using ECVT was conducted to determine the equivalent diameter, rise velocity and frequency of bubbles in a 3D flow domain. A new post-processing algorithm was developed to determine an optimum threshold that distinguished the bubble phase from the emulsion phase, and subsequently, this algorithm was used for calculations of bubble properties.

In summary, the major contributions of this thesis are (i) the investigation of wide spectrum of drag model and recommendation for drag models that resulted in better predictions, (ii) understanding the role of initial bed condition on mixing of bi-dispersed solids, and (iii) accurate measurement of bubble properties using non-invasive ECVT technique.

Acknowledgment

First and foremost, I would like to express my gratitude towards my supervisors Prof. Vishnu K Pareek, Dr. MilinKumar T Shah, Dr. Ranjeet P Utikar, and Prof. Jyeshtharaj B Joshi for showing faith in my potential and giving me this opportunity. It was their support and motivation that allowed me to work on this project and nurtured me as an independent researcher. They helped me in developing the research aptitude and analyzing the complex problems using simple and systematic approach.

My Ph.D. would not have sailed through so easily without the support of Dr. Yogesh H Shinde, Dr. Shambhu S Rathore and Adhirath S Wagh, who guided me during my early days as a researcher and provided a homely and friendly environment.

I owe a lot to the technical support team of chemical engineering department namely Araya, Jimmy, Andrew and Ross for their support in my experiments. I would also like to thank the admin staffs, Evelyn, Lemlem, and Randall, for their assistance and also the Curtin Safer community team for escorting me home during late night hours. I would also like to acknowledge the financial assistance (CIPRS) provided by the department of chemical engineering, Curtin University and computational resource provided by the Pawsey supercomputing center.

Above all, I am indebted to my parents and sisters who have provided me their unequivocal support and motivation throughout my student life. I would like to thank my colleagues and friends especially Sakshi Tiwari and Divya Bhatt for being my strength and bearing my frustration during the final phase of my research.

Table of Contents

List of figures

List of tables

Nomenclature

a	Tuning parameter of Syamlal–O'Brien drag model (-)
A	Area (m^2)
A_p	Projected surface area of a particle (m^2)
b	Tuning parameter of Syamlal–O'Brien drag model (-)
B	Thickness (m)
C	Concentration of flotsam/jetsam particles (kg/m^3)
CF	Correction factor (-)
$C_{D,H}$	Drag coefficient for a single particle in a multi-particle system (-)
$C_{D,\infty}$	Drag coefficient for a single isolated particle in infinite domain (-)
d	Diameter (m)
D	Dispersion coefficient (m^2/s)
$\overline{\overline{D_G}}$	Strain rate tensor (s^{-1})
e	Coefficient of restitution (-)
f_b	Bubble frequency (s^{-1})
$\boldsymbol{f}_D$	Drag force on a single isolated particle in infinite domain ($kg{\cdot}m/s^2$)
$\boldsymbol{f}_{D,H}$	Drag force on a single particle in a multi-particle system ($kg{\cdot}m/s^2$)
$\boldsymbol{F}_C^{(i)}$	Net contact force as a result of contact with another particle ($kg{\cdot}m/s^2$)
$\boldsymbol{F}_D$	Total drag force on all particles in a unit control volume ($kg{\cdot}m/s^2$)
$\boldsymbol{F}_d^{(ij)}$	Dashpot force between the i^{th} and j^{th} particles ($kg{\cdot}m/s^2$)
$\boldsymbol{F}_s^{(ij)}$	Spring force between the i^{th} and j^{th} particles ($kg{\cdot}m/s^2$)
$\boldsymbol{F}_T^{(i)}$	Net sum of all forces acting on the i^{th} particle ($kg{\cdot}m/s^2$)
$\boldsymbol{g}$	Acceleration due to gravity (m/s^2)
h	Axial height (m)
$\langle h_p \rangle_{bed}$	Average particle height (m)
H	Bed height (m)
$I^{(i)}$	Moment of inertia of the i^{th} particle ($kg{\cdot}m^2$)
$\boldsymbol{I}_{GS}$	Momentum transfer between gas and solid phases ($kg/m^2{\cdot}s^2$)
J	Time interval (-)
k´	Time interval at which cross-correlation is maximum (-)
k	Spring stiffness coefficient (kg/s^2)
L	Length (m)
$L^{(i)}$	Distance of the contact point from the center of the i^{th} particle (m)
M	Number of samples in cross-correlation function (-)
$m^{(i)}$	Mass of the i^{th} particle (kg)
m_{eff}	Effective mass (kg)
N	Number of sample interval (-)
N_c	Number of times a signal passes over its mean (-)
N_p	Number of particles (-)
P_G	Gas phase pressure ($kg/m{\cdot}s^2$)
R	Cross – correlation function (-)
Re_P	Particle Reynolds number (-)
$\bar{\bar{S}}_G$	Gas phase stress tensor ($kg/m{\cdot}s^2$)
t_n^{col}	Collision time between two particles (s)
T	Time (s)
$\boldsymbol{t}^{(ij)}$	Tangent to the plane of contact between the i^{th} and j^{th} particles (-)

T	Total sampling period (s)
$\boldsymbol{T}^{(i)}$	Sum of all torques acting on the i^{th} particle (kg·m^2/s^2)
$\boldsymbol{u}$	Local linear velocity (m/s)
$\boldsymbol{U}_G$	Inlet gas velocity (m/s)
$\boldsymbol{U}_{mf}$	Minimum fluidization gas velocity (m/s)
U_{slip}	Slip velocity (m/s)
V_p	Volume of a single particle (m^3)
$\boldsymbol{X}$	Particle location (-)
x, y, z	x, y and z direction in Cartesian coordinate system (Figure 3.2)

Greek letters

β	Gas - solid momentum exchange coefficient (kg/s)
Δ	Sampling interval (s)
δ_n	Normal overlap between particles (m)
δ_t	Tangential displacement (m)
ϵ	Volume fraction (-)
$\eta^{(ij)}$	Unit vector along the line of contact pointing from particle i to particle j (-)
η	Damping coefficient (kg/s)
λ_G	Second coefficient of viscosity of the gas phase (kg/m·s)
μ_G	Dynamic viscosity of gas (kg/m·s)
ν	Coefficient of friction (-)
$\omega^{(i)}$	Angular velocity of the i^{th} particle (rad/s)
ρ	Density (kg/m^3)
τ	Time lag (s)
$\overline{\overline{\tau_G}}$	Gas phase shear stress tensor (kg/m·s^2)
θ	Granular temperature (m^2/s^2)
$\vartheta^{(k)}$	Volume of k^{th} cell (m^3)

Subscripts

0	Initial condition (at time = 0)
Ayeni	Ayeni drag model
B	Bubble
Bed	Fluidized Column
Biomass	Biomass particles
BVK	Beetstra–van der Hoef–Kuipers drag model
Calc	Calculated from image analysis
calibration	Calculated from equation (1) in Chapter 5
c/s	Cross section
C	Contact force
d	Dashpot
D	Drag Force
DallaValle	DallaValle drag coefficient
Di Felice	Di Felice drag model
EMMS	EMMS drag model
Ergun	Ergun drag model
flotsam	particles that tend to accumulate on the top
G	Gaseous phase
Gidaspow	Gidaspow drag model

H	Hindered flow condition
I	Time interval number
jetsam	particles that tend to sink at the bottom of the bed
mb	Minimum bubbling condition
mf	Minimum fluidization condition
ms	Minimum slug flow condition
N	Properties in normal direction
p	Solid particle
s	Spring
S	Solid phase
S-B	Syamlal–O'Brien drag model
Sand	Sand particles
T	Properties in tangential direction
tr	Turbulent flow regime
Wen-Yu	Wen and Yu drag model

Superscripts

i	i^{th} particle
j	j^{th} particle
ij	i^{th} and j^{th} particle pair
k	k^{th} cell
$i \in k$	i^{th} particle residing in k^{th} cell

Abbreviations

2D	Two Dimensional
3D	Three Dimensional
ART	Algebraic Reconstruction Technique
BFB	Bubbling Fluidized Bed
BSD	Bubble Size Distribution
BVK	Beetstra–van der Hoef–Kuipers
CC	Cross- correlation
CF	Correction Factor
CFD	Computational Fluid Dynamics
CLC	Chemical Looping Combustion
DIAT	Digital Image Analysis Techniques
DEM	Discrete Element Model
DNS	Direct Numerical Simulation
DPM	Discrete Particle Model
DQMOM	Direct Quadrature Method of Moment
ECT	Electrical capacitance tomography
ECVT	Electrical capacitance volume tomography
EE	Eulerian–Eulerian
EL	Eulerian–Lagrangian
EMMS	Energy Minimization Multi-Scale
FCC	Fluid Catalytic Cracking
GenIDLEST	Generalized Incompressible Direct and Large Eddy Simulation of Turbulence
HKL	Hill–Koch–Ladd
KTGF	Kinetic Theory of Granular Flow
LBP	Linear Back Propagation

LI	Landweber Iteration
LLDPE	Linear Low-Density PolyEthylene
MFiX–DEM	Multiphase Flow with interphase eXchange–Discrete Element Model
MPT	Magnetic Particle Tracking
MRI	Magnetic Resonance Imaging
MSD	Mean Square Displacement
NETL	National Energy Technology Laboratory
NN-MOIRT	Neural Network Multi-criteria Optimization Image Reconstruction Technique
PCM	Particle Centroid Method
PEPT	Positron Emission Particle Tracking
PIV	Particle Image Velocimetry
PSD	Power Spectral Density
PSD´	Particle Size Distribution
PSN	Particle Segregation Number
RMS	Root Mean Square
RPT	Radioactive Particle Tracking
SIRT	Simultaneous Iterative Reconstruction Technique
TFM	Two Fluid Model
TRP	Tikhonov Regularization Principle
TV-IST	Total Variation Iterative Soft Thresholding

1 Introduction

1.1. Introduction

Gas-solid bubbling fluidized beds (BFBs) are used in many industrial processes such as pyrolysis, chemical looping combustion (CLC), polymerization, refining, etc. The performance of BFBs largely depends on the extent of mixing between gas and solid phases. For example in fast pyrolysis, biomass is fluidized with sand as an inert agent that retains and passes the supplied heat to the continuously fed biomass. The heat transfer between the sand and biomass governs the extent of pyrolysis and type of products. The uniform temperature distribution and a higher rate of heat transfer can only be achieved by good mixing between sand and biomass [1]. Another example is a fluidized bed polymerization reactor, where gaseous ethylene monomer polymerizes at the interfacial boundary of the solid Ziegler–Natta catalyst and polymer particle [2]. The polymerization process depends on the contact area between gas-solid and solid–solid phases. Contact area between gas and solid phase in any processes involving BFBs, therefore, determines the efficiency of the process. The contact area between the phases, in turn is determined by the gas-solid hydrodynamics. Hence, the efficiency of any process in a BFB depends on the gas-solid hydrodynamics.

1.2. Gas-solid flow in BFB

Figure 1.1 shows a schematic diagram of a BFB. As the gas fluidizes a solid bed, small bubbles are initially formed near the distributor. These small bubbles coalesce while moving upwards and form bigger bubbles. As size of the bubbles increases, they become unstable and split. During the rise of bubbles, particles above the roof of bubbles move upward due to the push experienced by them, while the wake of bubbles carries the particles with itself. At the time of bubble eruption, the particles at the top

of the bubbles are thrown radially outwards towards the walls [3–6]. These particles then flow down towards the bottom of the bed. The bubble coalescence, breakup, eruption and resultant movements of particles are unique flow characteristics of dense gas-solid flow in BFB, and they result in rigorous mixing with higher contact area between gas and solids.

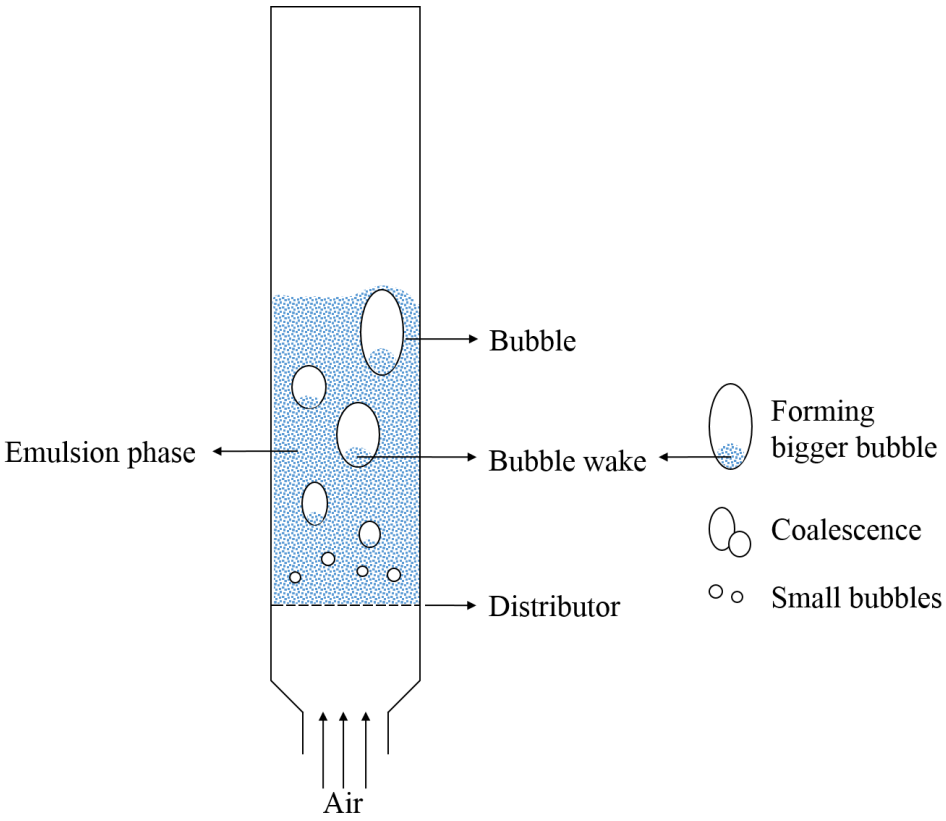

Figure 1.1 Schematic diagram of a BFB

The typical design procedure of a BFB assumes the gas-solid flow as a combination of two pseudo phases, i.e., emulsion and bubble phases. The interactions between the pseudo phases are modeled by considering the flow of these phases as either a plug or mixed flow [7]. The models determine the exchange of mass, momentum, and heat between the bubble and emulsion phase and as a result, helps in theoretical designing of a fluidized bed reactor. The bubble phase is quantified by calculating the bubble properties using the empirical correlations available in the literature. A number of

empirical correlations [8–12] have been proposed to calculate the bubble size and velocity. Figure 1.2(a) and (b) shows bubble diameter and velocity calculated using available empirical correlations for operating condition of $d_{p,Sand}$ = 320 μm, d_{bed} = 20 cm and $\mathbf{U}_G$ = 10.73 cm/s. These empirical correlations can predict the monotonic increase of bubble properties with bed height. However, variation in the bubble diameter and velocity profiles calculated using different empirical correlations is widespread, with bubble diameter ranging from 2.5 cm to 7.5 cm and bubble velocity ranging from 40 cm/s to 90 cm/s at given operating conditions and particle properties. The variation in the calculated bubble properties using different empirical correlations can be attributed to several shortcomings of experimental studies. For example, the majority of experiments have been performed in pseudo-2D columns [13–16], where the removal of the azimuthal dimension affects the flow pattern and consequently, the bubble properties. Geldart [17] found that the bubble diameter measured in a 3D column was much higher than that measured in a 2D column. The invasive probes, such as optical, resistance, capacitance probes, were mostly used [18–21] to measure the bubble properties. The presence of the probe during the measurement affects the local flow behavior [22]. The non–invasive techniques are better alternatives as they can be used in 3D columns and do not affect the local hydrodynamics during the measurements.

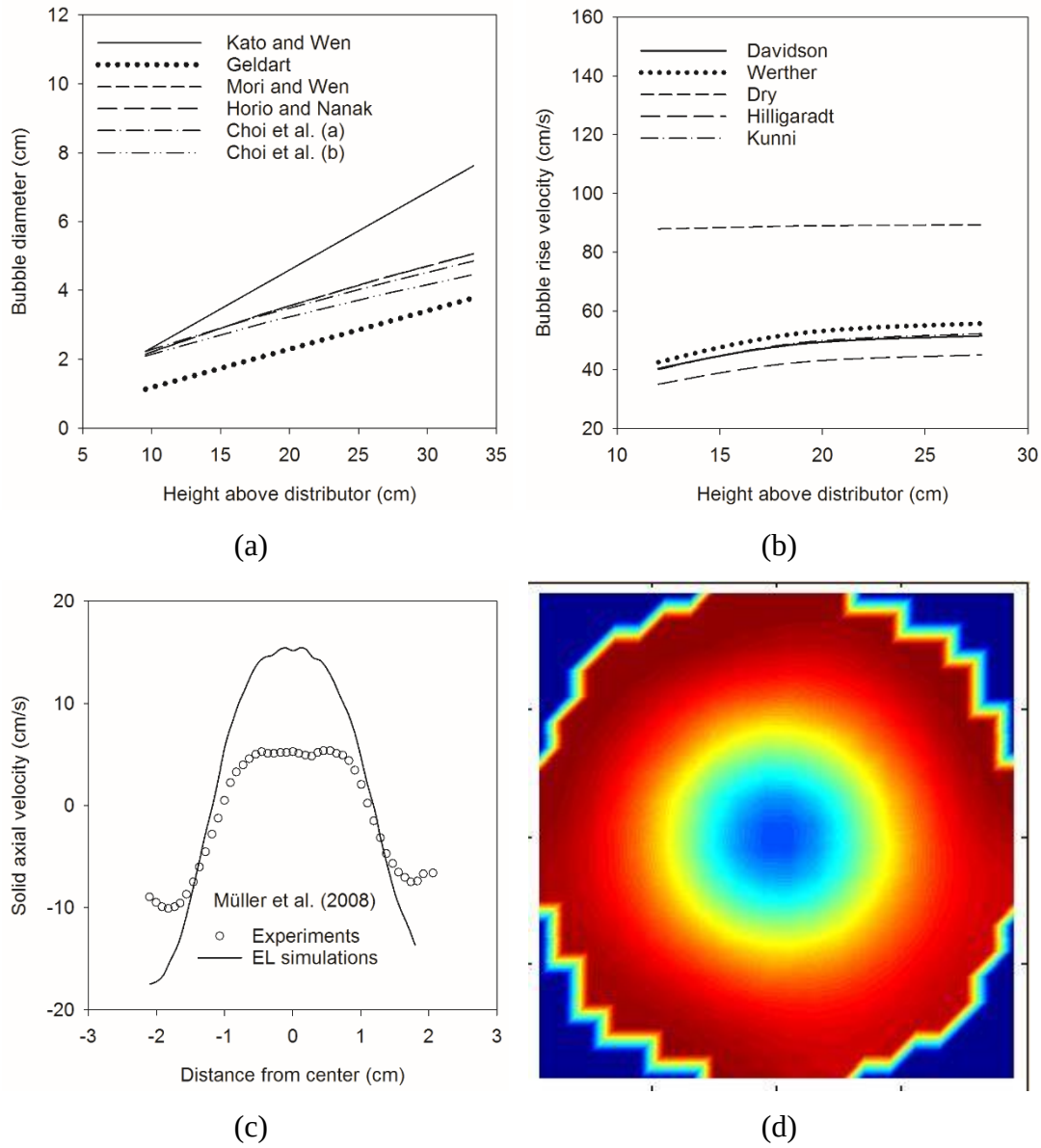

Figure 1.2 (a), (b) Bubble diameter and rise velocity ($d_{p,Sand}$ = 320 μm, $\mathbf{U}_G$ = 10.73 cm/s), (c) Solids axial velocity (d_p = 1200 μm, ρ_p = 1 gm/cm^3, $\mathbf{U}_G$ = 90 cm/s), (d) ECVT tomograph of solids volume fraction (■ - solids and ■ - gas)

The emulsion phase, on the other hand, is characterized by the solids volume fraction distribution inside the bed. The distribution of solids volume fraction depends on operating gas velocity and particle size distribution. Moreover, if a bed has more than one type of solids, mixing and segregation of the solid phases is also important for characterization of the emulsion phase. The mixing or segregation of solids depends on particle size and density, gas fluidizing velocity, initial bed configurations etc.

Several studies have investigated bi-dispersed BFB to study the effect of these parameters on the extent of mixing [23–29] and have determined that the extent of mixing increases at higher gas flow rate [25,27]. These previous studies [23–29] have measured the extent of mixing using either high speed imaging, or x-ray tomography, or electrical capacitance volume tomography or by just sieving the solids phases. They have reported the steady state or time averaged values of solids volume fraction and/or extent of mixing in a bi-dispersed BFB. Moreover, only few studies [23,30,31] have discussed the effect of hydrodynamic forces or bubbling phenomena on mixing. Consequently, to thoroughly understand the mixing process and the factors affecting it, a time tested strategy is required, which can calculate the mixing at steady and transient state. Computational fluid dynamics (CFD) is a promising and cost-effective strategy to study the hydrodynamics of bi-dispersed BFB. CFD simulations can resolve the individual solid phases and gas phase and therefore, can give us the insight of BFBs.

Computational fluid dynamics (CFD) has been extensively used to study the gas-solid flow in BFBs as it offers the advantage of performing an endless number of trials to evaluate the alternate design configuration and operating conditions. It can also effectively resolve the multiscale and multiphase nature of the gas-solid flow in a BFB [32–35]. In a CFD model of BFB, gas is generally considered as a continuum phase whereas solids are modeled as either continuum or discrete [36]. In Eulerian-Lagrangian (EL) model, commonly known as CFD–discrete element method (CFD–DEM), actual solid particles are tracked, and therefore, EL is more realistic and requires closures for gas-solid interactions only. The solid-solid collision force is determined by the spring-dashpot model given by Cundall and Strack [37]. Figure 1.2 (d) compares the radial profile of the solids axial velocity predicted by the EL

simulations and that measured by the magnetic resonance imaging (MRI) experiments [38]. Qualitative trend obtained by the simulations and experiments are similar, however quantitatively, the simulations overpredicted the solids axial velocity. Such discrepancies between the predictions and experiments are observed in several previous studies. This type of discrepancies can be attributed to the closure model used to model the gas-solid interactions or the selection of drag force model, which is the most dominant closure in the gas-solid CFD-DEM model of a BFB. A number of drag models have been proposed in the literature [39–44], and the selection of a drag model is critical to BFB simulations. Consequently, the impact of drag models on the hydrodynamic predictions of BFB has been extensively studied [33,44–50]. Most of these studies have used the Eulerian-Eulerian (EE) simulation, while few studies [44,48,49,51] used the CFD–DEM model. Despite several studies, the origin of discrepancies in CFD predictions arising from the use of different drag models is largely unknown. As a result, the selection of drag models often depends on a trial and error.

1.3. **Motivation and contribution**

BFBs have been investigated by both computationally and experimentally to understand pressure fluctuations, holdup profiles, bubble properties and mixing/segregation in bi-dispersed bed. However, very few studies have been conducted on measurement of bubble properties, particularly the bubble diameter. Moreover, steady state mixing in bi-dispersed BFBs has been reported repeatedly. However, transient behaviour of bi-dispersed bed leading to mixing of solids of different types, and sizes have not been thoroughly investigated. The current research therefore focuses on the measurement of bubble diameter and unsteady behaviour of mono and bi-dispersed beds. Three different studies have been conducted, i.e., (i)

measurement of bubble properties, (ii) gas-solid hydrodynamics in mono-dispersed BFBs and (iii) mixing and segregation in bi-dispersed BFBs. Motivations of each study are summarized below.

1) The complex nature of gas-solid BFBs and unavailability of high precision sensor has restricted the previous studies to 2D experiments. These previous studies have conducted experiments in either 2D column or processed a slice of 3D column or captured the data using probes. Very few studies have been conducted the measurements of bubble properties using non–invasive techniques in a 3D cylindrical column. However, non–invasive techniques have either low spatial or temporal resolution and therefore, cannot clearly capture discrete bubbles. For instance, solids volume fraction contours obtained from electrical capacitance volume tomography (ECVT) is shown in Figure 1.2 (d), which shows the gradual transition of the bubble phase to the emulsion phase. A cut–off value of solids volume fraction, also referred to as a threshold, is therefore required to distinguish bubble and emulsion phase and subsequently to determine the bubble size. Different studies [52–55] have used different threshold values, and there is no clear guideline for the selection of a particular value. The selection of different thresholds results in wide variation in bubble diameter measurements. Consequently, a methodology to calculate a threshold solids volume fraction to separate the bubble and emulsion phase is required.
2) The previous studies in bi-dispersed BFBs have measure the mixing or segregation in a collapsed bed system. In collapsed bed, air supply is suddenly switched off and the solids holdup and extent of mixing is calculated at this condition using either non-invasive technique or sieving. This method can only be used to measure the steady state value and moreover, measurement of mixing using this method is

affected by the way sample is collected [24]. Consequently, investigation of mixing in bi-dispersed BFB under the dynamic condition is required to obtain the transient nature of mixing or segregation from the initially segregated or mixed bed configuration. The effect of operating and system parameters on the transient nature and on the extent of mixing is also required to fundamentally understand the mixing process.

3) EL or CFD-DEM is a promising and more realistic simulation methodology to study the complex multiscale nature of mono- and bi-dispersed BFBs. EL simulations offers many advantages such as tracking of individual particles and closure model for darg force is only required. Despite these advantages, hydrodynamic predictions from EL simulations, similar to EE simulations, are also impacted by the different drag models available in the literature. This requires a thorough understanding of origin of discrepancies in drag models and their impact in predictions of gas-solid flow in mono- and bi-dispersed BFBs. To comprehensively validate the CFD–DEM model, comparison of not only the mean values but also the fluctuating part of velocity and pressure drop is required. Prediction of fluctuating components (such as granular temperature) helps in understanding the chaotic and heterogeneous nature of BFB.

To address the shortcomings of the previous studies, the present work has undertaken three substudies that are explained as follows.

1) Effect of drag models (Chapter–3): CFD–DEM model was used to simulate two different BFB systems as explained in Goldschmidt et al. [13] and NETL challenge problem[56]. The effect of different gas-solid drag models on CFD–DEM predictions was investigated. It was found that none of the drag models were able to consistently predict the flow parameters especially the fluctuating components

under different flow conditions. The inherent differences in the drag models were analyzed, the discrepancy in the flow predictions from each drag model was quantified, and suitable drag models for BFB simulations were recommended.

2) Effect of initial bed configuration on mixing of solids (Chapter–4): The mixing/segregation behavior, in light of different initial bed conditions and the formation of bubbles, were studied in a bi–dispersed BFB containing sand and biomass using CFD–DEM simulations. Different initial segregated configurations of solids were simulated to determine the extent and time of mixing. Though particle configuration did not affect the extent of mixing, the mixing time varied significantly.
3) Measurement of bubble properties using ECVT (Chapter–5): A post-processing algorithm to determine the optimal threshold value that takes into consideration of the gradual transition of bubble to emulsion phase and "soft–field" limitation of ECVT was developed. This algorithm was used to calculate the bubble diameter from ECVT images. Moreover, the behavior 3D bubbles comprising of coalescing, propagation and splitting of bubbles was also investigated.

A thesis layout describing the chapter-wise inclusions is shown in Figure 1.3.

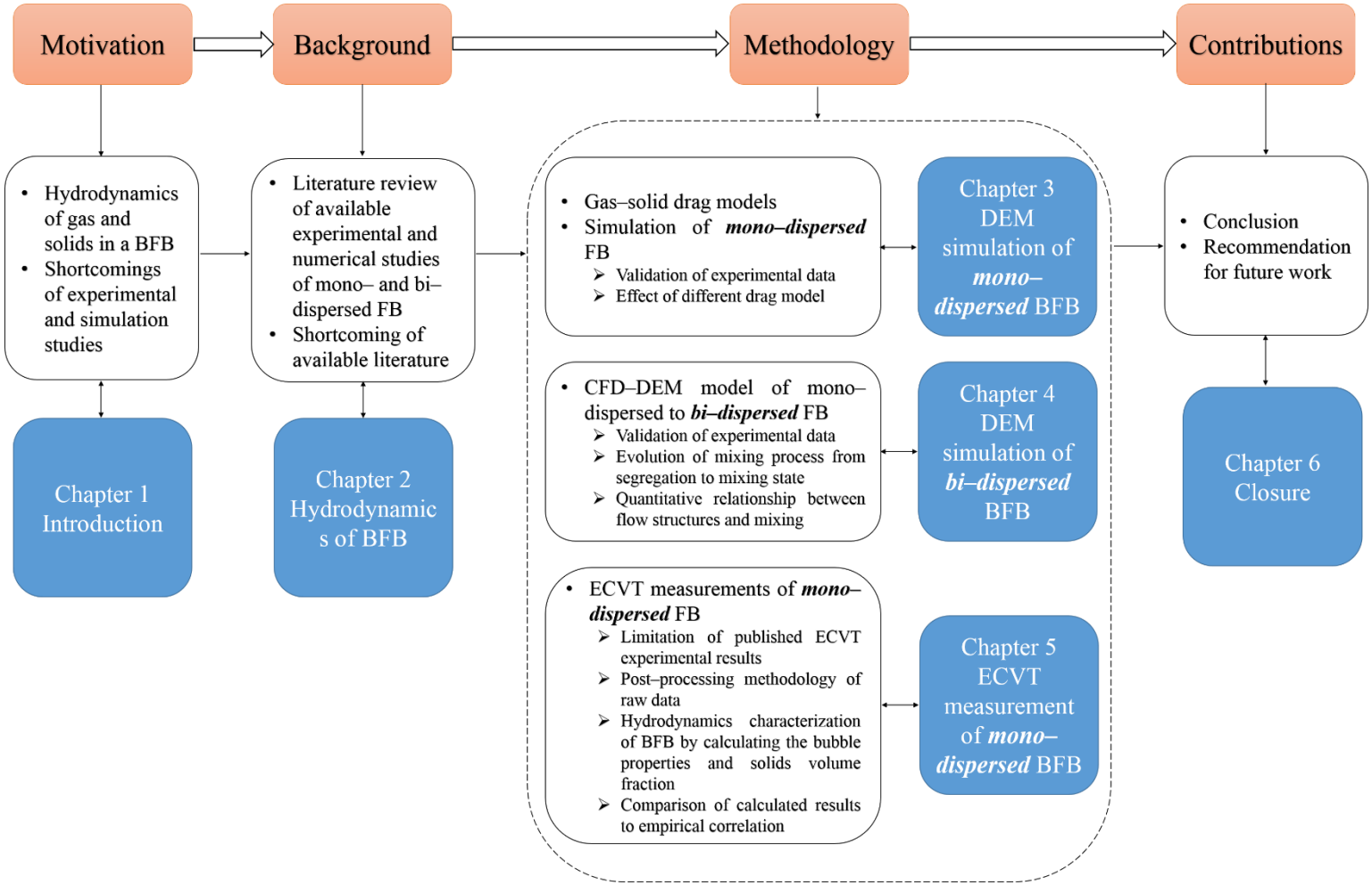

Figure 1.3 Thesis layout

2 Hydrodynamics of Bubbling Fluidized Bed

2.1. Introduction

Fluidization is a process in which solids are caused to behave like a fluid by blowing gas or liquid upwards through the solid-filled reactor. This “fluid-like” behavior of solids results in excellent solid-solid and gas-solid mixing and as a result, fluidization is used in many industrial applications such as in catalytic polymerization of ethylene [2], or in pyrolysis and drying of particles [57].

The performance of a fluidized bed is determined by the flow behavior of gas and solid phases. Different flow regimes such as bubbling, slugging or turbulent fluidization can occur, and each regime results in unique mixing patterns. For example, bubbling phenomena appears in a fluidized bed at a low inlet gas velocity, and results in rigorous mixing of the two phases. The slug flow which appears at a high gas velocity, results in bubbles having a diameter comparable to column diameter, which consequently results in very poor mixing [58]. It is therefore important to understand different flow regimes.

2.2. Fluidization regimes

The flow pattern in the fluidized bed is broadly classified as particulate (smooth) and aggregative (bubbling) [59]. In Particulate fluidization, the solids usually expand uniformly inside the bed. Aggregative fluidization, on the other hand, is characterized by the non–uniform expansion of bed due to the occurrence of bubbles. Aggregative fluidization is further classified as bubbling, slugging, and turbulent as shown in Figure 2.1 and briefly described in Table 2.1.

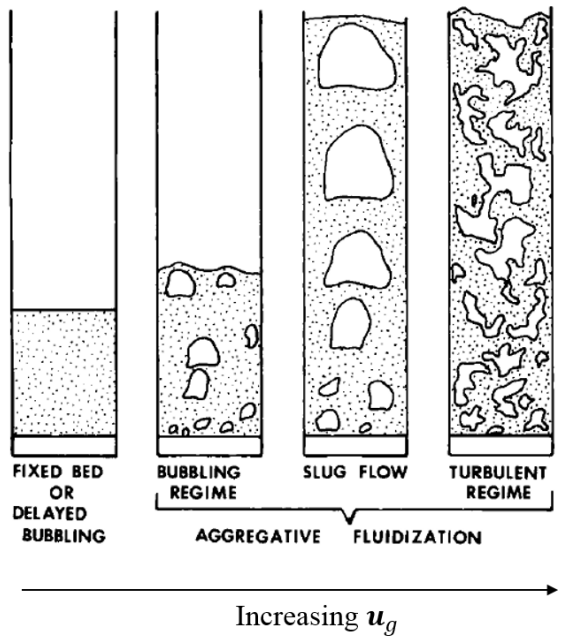

Figure 2.1 Different flow regimes in fluidized beds [60]

Table 2.1 Description of different flow regimes [59]

Velocity range	Fluidization regime	Fluidization feature and appearance
$0 < U_G < U_{mf}$	Fixed bed	Gas flow through the interstice without moving the stationary particles
$U_{mf} \leq U_G < U_{mb}$	Particulate/ homogeneous regime	Bed expands smoothly with the well-defined bed surface
$U_{mb} \leq U_G < U_{ms}$	Bubbling regime	Gas bubbles similar to boiling liquid are formed which promote solids mixing
$U_{ms} \leq U_G < U_{mc}$	Slug flow regime	Bubble size approaches bed diameter
$U_{mc} \leq U_G < U_{tr}$	Turbulent regime	Irregular movement of small bubbles and particle clusters with continuously changing velocity.

Different research groups have studied the transition of fluidization regimes from fixed to fast fluidization with an increase in superficial velocity. Svensson et al. [61] measured the pressure

fluctuation in a rectangular cross-sectional area reactor and analyzed the frequency of the pressure signals to determine the three bubbling regimes – single, multiple and exploding. Bai et al. [62] on the other hand, analyzed the standard deviation of the pressure fluctuations signal measured in a cylindrical column and for two different particles – fluid catalytic cracking (FCC) catalyst and silica sand. Bai et al. [62] obtained four fluidization regime – bubbling, turbulent, fast fluidization and pneumatic conveying. Makkawi and Wright [63] provided the pictorial description of different fluidization regimes using electrical capacitance volume tomography (ECVT). Lim et al. [64] reviewed the work published in gas fluidization and gave a comprehensive regime map which is a function of dimensionless superficial velocity and Archimedes number as shown in Figure 2.2.

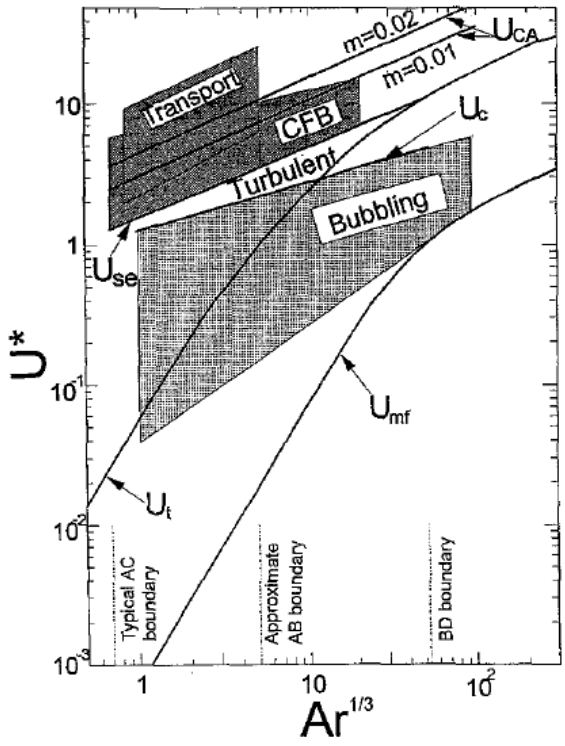

Figure 2.2 Dimensionless regime diagram [64]

2.3. **Geldart classification of solids**

Archimedes number used in Figure 2.2 is a function of particle properties. Therefore, Particle size and density play a critical role in determining the flow pattern of the fluidized bed. Geldart [65] classified the solids into four groups namely–A, B, C, and D (Table 2.2). Further work was then carried out to extend/modify the Geldart boundaries and Grace [60] reviewed and defined three new boundaries–AB, BD and CA where AB means the boundary between group A and B of Geldart classification and so on.

Table 2.2 Geldart classification of powder [65]

Geldart classification	Bed particle properties
Group A	Bed particles expand homogeneously after minimum fluidization condition and gas bubbles start appearing at the minimum bubbling velocity ($\boldsymbol{U}_{mb}$>$\boldsymbol{U}_{mf}$).
Group B	Gas bubbles appear at the minimum fluidization ($\boldsymbol{U}_{mb}$=$\boldsymbol{U}_{mf}$).
Group C	The bed particles are cohesive and difficult to fluidize.
Group D	Scalable spouted bed can be easily formed in this group of powders.

2.4. **Mono–dispersed BFB**

Knowledge of flow pattern and powder classification are the prerequisite to understand the hydrodynamics of a fluidized bed reactor. The focus of this thesis is to study the hydrodynamics of bubbling fluidized bed for Geldart B or D classification and hereafter; all the discussion will be based on the gas-solid bubbling fluidized bed for Geldart B or D.

As described in Table 2.1, the fluidized bed is classified as a BFB, when the gas from the bottom of the column flows in the form of bubbles. Small bubbles are formed at the bottom, and as they move up, they coalesce with the other neighboring bubbles to form a large bubble, which

eventually erupts at the top of the column. This formation, movement, and eruption of the bubble is the basic attribute of the BFB which determines the amount of heat and mass transfer between phases.

Many numerical and experimental studies have been undertaken to study the hydrodynamics of BFB under different operating condition. In the following subsection, an overview of these studies is presented. It is to note that, in the next two subsections, BFB containing solid particles of same material and uniform size are considered, commonly known as mono–dispersed BFB.

2.4.1. Experimental studies

Since the conceptualization of fluidization in Winker's coal gasifier in 1926 [66], several experimental studies have been performed to study the hydrodynamics of BFB. Various aspects which define the BFB such as minimum fluidization velocity, bubble properties, etc. have been measured using different techniques.

Measurement techniques used in the BFB can be broadly classified as intrusive and non-intrusive. Intrusive techniques such as optical or capacitance probes generate a pulse signal after coming into contact with the bubble. These probes are designed in such a way that pulse signal generated by the same bubble is measured at two axial height. The time gap between the two pulse signal and the distance between the probe tips is then used to calculate the bubble velocity. Werther and Molerus [18] calculated this time gap using the cross-correlation method. The major disadvantage of intrusive techniques is that they alter the local flow behavior of the gas [19,22,67]. Moreover, the data generated from probes are highly dependent on the orientation inside the BFB. A slight change in the orientation results in inconsistent data [19].

Non–intrusive measurements, on the other hand, are much more robust and does not alter the hydrodynamics of BFB. Non–intrusive can be further classified into particle tracking and

tomography techniques. A tomographic technique such as ECVT captures the gas/solid volume distribution of the BFB whereas, particle tracking such as radioactive particle tracking (RPT) follows the motion of single particle rather than the solid as a whole. Pressure and acoustic measurement though falls into the non–intrusive classification, but they do not either track the single particle or measure the gas/solid volume distribution. They measure the pressure and acoustic energy, generated by coalescence, movement, and eruption of bubbles. van Ommen and Mudde [68] and Sun and Yan [69] have comprehensively reviewed the non–intrusive techniques used in the gas-solid fluidized beds.

Table 2.3 summarizes the recent experimental studies on the gas-solid BFB. The sensor used, the fluidization condition, the parameter calculated/ measured and the main observation of these studies is detailed in this table.

Measurement of pressure drop is the commonly used experimental technique. It is mostly used to determine the minimum fluidization velocity [70–72] and regimes by analyzing the fluctuation [62] or frequency [61] of pressure time series. Van der Schaaf et al. [73] re-evaluated the published results on the origin and attenuation of pressure waves in BFB and found that bubbles and volume distribution are the main reason for pressure wave generation and attenuation. Bubble formation and coalesce results in upward moving pressure waves, the amplitude of which is linearly dependent on the distance to the bed surface. Whereas, bubble eruption, and coalesce and gas volume distribution causes the downward moving pressure waves with an amplitude independent of the distance to the bed surface. Consequently, van der Schaaf et al. [74] decomposed the pressure fluctuation measured by the sensor into waves caused by the bubbles and that caused by the volume distribution. Pressure fluctuations were simultaneously measured at a height above the distributor and the plenum section, and power

spectral density (PSD) analysis was used to decompose these pressure waves into the coherent and incoherent output. Incoherent output was directly linked to the bubble characteristic length at that height above distributor. The measured characteristic length compares reasonably well with the bubble diameter calculated from the correlation of Darton et al. [9]. Liu et al. [75] extended the work of van der Schaaf et al. [74] for Geldart A particles and estimated the bubble diameter for FCC particle of size 78 µm.

Hulme and kantzas [52] conducted the X-ray fluoroscopy experiments to measure the bubble properties in a cylindrical bed. They used linear low-density polyethylene (LLDPE) particles with a wide size distribution ranging from 100 µm to 1500 µm with a mean of 850 µm. Bubble properties were calculated by first identifying the bubble using image analysis and then tracking the bubble to determine the bubble diameter and velocity respectively. The calculated bubble diameter and velocity compared well with the empirical correlation of Werther [10] and Kunii and Levenspiel [66] respectively.

Busciglio et al. [15] on the other hand determined the bubble properties using the digital image analysis technique (DIAT), which is another widely used experimental technique other than the pressure measurement. Visual observation of the fluidization process under dynamic condition makes it easy to interpret the obtained results. However, the opaqueness caused by the presence of solids results in data capture along the wall only [68]. Nevertheless, Busciglio et al. [15] determined the bubble diameter and velocity and aspect ratio using DIAT. Bubble diameter results compared reasonably well with Darton et al. [9]. They calculated the bubble velocity using two methods (i) based on the cross-correlation method and (ii) based on tracking bubbles to determine the distance traveled by the bubble in the one-time frame.

Fan et al. [5] used positron emission particle tracking (PEPT) method to determine the particle and bubble velocity and flow pattern of the solids. The data obtained from PEPT can be easily transformed into the particle velocity, and bubble velocity was calculated from particle velocity by assuming particles in the wake travel with the same velocity as that of the bubbles [3,76]. The top 10% of particle V_y (particle velocity in the y-direction) velocities were considered as particle wake velocity, and an average of this velocity was the measure of bubble velocity. The vector plot of the particle velocity determines the flow pattern of the solid in the experiments. Fan et al. [77] observed three flow patterns

1. Single bubble regime at low velocity, where the particles move upward along one side of the wall and come down from the other side.
2. At higher velocity for glass beads particles, the particles move upward from the center and come down along the walls.
3. At higher velocity for polyethylene particles, a combination of the above two patterns was observed. At the lower portion of the bed, single bubble regime was observed whereas at the upper portion, solids moving from the center and coming along the walls was observed and these two flow regimes merge at the intermediate portion of the bed.

Laverman et al. [78] coupled the two non–intrusive techniques – high speed imaging (DIAT) and particle image velocimetry (PIV). DIAT was used to determine the gas/solid volume distribution whereas, PIV was used to determine the particle velocity. It was observed that the bubble diameter and velocity measurement was consistent with the empirical correlation and bubble properties depends strongly on the width of the bed due to the wall effect. Packed bed height does not have any effect on either bubble properties or emulsion phase velocity. Subsequently, Delgabo et al. [16] also coupled the DIAT and PIV and calculated the circulation

time of particles defined as the time taken by particles to move from the bottom of the bed to top and back.

Chandrasekera et al. [79] compared the results obtained from MRI and ECVT. The comparison was mostly qualitative in nature and smoothness inherited from the reconstruction process resulted in low spatial resolution of ECVT reconstructed images. Rautenbach et al. [80], on the other hand, quantified the comparison of results obtained from the ECVT and time-resolved X-ray tomography. It was observed that the presence of a small amount of fine in the solid phase results in smaller and distributed bubbles which consequently alters the hydrodynamics of the fluidized bed.

Weber and Mei [55] performed experiments on BFB using ECVT and measured the bubble diameter, velocity, solids volume fraction of the bed. The quantitative results obtained from the ECVT were compared with empirical correlations. It was observed that bubble size increased with height until it reached a maximum and stable bubble diameter. After that, it starts decreasing due to bubble splitting. Similar phenomena of stable bubble diameter was also observed by Shen et al. [14].

Asegehegn et al. [54] measured the effect of immersed tubes on the bubble properties. DIAT was carried out in a 2D column comprising of the immersed tube and also in another column without tubes. It was observed that immersed tubes strongly influence the bubble properties in the tube bank region and result in properties being independent of superficial velocity, particle size, and bed height. Splitting is predominant in the bed containing immersed tubes, and therefore, bubble size obtained from such bed is smaller than that obtained from bed without tubes.

Dubrawski et al. [67] carried out the hydrodynamics study of BFB using various measurement techniques – invasive and non–invasive, available at different research labs across Canada. Influence of probes on the local hydrodynamic of BFB was studied. Time average voidage measured using different techniques was compared, and it was observed that invasive techniques result in slightly higher voidage compared to non–invasive techniques. Effect of geometry, orientation, and height from the distributor of the probe tip on the hydrodynamics of gas-solid fluidized bed was also studied by Whitemarsh et al. [22]. It was found that probe tip orientation and height from the distributor significantly affects the local hydrodynamics while geometry does not have any effect. Moreover, the presence of the probe affects only the local hydrodynamics whereas, bed expansion does not get affected by its presence.

Buist et al. [6] tracked a single magnetic marker in the bed using magnetic particle tracking (MPT). Similar to the logic applied in other tracking techniques such as RPT or PEPT the properties of this magnetic marker correspond to the particle properties, and the movement of a single magnetic marker corresponds to the movement of complete solid phase. It was found that the results from MPT were significantly influenced by the magnetic moment and relative distance of the magnetic marker from the sensor array. Magnetic field strength also gets influenced by the orientation of the magnetic marker, and in the case of non–spherical particles, this influence could be utilized to study the fluidization of non–spherical particles.

Recently, Gopalan et al. [56] have reported data obtained from PIV and pressure transducers for gas-solid BFB consisting of Geldart D particles. Higher order statistics of particle velocity such as mean, root mean square (RMS), skewness and kurtosis and the granular temperature was reported for all the particles at the vicinity of the wall. Analysis of higher order statistics

revealed that particle velocity distribution was closer to Gaussian distribution near the center of the bed but varied substantially near the walls.

Consequently, despite the challenges posed by the gas-solid BFB such as opaqueness of the system, wide spectrum of scale of operation, experimental techniques have still been able to determine the characteristic features of BFB. However, the different experimental techniques still have few limitations such as digital imaging can determine the properties at the wall only because of the opaqueness, whereas, "nuclear field" tomographs comprising of X-ray, nuclear magnetic resonance, etc. have intermediate temporal resolution and requires extensive safety precautions [68]. These limitations of experimental technique restrict their usage in scale-up geometry. Moreover, using the experimental techniques under the extreme operating conditions such as high temperature, high pressure, etc. are resource intensive. Numerical techniques, consequently, can be used for the scale-up geometry and at the extreme operating conditions. The next section reviews the simulation studies particularly the CFD on the gas-solid BFB.

Table 2.3 Summary of experimental studies on mono–dispersed fluidized bed

Reference	Measurement Technique	Experimental Setup	Results
Van der Schaaf et al. [74]	Pressure transducer Operating Condition H_0= 30 cm $\boldsymbol{U}_G$= 1.4 – 6.8$\boldsymbol{U}_{mf}$	Bed: Cylindrical d_{bed} = 38.5 Particle: d_p= 390 µm, ρ_p= 2.65 gm/cm^3, $\boldsymbol{U}_{mf}$= 14 cm/s, Geldart B	Results reported: Bubble diameter Observation: A method to calculate the bubble diameter from the pressure fluctuation analysis was proposed.
Hulme and Kantzas [52]	X-ray fluoroscopy Operating Condition H_0= 40 cm $\boldsymbol{U}_G$= 2.5 – 3.5$\boldsymbol{U}_{mf}$	Bed: Cylindrical $d_{bed} \times H$ = 10×100 cm Particle: d_p= 850 µm, ρ_p= 0.65 gm/cm^3, $\boldsymbol{U}_{mf}$= 7.7 cm/s, Geldart B	Results reported: Bubble diameter, Bubble velocity Observation: Measured bubble diameter and velocity compares well with the empirical correlation of Werther [10] and Kunii and Levenspiel [66] respectively.
Busciglio et al. [15]	DIAT	Bed: Rectangular 2D $L \times B \times H$ = 18×1.5×80 cm	Results reported: Bubble diameter, Bubble rise velocity, Bubble aspect ratio

	Operating Condition H_0= 36 cm $\boldsymbol{U}_G$= 3.4$\boldsymbol{U}_{mf}$	Particle: d_p= 231 µm, ρ_p= 2.5 gm/cm^3, $\boldsymbol{U}_{mf}$= 5.24 cm/s, Geldart B	Observation: Two methods based on cross-correlation and bubble tracking were used to calculate the bubble rise velocity.
Fan et al. [5] Fan et al. [77]	PEPT Operating Condition H_0= 15.2 cm $\boldsymbol{U}_G$-$\boldsymbol{U}_{mf}$= 25 and 42 cm/s	Bed: Cylindrical $d_{bed} \times H$ = 15.2×100 cm Particle: d_p= 717, 352 µm, ρ_p= 0.76, 2.7 gm/cm^3, $\boldsymbol{U}_{mf}$= 24, 15 cm/s, Geldart B	Results reported: Particle velocity, Bubble velocity, Flow pattern Observations: Bubble velocity was assumed to equal to particle velocity in the wake owing to the observations of Geldart and Baeyens [76] and Stein et al. [3] A significant difference in particle/bubble flow pattern was observed for different bed material and superficial velocity.
Laverman et al. [78]	PIV and DIAT Operating Condition H_0= 15, 30 and 45 cm $\boldsymbol{U}_G$= 1.5, 2, 2.5 and 3.5$\boldsymbol{U}_{mf}$	Bed: Rectangular 2D $L \times B \times H$ = 15× 1.5×70 cm and 30×1.5×70 cm Particle: d_p= 500 µm, $\boldsymbol{U}_{mf}$= 18 cm/s, Geldart B	Results reported: Bubble diameter, Bubble velocity, Emulsion phase velocity Observation: Measurement of bubble diameter and velocity were consistent with the empirical correlation and bubble properties depends strongly on the width of the bed.

Liu et al. [75]	Optical probe and Pressure transducers Operating Condition H_0 = 100 cm $\boldsymbol{U}_G$ = 10–50 cm/s	Bed: Cylindrical $d_{bed} \times H$ = 29 × 450 cm Particle: d_p= 78 µm, ρ_p= 1.56 gm/cm^3, $\boldsymbol{U_{mf}}$= 0.25 cm/s, Geldart A	Results reported: Bubble diameter Observation: Decomposition of pressure fluctuation given by Schaaf et al. [74] to predicts the bubble size.
Asegehegn et al. [54]	DIAT Operating Condition H_0= 50 cm $\boldsymbol{U}_G$= 2, 3, and 4$\boldsymbol{U}_{mf}$	Bed: Rectangular 2D $L \times B \times H$ = 32 × 2 × 120 cm Particle: d_p= 246, 347, 439, and 776 µm, ρ_p= 2.5 gm/cm^3, $\boldsymbol{U}_{mf}$= 8.76, 14.4, 24, and 46.7 cm/s, Geldart B	Results reported: Bubble diameter, Bubble rise velocity Observation: Bubble properties, calculated for a bed with and without immersed horizontal tube, were independent of superficial velocity, particle size and bed height in the tube bank region. Splitting was predominant in the bed containing immersed tube.
Escudero and Heindel [72]	X-ray CT and Pressure transducers	Bed: Cylindrical	Results reported: Minimum fluidization velocity, Gas holdup

	Operating Condition H_0= 5.1, 10.2, 15.3, 20.4, 30.6 cm $\boldsymbol{U}_G$= 1.25 – 3$\boldsymbol{U}_{mf}$	$d_{bed} \times H$ = 10.2× 91 cm Particle: d_p= 550 µm, ρ_p= 2.6, 1.3, 1 gm/cm^3, Geldart B	Observation: Effect of static bed height on minimum fluidization velocity and gas holdup was studied.
Chandrasekera et al. [79]	MRI and ECVT Operating Condition $\boldsymbol{U}_G$ = 4.5–28 L/min (Single jet through an orifice of diameter 0.4 cm drilled in the center)	Bed: Cylindrical $d_{bed} \times H$ = 5×15 cm Particle: d_p= 1200 µm, ρ_p= 0.96 gm/cm^3, $\boldsymbol{U}_{mf}$= 35L/min, Geldart D	Results reported: Qualitative profile of jet, Solids volume fraction, Jet length Observation: Spatial resolution and contrast of ECVT reconstructed images was low owing to the smoothness inherited from the reconstruction process.
Delgabo et al. [16]	PIV and DIAT Operating Condition H_0 = 30, 40, 50, 60 cm $\boldsymbol{U}_G$ = 1.5, 1.75, 2, 2.25 and 2.5$\boldsymbol{U}_{mf}$	Bed: Rectangular 2D $L \times B \times H$ = 50×0.5×150 cm Particle: d_p= 677.8 µm, ρ_p= 2.5 gm/cm^3, $\boldsymbol{U}_{mf}$= 48.125 cm/s, Geldart B	Results reported: Circulation time Observation: Experimentally determined circulation time was compared with the correlation.

Dubrawski et al. [67]	Optical probes, Pressure transducers, ECT, X-ray CT and RPT Operating Condition H_0 = 10.2 cm $\boldsymbol{U}_G$ = 30 – 60 cm/s	<u>Bed:</u> Cylindrical $d_{bed} \times H$ = 13.3×96 cm <u>Particle:</u> d_p= 104, 332 µm, ρ_p= 1.56, 2.644 gm/cm^3, $\boldsymbol{U}_{mf}$= 0.606, 7.96 cm/s, Geldart A, B	<u>Results reported:</u> Voidage <u>Observation:</u> Time average voidage measured using invasive and non–invasive techniques were compared, and the influence of probes on local hydrodynamics was established.
Rautenbach et al. [80]	ECT Time-resolved X-ray tomography Operating Condition $\boldsymbol{U}_G$ = 5–70 cm/s	<u>Bed:</u> Cylindrical d_{bed} = 10.4 cm (ECT) and 23.8 cm (X-ray) <u>Particle:</u> d_p= 153, 482.9, 899.15, 265.58, 800.35, 114 µm, ρ_p= 2.485 gm/cm^3, $\boldsymbol{U}_{mf}$= 2, 21, 45, 4, 27, 0.9 cm/s, Geldart B	<u>Results reported:</u> Bubble volume, Bubble frequency <u>Observation:</u> Presence of small amount of fine in the solid phase results in smaller and distributed bubbles in the bed which consequently alters the hydrodynamics of the fluidized bed.
Weber and Mei [55]	ECVT	<u>Bed:</u> Cylindrical $d_{bed} \times H$ = 10×170 cm	<u>Results reported:</u> Solids volume fraction, Bubble frequency, Bubble diameter, Bubble aspect ratio

	Operating Condition $\boldsymbol{U}_G$= 1, 2, 4, 6 $\boldsymbol{U}_{mf}$	Particle: d_p= 185 µm, ρ_p= 2.483 gm/cm^3, $\boldsymbol{U}_{mf}$= 3.17 cm/s, Geldart B	Observation: Bubble size increases with height until it reaches a maximum and stable bubble diameter. After that, it started decreasing due to the bubble splitting.
Buist et al. [6]	MPT Operating Condition $\boldsymbol{U}_G$ = 250, 350 cm/s	Bed: Rectangular 2D $L \times B \times H$ = 30×1.5×100 cm Particle: d_p= 3000 µm, ρ_p= 2.526 gm/cm^3, $\boldsymbol{U}_{mf}$ = 170 cm/s Geldart D	Results reported: Particle velocity Solids volume fraction Observation: Newly developed analysis tool shows that data obtained from these experiments were influenced significantly by the magnetic moment and relative distance from the sensor array.
Gopalan et al. [56]	Pressure transducer and PIV with particle tracking Operating Condition $\boldsymbol{U}_G$ = 2,3 and 4$\boldsymbol{U}_{mf}$	Bed: Rectangular 2D $L \times B \times H$ = 23×7.6×122 cm Particle: d_p= 3256 µm, ρ_p= 1.131 gm/cm^3, $\boldsymbol{U}_{mf}$= 1.05 cm/s, Geldart D	Results reported: Pressure drop, Particle velocity, Granular temperature Observation: Particle velocity distribution was closer to Gaussian distribution near the center of the bed.

Whitemarsh et al. [22]	X-ray CT Operating Condition H_0 = 10.2 cm $\boldsymbol{U}_{mf}$ = 1.5 and 3$\boldsymbol{U}_{mf}$	Bed: Cylindrical $d_{bed} \times H$ = 10.2×61 cm Particle: d_p = 550 µm, ρ_p= 2.51 gm/cm^3, $\boldsymbol{U}_{mf}$ = 14.6 cm/s, Geldart B	Results reported: Gas holdup Observation: Effect of the probe tip (geometry, orientation, and height from the distributor) on the hydrodynamics of gas-solid fluidized bed was studied.

2.4.2. Simulation studies

Numerical studies enable innumerable permutation of operating condition and reactor design modifications, which otherwise is resource intensive in experimental studies. Moreover, it is possible to study the fundamentals of the flow structure and inherent heterogeneity of the BFB using CFD simulations. However, the underlying limitation of CFD studies is the availability of a robust model, and computational resources. CFD modeling of gas-solid flow in the fluidized bed is rather difficult because of the disparate time and length scale of multiphase flow structures. The size of bubbles, which determine the hydrodynamics of BFB is in the centimeter scale, whereas gas-solid and solid-solid interaction, which governs the bubble formation is in the micrometer scale [36]. This wide difference in scale of flow structures and the factors determining it causes difficulty in modeling the gas-solid flow. Macroscale (flow structures) and microscale (gas-solid and solid-solid interactions) structure cannot be resolved concurrently, by a single modeling approach. Consequently, a hierarchy of gas-solid flow models that can resolve the hydrodynamics at various scale is required [36].

Gas and solid phase can be modeled using Eulerian or Lagrangian approach. In the Eulerian method, the flow of gas or solid is considered continuum and is resolved around the fixed control volume. Navier–Stokes equation is solved to determine the flow behaviour using Eulerian method. Whereas, in the Lagrangian method, flow of gas parcel/ solid particle is tracked in space and time domain and Newton's equation of motion is resolved to determine the flow structure using Lagrangian method. Depending upon the resolution required for gas and solid phase, a combination of gas and solid flow model can be obtained as described in Table 2.4.

Table 2.4 Classification of gas-solid model [36]

Name	Gas phase	Solid phase	Gas-solid coupling
Discrete bubble model	Lagrangian	Eulerian	Drag closure for bubbles
Two fluid model	Eulerian	Eulerian	Gas–solid drag closure
Unresolved discrete particle model	Eulerian (Unresolved)	Lagrangian	Gas–particle drag closure
Resolved discrete particle model	Eulerian (Resolved)	Lagrangian	Boundary condition at particle surface
Molecular dynamics	Lagrangian	Lagrangian	Elastic collision at particle surface

EE and EL are the most commonly used models in gas-solid fluidized bed with EL being the focus of this thesis. In the EL model, also known as discrete particle model (DPM), the gas phase is assumed to be continuous, and the solid phase is treated as discrete particles. The EL models can be further classified as unresolved-DPM (u-DPM), and resolved-DPM (r-DPM) models based on the spatial discretization of the continuous phase [36]. In u-DPM models, the size of the Eulerian grid is larger than the size of the solid particles, whereas, in r-DPM models, it is smaller than the solid particles. The u-DPM model is also referred to as a CFD–DEM.

Tsuji et al. [81] were the first to apply the CFD–DEM methodology in gas-solid BFB. Particle-particle and particle-wall collisional force were modeled using the soft sphere approach [37]. An in-house code was developed to solve the fluid and solid phase equations simultaneously. Reduced stiffness coefficient was used to decrease the computational power requirement. Tsuji et al. [81] argued that, if the actual stiffness coefficient was taken, the particle time step would be too small thus making the computation unrealistic. Pressure fluctuations and snapshot from

the simulation were compared with the experiments, and the results were not quantitatively similar.

Hoomans et al. [82] contended the soft sphere approach adopted by the Tsuji et al. [81] and developed a new collisional model named hard sphere model. In their model, realistic values of the key parameter were used, and the binary collision was assumed whereas, the multi-particle collision was assumed in the soft sphere model. Hoomans et al. [82] performed the parametric study to determine the sensitivity of restitution and friction coefficient, and the results were compared with the Tsuji et al. [81]. It was found that simulations were strongly dependent on the restitution and friction coefficient. Furthermore, Hoomans et al. [82] performed another simulation to compare the qualitative profile of bubble formation with an experimental study of Nieuwland [83]. Subsequently, many DEM simulations with the hard sphere and soft sphere collision models were reported. Table 2.5 presents the summary of the latest numerical studies on BFBs containing Geldart B or D type particles.

Muller et al. [84] performed the validation and sensitivity study of the CFD–DEM predictions for Geldart B/D particles. The sensitivity of different parameters such as coefficient of restitution, friction, boundary conditions, distributor design and drag models on the CFD–DEM predictions were studied. Experiments using MRI were performed, and the gas volume faction profile was compared. Ku et al. [48], on the other hand, also performed similar simulations where the effect of drag models, restitution coefficient and friction coefficient were analyzed. Ku et al. [48] compared the predicted minimum fluidization velocity with the reported one. Muller et al. [84] and Ku et al. [48] independently developed the CFD–DEM code and the drag model analyzed were different. Muller et al. [84] used Beetstra–van der Hoef–Kuiper (BVK), Di Felice and Gidaspow whereas, Ku et al. [48] used the Hill–Koch–Ladd (HKL) model instead

of BVK. Moreover, Ku et al. [48] used the particles of Geldart D classification. Despite the differences, Muller et al. [84] and Ku et al. [48] concluded that drag is the most dominant force in gas-solid fluidized bed, and collisional parameters have little effect on the predictions as long as some means of energy dissipation was defined, i.e., either restitution coefficient or friction coefficient should be non-zero.

Norouzi et al. [85] compared the CFD–DEM predictions with the RPT experiments for the Geldart D particles. Solid movement in bubbling fluidized bed was analyzed using the parameters such as diffusivity and internal and gross circulation. Qualitative profile of instantaneous particle position shows that by increasing the aspect ratio, particle flow pattern differs significantly. At aspect ratio less than one, the flow pattern of the shallow fluidized bed was observed, i.e., particles moving down near the wall and center of the bed whereas, moving up by the wake of the bubbles. At an aspect ratio of one, particles were coming down from the wall while moving up from the center and for aspect ratio more than one, a combination of above two aspect ratio was seen – shallow flow regime near the distributor and above that, the flow pattern of the aspect ratio of one. Further, 2D simulations were able to capture the hydrodynamics of experiments performed on the 3D bed, and axial diffusivity was dominant at higher velocity due to increased gross circulation.

Karimi et al. [86] proposed a new method to compare the experimental results with simulation results. Measured and predicted pressure fluctuations were compared in the state space domain using the chaotic attractor. S–statistic was calculated from this attractor to determine the similarity of dynamics captured by the simulations and experiments. S-statistic value of less than three indicates that dynamics are similar for the given signals.

Elghannay and Tafti [87] tested the ability of their in-house code GenIDLEST for CFD–DEM simulations and compared the predictions with the experimental results of the NETL challenge problem [56]. GenIDLEST [88] was originally developed to perform the transitional and turbulent flow simulation in complex geometries, and its capacity was later extended for CFD–DEM methodology. Measured and predicted results of pressure drop and horizontal and vertical particle velocity were compared. Reasonable qualitative agreement between measured and predicted results was seen. However, there was a discrepancy in quantitative comparison.

Peng et al. [89] also developed the in-house CFD–DEM code and compared the predictions of pressure fluctuation and qualitative particle position profile with that reported by van Wachem et al.[32]. Peng et al. [89] observed the limitation of commonly used particle centroid method (PCM) to calculate the gas/solids volume fraction in a cell. In PCM method, the location of the centroid of the particle determines the cell to which that particle belong, and complete volume of the particle was considered for the calculation of void fraction of that cell. Whereas, in the analytical method, the volume of the proportion of particle in a cell was used to determine the void fraction of a cell. Critical cell size was determined above which the PCM will predict the experimental result as accurately as an analytical method. Various combinations of the domain to cell size ratio and cell to particle size ratio were simulated and a reference map to select the ideal computational cell size and suitable method to calculate the void fraction was henceforth, developed.

Busciglio et al. [90], Hernández-Jiménez et al.[91], Verma et al. [92], and Lungu et al. [50] performed the two fluid model (TFM) simulations with kinetic theory of granular flow (KTGF) closure model. All of them used Gidaspow drag model except by Verma et al. [92], who used the BVK models. Different experimental techniques such as DIAT by Busciglio et al. [90],

DIAT and PIV by Hernández-Jiménez et al. [91], X-ray tomography by Verma et al. [92] and pressure drop and PIV by Lungu et al. [50] were used to validate the predictions with measurements. Though different experimental techniques were used, all of them compared the bubble diameter and velocity except for Lungu et al. [50], who compared the particle velocities. Although TFM simulations have been widely used in the gas-solid fluidized bed, the continuum assumption of the solid phase in this methodology limits its ability to analyze the emulsion phase dynamics thoroughly.

Almohammed et al. [93] compared the simulations prediction from CFD–DEM with TFM simulations and also with the experimental results from DIAT. It was observed that CFD–DEM was able to predict the experimental results more consistently than TFM with KTGF closure. Closer predictions from DEM could be attributed to the consideration of particle as a discrete entity in DEM rather than averaging of particle properties over a control volume as in TFM.

The literature reviewed above, clearly shows that the application of DEM for gas-solid fluidized bed is mostly based on the in-house codes. Consequently, NETL developed a DEM code for the solids and integrated it with the already existing open source CFD code – MFiX [94–96]. Many researchers [49,97–100] performed DEM simulations using the newly developed MFiX–DEM code. Li et al. [97] investigated the effect of bed thickness on the hydrodynamics of fluidized bed, and it was observed that the bed behavior would start changing from 2D to 3D when the thickness of the bed is changed from 20 d_p to 40 d_p. Luo et al. [100], on the other hand, analyzed the mixing process in the mono–dispersed fluidized bed system. It was observed that the dispersion coefficient is anisotropic in the axial direction, i.e., mixing of particles will predominantly take place in the axial direction. Moreover, the dispersion coefficient increases with an increase in superficial velocity.

From the literature reviewed, it could be summarized that though the DEM methodology for the gas-solid flow was first applied in 1993, there has not been the widespread use of this methodology. Primarily, because of the high computational resource required by the DEM to track each particle. Whereas, EE or TFM simulation has been widely used simulation methodology because of the relatively low amount of computational requirement. Consequently, EE can be used for the industrial scale simulations as well. Nevertheless, DEM methodology which can give the flow properties at the particle scale is applied in this thesis, because of the fewer assumptions used. Empirical correlation of the drag force is the only uncertainty in the CFD–DEM predictions. Since drag is the most dominant force, this uncertainty could result in a discrepancy between the predictions and experimental results. It is, therefore, the effect of the drag model on the CFD–DEM predictions is studied in Chapter 3 of this thesis.

Table 2.5 Summary of numerical studies on mono–dispersed fluidized bed

Reference	Model	Computations	Validation	Comments
Tsuji et al. [81]	CFD–DEM Drag: Gidaspow Contact: Soft sphere k = 800 Nm^{-1}, e = 0.9, ν = 0.3 In house code	Geometry: Rectangular 2D Bed (L) = 15 cm Grid ($L \times H$) = 1×2 cm Particle: d_p= 4000 µm, ρ_p= 2.7 gm/cm^3, N_p= 2400, $\boldsymbol{U}_{mf}$= 177 cm/s, $\boldsymbol{U}_G$= 20–26 cm/s, Geldart D	Measurement technique/ experimental study: Pressure transducer, Videography Results compared: Pressure fluctuations Air velocity at the onset of bubbling.	EL simulations were performed with the contact force model given by Cundall and Strack [37].
Hoomans et al. [82]	CFD–DEM Drag: Gidaspow Contact: Hard sphere e = 0.96, ν = 0.15 In house code – POGO	Geometry: Rectangular 2D Bed ($L \times H$) = 19.5×30 cm Grid ($L \times H$) = 0.5×0.5 cm Particle: d_p= 850 µm, ρ_p= 2.93 gm/cm^3, N_p= 40000, $\boldsymbol{U}_{mf}$= 50 cm/s, $\boldsymbol{U}_G$= 250 cm/s (injected through a central orifice of diameter 1.5 cm)	Measurement technique/ experimental study: Nieuwland [83] Results compared: Qualitative profile of bubble formation from a single orifice.	New collision model was proposed based on the linear and angular momentum conservation.

Busciglio et al. [90]	TFM with KTGF Drag: Gidaspow $\Delta t = 10^{-3}$ s Fluent–CFX	Geometry: Rectangular 2D Bed ($L \times B \times H$) = 18×1.5×80 cm Grid ($L \times H$) = 0. 5×0.5 cm Particle: d_p= 212 - 250 µm, ρ_p= 2.5 gm/cm^3, $\boldsymbol{U}_{mf}$= 5.24 cm/s, H_0= 36 cm, $\boldsymbol{U}_G$= 1.7, 3.4, 5 and 7 $\boldsymbol{U}_{mf}$	Measurement technique/ experimental study: Busciglio et al. [15] Result compared Qualitative profile of volume fraction distribution, average bed height, bubble holdup, bubble diameter and bubble velocity	Bimodality for the local BSD at all elevations highlighted the richness and complexity of the bubbling dynamics, which includes bubble break-up and coalescence phenomena.
Muller et al. [84]	CFD–DEM Drag: BVK, Di Felice and Gidaspow Contact: Soft sphere e = 1–0.01, ν = 0.0–0.3 In house code	Geometry: Rectangular 2D Bed ($L \times B \times H$) = 4.4×1×12 cm Grid ($L \times H$) = 0.37×1×0.5 cm Particle: d_p= 1200 µm, ρ_p= 1 gm/cm^3, N_p= 9240, $\boldsymbol{U}_{mf}$= 30 cm/s, $\boldsymbol{U}_G$= 60 and 90 cm/s, Geldart B/D	Measurement technique/ experimental study: MRI Results compared: Gas volume fraction	Values of restitution or friction coefficient does not have any effect on CFD–DEM prediction as long as ideal collision (Restitution = friction = 0) is not assumed.
Hernández-Jiménez et al. [91]	TFM with KTGF Drag: Gidaspow and Syamlal–O'Brien	Geometry: Rectangular 2D Bed ($L \times B \times H$) = 50×0.5×200 cm	Measurement technique/ experimental study: DIAT and PIV	Simultaneous measurements from DIAT and PIV enable

	e = 0.9, ϵ_0 = 0.6, Δt = 5 × 10^{-4} s Ansys fluent code	Grid ($L \times H$) = 0. 5×0.28 cm Particle: d_p= 700 µm ρ_p= 2.5 gm/cm^3, $\boldsymbol{U}_{mf}$= 35 cm/s, H_0= 30 cm, $\boldsymbol{U}_G$= 1.75 $\boldsymbol{U}_{mf}$	Results compared: Bubble size, Bubble velocity, Solid phase velocity	the comparison of bubble properties and solid phase velocity with the TFM simulations.
Norouzi et al. [85]	CFD–DEM Drag: Gidaspow Contact: Soft sphere k = 800 Nm^{-1}, e = 0.9, ν = 0.3 In house code	Geometry: Rectangular 2D Bed ($L \times H$) = 15×90 cm Grid ($L \times H$) = 0.2×0.2 cm Particle: d_p= 650 µm, ρ_p= 2.650 gm/cm^3, N_p= 34000, 67000, 110000, $\boldsymbol{U}_{mf}$= 35 cm/s, $\boldsymbol{U}_G$ = 53, 70, 80, 100 cm/s, Geldart D	Measurement technique/ experimental study: RPT Results compared: Diffusivity and Circulation length	Additional results: Qualitative profile of instantaneous particle position Observation: Significant difference in flow pattern of solids was seen with varying aspect ratio.
Karimi et al. [86]	CFD–DEM Contact: Soft sphere k = 800 Nm^{-1}, e = 0.9, ν = 0.3 In house code of Mansourpour et al. [101]	Geometry: Cylindrical Bed ($d_{bed} \times H$) = 10×200 cm Grid ($L \times B \times H$)= 0.3×0.3×0.3 cm Particle:	Measurement technique/ experimental study: Pressure transducers Results compared: Pressure fluctuations, S–statistic, Multi–resolution analysis	Observation: A new method based on S–statistic and Multi–resolution analysis was proposed to compare the experimental results of

		d_p= 600 µm, ρ_p= 0.92 gm/cm^3, N_p= 60000, $\boldsymbol{U}_{mf}$= 10 cm/s, $\boldsymbol{U}_G$= 40, 55, 65 cm/s, Geldart B		pressure signals with simulations.
Li et al. [97]	CFD–DEM Drag: Gidaspow Contact: Soft sphere k = 800 Nm^{-1}, e = 0.97, ν = 0.1 MFiX–DEM code	<u>Geometry:</u> Rectangular 2D Bed ($L \times H$) = 10×50 cm Thickness (B) = 0.1, 0.5, 1, 2, 4 and 10 cm Grid ($L \times H$) = 0.5×0.5×0.5 cm <u>Particle:</u> d_p= 1000 µm, ρ_p= 2.5 gm/cm^3, N_p= 8000, 40000, 80000, 160000, 320000, 800000, $\boldsymbol{U}_G$ = 80 cm/s	Validation was done in another study of the same author– Li et al. [96]	<u>Additional results:</u> Solids volume fraction, Average particle height, Qualitative bubble behaviour, Particle velocity and kinetic energy <u>Observation:</u> Effect of bed thickness on the hydrodynamics of fluidized bed was investigated.
Ku et al. [48]	CFD–DEM Drag: Gidaspow, Di Felice, HKL Contact: Soft sphere k = 1.28×10^5, 1.28×10^6, 1.28×10^7	<u>Geometry:</u> Rectangular 2D Bed ($L \times B \times H$) = 15×0.4×90 cm Grid ($L \times B \times H$)= 0.1×0.4×0.2 cm <u>Particle:</u>	<u>Measurement technique/ experimental study:</u> Hoomans et al. [82], Xu and Yu [102] and Boyalakuntla [103] <u>Results compared:</u>	<u>Additional results:</u> Qualitative profile of instantaneous particle position and Bed pressure drop <u>Observation:</u>

	Nm^{-1}, e = 0.9, ν = 0.3 DEM methodology implemented in OpenFoam framework	d_p= 4000 µm, ρ_p= 2.7 gm/cm^3, N_p= 2400, $\boldsymbol{U}_G$= 4800 cm/s (Jet velocity from a orifice of 0.1cm wide), Geldart D	Minimum fluidization velocity	CFD–DEM Predictions from different drag models, stiffness coefficient and ideal collision case (Restitution = 1, Friction = 0) were compared.
Almohammed et al. [93]	CFD–DEM and TFM with KTGF Drag: HKL, Syamlal–O'Brien, Wen–Yu, Gidaspow k = 4.1×10^5 Nm^{-1}, e = 0.97, ν = 0.1 DEMEST (DEM), Ansys Fluent (TFM)	Geometry: Spouted bed Rectangular 2D Bed ($L \times B \times H$) = 15×2×100 cm Particle: d_p= 2500 µm, ρ_p= 2.5 gm/cm^3, N_p= 36500, $\boldsymbol{U}_{mf}$= 105 cm/s, $\boldsymbol{U}_G$= 5, 6 kg/s, Geldart D	Measurement technique/ experimental study: DIAT Results compared: Qualitative profile of instantaneous particle position and Bed height	Additional results: Particle velocity Observation: Predictions from CFD–DEM were consistent with the experiment than TFM with KTGF.
Elghannay and Tafti [87]	CFD–DEM Drag: Gidaspow Contact: Soft sphere k = 800 Nm^{-1}, e = 0.84, ν = 0.35	Geometry: Rectangular 2D Bed ($L \times B \times H$) = 23×7.6×122 cm Grid ($L \times H$)=0.575×1.27×1.22 cm Particle:	Measurement technique/ experimental study: NETL small scale challenge problem [56] Results compared:	Ability of the in house code to simulate the CFD–DEM methodology and subsequent comparison

	In house code – GenIDLEST	d_p= 3256 µm, ρ_p= 1.131 gm/cm^3, N_p= 92948, $\boldsymbol{U}_{mf}$= 105 cm/s, $\boldsymbol{U}_G$= 2, 3, 4$\boldsymbol{U}_{mf}$, Geldart D	Pressure drop and horizontal and vertical particle velocity	of predictions with the measurements were carried out.
Peng et al. [89]	CFD–DEM Drag: Gidaspow Contact: Soft sphere k = 10000 Nm^{-1}, e = 0.9, ν = 0.3 In house code	Geometry: Rectangular 2D Bed ($L \times B \times H$) = 9×0.8×50 cm Particle: d_p= 1545 µm, ρ_p= 1.150 gm/cm^3, N_p= 17500, $\boldsymbol{U}_{mf}$= 74 cm/s, $\boldsymbol{U}_G$= 90, 130, 180, 230 cm/s	Measurement technique/ experimental study: van Wachem et al. [32] Results compared: Instantaneous particle position and Pressure fluctuation	Limitation of particle centroid method (PCM) to calculate the void fraction in a cell was established and compared with the more robust "analytical" method.
Verma et al. [92]	TFM with KTGF Drag: BVK Δt = 10^{-4} s e = 0.69, 0.74, 0.86	Geometry: Cylindrical Bed ($d_{bed} \times H$) = 10×140 cm Grid ($L \times H$) = 0.3125×0.2 cm Particle: d_p= 1100, 1000, 1000 µm, ρ_p= 0.8, 1.040, 2.526 gm/cm^3, $\boldsymbol{U}_{mf}$= 24, 32, 67 cm/s, $\boldsymbol{U}_G$ = 1.25, 1.5, 2 and 3 $\boldsymbol{U}_{mf}$	Measurement technique/ experimental study: X–ray tomography Results compared: Bubble size, Bubble velocity	Effect of different solid phase, superficial velocity and static bed height were studied and bubble properties obtained from TFM simulations were compared with X–ray tomography

Luo et al. [100]	CFD–DEM Drag: HKL Contact: Soft sphere k = 800 Nm^{-1}, e = 0.97, ν = 0.1 MFiX–DEM code	Geometry: Rectangular 2D Bed ($L \times B \times H$) = 15×1.5×70 cm Grid ($L \times B \times H$) = 1×0.3×1 cm Particle: d_p= 2500 µm, ρ_p= 2.526 gm/cm^3, N_p= 25400, $\boldsymbol{U}_{mf}$= 125 cm/s, $\boldsymbol{U}_G$= 1.25, 1.5, 2$\boldsymbol{U}_{mf}$, Geldart B/D	Measurement technique/ experimental study: Goldschmidt et al. [13] Results compared: Solids volume fraction and Average particle height	Additional results: Solid velocity and flux, dispersion coefficient. Observation: Mixing of particles will predominantly take place in the axial direction.
Lungu et al. [50]	TFM with KTGF Drag: Gidaspow and Syamlal–O'Brien e = 0.92, Δt = 10^{-4} s Ansys Fluent code	Geometry: Rectangular 2D Bed ($L \times B \times H$) = 23×7.5×122 cm Particle: d_p= 3256 µm, ρ_p= 1.131 gm/cm^3, $\boldsymbol{U}_{mf}$= 105 cm/s, H_0= 17.3 cm, $\boldsymbol{U}_G$ = 2, 3 and 4 $\boldsymbol{U}_{mf}$	Measurement technique/ experimental study: NETL small scale challenge [56] Results compared: Pressure drop, Particle velocity, Granular temperature	Simulation results predicted by the TFM were compared with the experimental results reported in the small scale challenge problem.

2.5. **Bi–dispersed BFB**

Many industrial processes use a binary mixture of solid phase differing in density and/or size. These solids phases tend to undergo mixing and segregation during fluidization. Whether mixing or segregation of solids is required, is determined by the process. For instance, segregation is required to remove the potatoes from the clods and stones [104] whereas, mixing of sand and biomass is required for efficient pyrolysis process [105]. The extent of mixing/ segregation of solid phases realized at a given operating condition determines the yield of such processes. Consequently, the extent of mixing and the factors affecting it are critical in bi–dispersed fluidized bed.

There have been many experimental and numerical studies to understand the mixing in bi–dispersed fluidized bed. Table 2.6 summarizes the latest studies on bi–dispersed fluidized bed.

Minimum fluidization condition sets the lower limit of the fluid flow rate where the fluidization process begins [106], and the bubble starts forming for Geldart B and D particles. Rao and Bheemarasetti [107], Si and Guo [108], Oliveira et al.[109], Paudel and Feng [106] followed the conventional approach of measuring the pressure drop across the bed to determine the minimum fluidization velocity of bi–dispersed fluidized bed. Variants of sand and biomass mixed in different ratio and of different shape and size were considered in all the studies. They eventually determined the empirical correlation for predicting the minimum fluidization velocity for a binary particle system, particularly for sand and biomass.

Another important aspect of bi–dispersed fluidized bed is the extent of mixing for given operating conditions. Most commonly used procedure for this purpose is the sieve analysis of the frozen bed. In this procedure, the bed is fluidized at the preset

value of fluid velocity for a certain time until it reaches the steady profile and then the gas supply is suddenly switched off. After that, the solids are extracted from different locations of the collapsed bed. The extracted solids are then sieved, to obtain the mixing/ concentration profile of the bed at a given superficial velocity. Hoffmann et al. [110], Wu and Baeyens [111], Marzocchella et al. [112], and most recently Zhang et al. [24] have used this procedure to determine the mixing or segregation of the bi–dispersed fluidized bed. Zhang et al. [24] performed these experiments with sand and biomass to determine the steady state mixing.

Bai et al. [25] performed similar frozen bed experiments for sand and biomass, but X-ray computed tomography was used to quantify the mixing. Effect of different operating conditions such as initial biomass fraction, biomass size, and superficial velocity on the mixing index was analyzed. It was found that by decreasing the biomass percentage in bed or increasing the superficial velocity, extent of mixing could be increased. Furthermore, Bai et al. [25] also performed the 2D EE simulations and compared the experimental results with the prediction. The simulations were able to capture the trend of mixing, but, there was a quantitative difference in the mixing profile. This discrepancy was attributed to the method of calculation of mixing index for the experiments and simulations. In experiments, mixing index was calculated under the frozen bed condition, whereas, in simulations, it was calculated under dynamic condition and a correction factor was applied to account for the decrease in the height of bed due to freezing.

Olaofe et al. [26] and Sette et al. [29] performed the high speed imaging of the bi–dispersed fluidized bed to determine the extent of mixing. Olaofe et al. [26] extended the work of Goldschmidt et al. [113] to calculate the mixing index of solid phases with same density but different size. Olaofe et al. [26] performed the experiments on glass

beads of diameter 1500, 2500 and 3500 μm and performed experiments using two and three solid phases at a time. They observed that the while the binary fluidized bed was in the segregation state even at the gas velocity slightly higher than individual $\boldsymbol{U}_{mf}$, the ternary mixture becomes well mixed at a velocity lower than $\boldsymbol{U}_{mf}$ of the biggest particle (3500 μm). Sette et al. [29] on the other hand, described the extent of mixing in terms of dispersion coefficient analogous to diffusion coefficient. Two methods - direct and indirect were proposed to calculate the dispersion coefficient in the lateral direction. Direct method was based on the analysis of digital images to calculate the concentration of tracer particle coated with fluorescent color. Whereas, an indirect method was based on monitoring the concentration of tracer leaving the system through the outlet. Indirect method was considerably faster than the direct method but requires the tracer to leave the system, thus reducing the concentration of tracer inside the bed. Moreover, in cold flow study, outflow stream containing tracer particle could only be made possible by fluidizing the system at a very high flow rate or reducing the height of freeboard.

Huang et al. [114] performed the capacitance probe experiments to determine the volume fraction of one phase in a binary system. Quartz sand was independently mixed with salt, aluminium oxide, glass beads, corn grits, and polypropylene plastics and the volume fraction of quartz sand was determined. In all the binary mixtures, size was kept equal for both the solid phase. A linear relationship between the probe signal and volume fraction distribution of quartz sand was found. This relationship, therefore, provides an opportunity to use the capacitance probe in determining the mixing/concentration of solid phase under fluidizing bed condition. However, the invasive nature of probe and applicability of capacitance probe in only those binary

systems where the solids have dielectric and dissimilar permittivity limits the use of capacitance probe.

Girimonte et al. [115] proposed a model to predict the volume fraction of the solid phase in a binary system differing in density or size. To determine the model, initially, well mixed fluidizing system was assumed, and gradually the gas flow rate was reduced to a value lower than the final fluidization velocity of the bed. A gradual decrease in gas velocity results in the sinking of heavier or coarser solid phase first followed by the lighter or finer solid phase. Consequently, near the distributor, the lighter or finer particle will have less concentration compared to the concentration at the top. Similar di–fluidized bed experiments were conducted to compare the experimental results with the model. Although the quantitative comparison was not consistent, the model followed the qualitative trend and captured some important aspect of this phenomenology.

Experimental studies on bi–dispersed fluidized bed have focussed mostly on determining either the minimum fluidization velocity or extent of mixing. The extent of mixing in most of these studies was determined under the “frozen” bed condition, and sudden stoppage of gas supply could influence the mixing. Moreover, opening the walls or segmenting the fluidized bed destroys the integrity of the reactor [114]. Sample collection also becomes critical in such method [24]. Therefore, determining the mixing under the dynamic condition is desirable. Numerical studies can provide the mixing index under the dynamic condition and are, therefore, more suitable for bi–dispersed fluidized beds.

Most of the numerical studies in bi–dispersed are performed using the EE or EL approach. Application of EL is straightforward in bi–dispersed as the motion of

individual particles are resolved and therefore, no extra care is required to resolve the particle-particle contact force. Table 2.6 also summarizes the latest numerical studies performed on bi–dispersed fluidized bed using either the EE or EL approach, with a focus on EL approach.

Bokkers et al. [23] performed the PIV experiments and DEM simulation to track the motion of a single bubble and the mixing induced by the bubble. Two drag models– HKL [116,117] and Gidaspow [42] were used in the simulation, and the predicted size and shape of the single bubble was compared with that observed in experiments. Predictions from HKL were consistent with the experiments and also two collisional model – hard [82], and soft [37] sphere model did not influence the predictions. Furthermore, relative segregation was also determined for the case when the bed was freely bubbling. Predictions were compared to experimental measurements. Bokkers et al. [23] qualitatively showed the motion of particles around the bubble and how the wake pulls the solids with it. Cooper and Coronella [31], on the other hand, performed the EE simulations and also analyzed the solid movement around the bubbles. According to Cooper and Coronella [31], the solids near the distributor were pulled by the wakes and move with the bubble across the bed and then were deposited on the bed surface after the bubble eruption. Whereas, the solids in the emulsion phase travel down the bottom to occupy the space left by the upward moving solids. This circular motion of solids caused mixing. It was also observed that the jetsam and flotsam velocity profile follows the same trend but quantitatively, there was a difference in velocities.

Huilin et al. [118] used the EE and EL approach in a bi–dispersed fluidized bed to investigate the gas-solid flow. Particle segregation phenomena with jetsam settling at bottom and flotsam moving to the top were observed in both EE and EL simulations.

It was observed that fluctuating component of particle velocity was dominant in the vertical direction than lateral direction and better mixing can be obtained by increasing the gas velocity.

Fan and Fox [119] implemented the population balance equation–direct quadrature method of moment (DQMOM) to model the influence of particle size distribution (PSD′) in predictions from EE simulation of gas-solid flow in a fluidized bed. Consequently, a multi-fluid model based on the EE methodology and DQMOM was proposed for the PSD′. Initially, relative segregation obtained from the experiments were compared with predictions for binary PSD′, i.e., two solid phases with the same density and different size. Subsequently, four test cases–Gaussian and lognormal PSD′ distribution with varying standard deviation were simulated to check the rationality of EE with DQMOM in hydrodynamic predictions with continuous PSD′. The predictions for continuous PSD′ were compared with the DEM simulation results of Dahl and Hrenya [120].

It is well established that any amount of mixing can be achieved by varying the superficial velocity and this mixing can be determined from the mixing map prepared by the Di Renzo et al. [121]. This mixing map can determine the extent of mixing for the particles differing in density, and at a given superficial velocity. This map was prepared by comprehensively simulating the bi–dispersed fluidized bed using CFD–DEM for different density and gas velocity ratio.

Peng et al. [27] carried out the extensive CFD–DEM simulations to determine the various factors affecting the mixing. Effect of initial particle configuration, packed bed height, solid size and density ratio and excess gas velocity on the mixing index was studied. Olaofe et al. [28] also studied the effect of different operating condition on

mixing using the CFD–DEM and multi-fluid model. Olaofe et al. [28] used the solid phases with the same density and different sizes. Fotovat et al. [122], on the other hand, determined the bubble size and velocity in the bi–dispersed fluidized bed. Statistical analysis with 1^{st}, 2^{nd}, and 3^{rd} moment of bubble size and velocity were compared for different biomass loading and superficial velocity with experiments.

The literature review on bi–dispersed fluidized bed suggests that the determination of steady state mixing is the most important parameter. The bubble formation, coalesce and eruption govern the mixing process. Further, for a given superficial velocity, mixing of two solid phase can be increased by decreasing the density or size ratio, or increasing the fraction of lighter or fine particle in the mixture. Experiments lag the ability to determine the mixing index in a 3D bed under the dynamic condition, and very few experimental techniques such as high speed imaging or optical probe can be used under the dynamics condition. However, as discussed in the review of mono–dispersed studies section, imaging can be done in the 2D bed and probe alters the local hydrodynamics. Moreover, numerical techniques such as the multi-fluid model based on the EE approach requires the closure model for the particle-particle collisional force and CFD–DEM based on the EL approach requires the high computational requirement.

Table 2.6: Summary of studies on bi-dispersed fluidization

Experimental studies			
Reference	Measurement Technique	Experimental Setup	Results
Rao and Bheemarasetti [107]	Pressure transducer (U–tube manometer)	Bed: Cylindrical $d_{bed} \times H$ = 5×100 cm Particle: Sand 1, d_p= 477.5 µm, ρ_p= 2. 5 gm/cm^3 Sand 2, d_p= 302.5 µm, ρ_p= 2. 7 gm/cm^3 Rice husk, $L \times B \times H$ = 2×1×10 mm Saw dust, d_p = 900 µm Groundnut shell, d_p = 1000 µm	Results reported: Minimum fluidization velocity Observation: New correlation to predict the minimum fluidization velocity for a mixture of biomass and sand particles was proposed.
Shen et al. [123]	DIAT Operating conditions $\boldsymbol{U}_G$ = 52, 69, 104, 122 cm/s	Bed: Rectangular 2D $L \times B \times H$ = 40×0.4×140 cm H_0 = 16 cm Particle: Glass beads, d_p= 605 µm, ρ_p= 2. 6 gm/cm^3, $\boldsymbol{U}_{mf}$= 28 cm/s, Geldart B Biomass, d_p= 8000 µm, ρ_p= 0.52 gm/cm^3	Results reported: Biomass concentration Observation: Rate of mixing of biomass particle in axial direction was higher compared to lateral direction.

Si and Guo [108]	Pressure transducer	Bed: Cylindrical $d_{bed} \times H$ = 5.3×80 cm Particle: Sand, d_p= 255 µm, ρ_p= 2.65 gm/cm^3 Sawdust, d_p= 950 µm, ρ_p= 1.515 gm/cm^3 Wheat stalk, d_p= 1050 µm, ρ_p= 1.2 gm/cm^3	Results reported: Minimum fluidization velocity
Zhang et al. [24]	Frozen method and Sieve analysis Operating conditions $X_{Biomass}$ = 1, 2, 3 % (mass ratio of biomass)	Bed: Rectangular 2D $L \times B \times H$ = 40×40×440 cm Particle: Sand, d_p = 500 µm, ρ_p = 2.56 gm/cm^3 Biomass, $d_p \times H$ = 5×50 mm, ρ_p = 0.3853 gm/cm^3	Results reported: Extent of mixing Biomass distribution Observation: Mixing and segregation behaviour of biomass sand mixture was investigated.
Bai et al. [25]	X–ray CT Operating conditions $\boldsymbol{U}_G$= 1, 2, 3 $\boldsymbol{U}_{mf,GB}$ ϵ_{GWS}:ϵ_{GB} = 0.25:0.75, 0.5:0.5, 0.75:0.25	Bed: Cylindrical $d_{bed} \times H$ = 10.2×91 cm, H_0 = 10.2 cm Particle: Glass beads (GB), d_p= 550 µm, ρ_p= 2.6 g/cm^3, $\boldsymbol{U}_{mf}$= 21.3 cm/s	Results reported: Particle segregation number Observation:

		Ground walnut shell (GWS), d_p= 256, 550, 900 µm, ρ_p = 1.3 g/cm^3	Extent of mixing was calculated at different operating condition.
Olaofe et al. [26]	DIAT Operating conditions $\boldsymbol{U}_G$ = 1.05 – 1.5 $\boldsymbol{U}_{mf}$	<u>Bed:</u> Rectangular 2D $L \times B \times H$ = 30×1.5×80 cm <u>Particle:</u> Glass beads, d_p= 1500, 2500, 3500 µm, ρ_p= 2.552 gm/cm^3	<u>Results reported:</u> Extent of segregation <u>Observation:</u> Binary mixtures segregate at fluidization velocities slightly higher than individual $\boldsymbol{U}_{mf}$, whereas, the ternary mixture becomes well mixed even at a velocity lower than $\boldsymbol{U}_{mf}$ of the biggest particle (3500 µm)

Oliveira et al. [109]	Pressure transducer	Bed: Cylindrical $d_{bed} \times H$ = 5×152 cm Particle: Sand, d_p= 350–1130 µm, ρ_p= 2.695 gm/cm^3 Sorghum, d_p= 250–650 µm, ρ_p= 1.485 gm/cm^3 Tobacco, d_p= 250–600 µm, ρ_p= 1.371 gm/cm^3 Soy hulls, d_p= 300–800 µm, ρ_p= 1.44 gm/cm^3	Results reported: Minimum fluidization velocity
Paudel and Feng [106]	Pressure transducer (Digital manometer)	Bed: Cylindrical $d_{bed} \times H$ = 14.5×100 cm Particle: Sand, Spherical, d_p= 240.8 µm, ρ_p= 2.63 gm/cm^3 Glass bead, Spherical, d_p= 383 µm, ρ_p= 2.5 gm/cm^3 Alumina, Angular, d_p= 490 µm, ρ_p= 3.94 gm/cm^3 Walnut, Spherical, d_p= 100 µm, ρ_p= 1.2 gm/cm^3 Walnut shell, Angular, d_p= 856 µm, ρ_p= 1.2 gm/cm^3 Corn cob, Angular, d_p= 1040 µm, ρ_p= 1.08 gm/cm^3	Results reported: Minimum fluidization velocity

Sette et al. [29]	DIAT Operating conditions $\boldsymbol{U}_G$= 4–37 cm/s	Bed: Rectangular 2D Cross–sectional area = 900, 390 cm^2 Particle: Bronze powder, d_p= 60 µm, ρ_p= 10.6 gm/cm^3 Char pellet, $d_p \times H$ = 3×10 mm, ρ_p= 1.37 gm/cm^3 Wood pellet, $d_p \times H$ = 3×10 mm, ρ_p= 3.29 gm/cm^3 Wood, $L \times B \times H$ = 15×10×6 mm, ρ_p= 1.71 gm/cm^3	Results reported: Dispersion coefficient, Bubble mixing factor Observation: Two method–direct and indirect method were proposed to calculate the dispersion coefficient in the lateral direction.
Huang et al. [114]	Capacitance probe Operating conditions $\boldsymbol{U}_G$ = 42 and 107 cm/s Volume fraction ratio (Quartz : Aluminium oxide or Quartz : Polypropylene) = 1:1	Bed: Rectangular 2D $L \times B \times H$ = 20×1.5×150 cm Particle: Aluminium oxide, d_p= 150–200 µm Polypropylene plastics, d_p= 700–800 µm	Results reported: Volume fraction of quartz sand Observation: A linear relationship between the probe signal and volume fraction distribution of solids was found.
Girimonte et al. [115]	Sieve analysis (de–fluidization) U tube water manometer	Bed: Cylindrical d_{bed} = 10 cm, H_0 = 17 cm	Results reported: Solids volume fraction

		Particle: Glass ballotini, d_p= 593, 521, 428, 268, 167, 154 µm, ρ_p= 2.5 g/cm^3 Ceramics, d_p= 605, 463 µm, ρ_p= 3.8 g/cm^3 Steel shots, d_p= 468, 439 µm, ρ_p= 7.6 g/cm^3		Observation: A model was proposed to predict the solids volume fraction in a density or size segregating mixture and the results were compared with that obtained from sieve analysis of the de–fluidized bed.
Numerical studies				
Reference	Model	Computations	Validation	Comments
Bokkers et al. [23]	CFD–DEM Drag: Gidaspow, HKL Contact: Soft and hard sphere e = 0.97, ν = 0.1 In-house code	Geometry: Rectangular 2D Bed ($L \times B \times H$) = 15×1.5×100 cm Particle: d_p= 1500, 2500 µm, ρ_p= 2.526 gm/cm^3, N_p= 30000, 40000	Measurement technique/ experimental study: PIV Results compared: Qualitative profile of single bubble, Relative segregation	Observation: The extent of mixing and segregation induced by a single bubble in mono and bi–dispersed fluidized beds was studied using the PIV and DEM simulations.

Cooper and Coronella [31]	Eulerian–Eulerian Drag: Gidaspow Momentum exchange: Syamlal – O'Brien e = 0.97, ν = 0.1 Fluent 6.0	Geometry: Rectangular 2D Bed ($L \times H$) = 15×80 cm Particle: d_p= 355, 69.5 µm, ρ_p= 1.8, 4.8 gm/cm^3	Measurement technique/ experimental study: Laputz [124] Results compared: Mass fraction	Observation: The influence of bubble particularly the bubble wake in the mixing of solids was analyzed.
Huilin et al. [118]	Multi–fluid model with KTGF and CFD–DEM Drag: Gidaspow TFM with KTGF e = 0.95, Δt = 10^{-5} s CFD–DEM Contact: Hard sphere e = 0.9, 0.95, 0.99, Δt = 10^{-5} s In–house code	Multi–fluid model with KTGF Geometry: Rectangular 2D Bed ($L \times H$)=30×150 cm Grid ($L \times H$)=0.61×1.875 cm Particle: d_p= 1000, 3000 µm, ρ_p= 1.2, 1.6 gm/cm^3, H_0= 40 cm CFD–DEM Geometry: Rectangular 2D Bed ($L \times H$) = 15×65 cm	Measurement technique/ experimental study: Formisani et al. [125] Hulin et al. [126] Results compared: Mass fraction of particles, Mean particle diameter	Additional results: Instantaneous qualitative profile of porosity and particle velocity, Particle volume fraction, Particle velocity, Granular temperature, Segregation coefficient Observation: Particle segregation phenomena with jetsam settling at bottom and flotsam moving at the top was predicted by both TFM and DEM and

		Grid ($L \times H$)=1×1.18 cm Particle: d_p= 1000, 2300, 3000, 4260 µm, ρ_p = 1.4, 2.6 gm/cm^3, N_p= 2200		fluctuating component of particle velocity was higher in vertical direction than in lateral direction.
Fan and Fox [119]	Multi-fluid model with DQMOM Drag: Gidaspow e = 0.97 MFiX code	Binary PSD´ Geometry: Rectangular 2D Bed ($L \times H$) = 15×50 cm Grid ($L \times H$)= 0.5×0.625 cm Particle: d_p = 1500, 2500 µm, ρ_p = 2.526 gm/cm^3 Continuous PSD´ Geometry: Rectangular 2D Bed ($L \times H$) = 10×50 cm Particle: ρ_p = 2.525 gm/cm^3	Measurement technique/ experimental study: Goldschmidt et al. [113] Dahl and Hrenya [120] Results compared: Relative segregation (Binary PSD´) Normalized mean diameter and standard deviation of local PSD´ (Continuous PSD´, compared the results obtained from DEM simulation of Dahl and Hrenya)	Observation: A multi-fluid model based on the EE methodology and DQMOM was proposed for the continuous PSD´. Initially, predictions for binary PSD´ were compared and subsequently, DQMOM was proposed for the continuous PSD´.

Di Renzo et al. [121]	CFD–DEM Drag: Di Felice e = 0.9, ν = 0.3 In–house code	Geometry: Rectangular 2D Bed $(L \times B \times H)$ = 4×0.0433×15 cm Particle: d_p= 433 µm, ρ_p= 2.48, 7.6 gm/cm^3, N_p= 15000	Measurement technique/ experimental study: Sieve analysis Results compared: Mixing index	Observation: Mixing map that can determine the extent of mixing for the given particles differing in density, and at a given superficial velocity.
Peng et al. [27]	CFD–DEM Drag: Di Felice k = 10 N/m, e = 0.9, ν = 0.3 In–house code	Geometry: Rectangular 2D Bed $(L \times H)$ = 1.5×15, 2×20 cm Grid $(L \times H)$ = 1×1 cm Particle: Species 1, d_p= 116 µm, ρ_p= 0.939, 2.462, 3.287, 6.949, 8.057 g/cm^3 Species 2, d_p= 234, 278, 328, 393 µm, ρ_p= 0.939 g/cm^3	Measurement technique/ experimental study: Sieve analysis Results compared: Mixing index	Observation: A comprehensive parametric study was performed to study the effect of different operating condition on mixing index.
Olaofe et al. [28]	CFD–DEM and Multi–fluid model	Geometry: Rectangular 2D	Measurement technique/ experimental study:	Observation:

	CFD–DEM Drag: Gidaspow, BVK Contact: Soft sphere k = 9000 N/m, e = 0.97, ν = 0.1, Δt = 10^{-4}-10^{-5} s In–house code Multi–fluid model Drag: Gidaspow e = 0.88, Δt = 10^{-5} s	Bed ($L \times B \times H$) = 15×1.5×100 cm Grid ($L \times B \times H$) = 0.33 × 1.5 × 0.33 cm Particle: d_p= 1500, 2500, 3500 µm, ρ_p= 2.526 gm/cm^3, N_p= 33690–101080	Goldschmidt et al. [113] Olaofe et al. [26] Results compared: Extent of segregation	Extensive CFD–DEM simulations were performed to predict the extent of mixing and segregation under different operating conditions and these predictions were closer than that obtained from MFM.
Fotovat et al. [122]	CPFD Drag: Ganser e = 0.95 Weight % of biomass = 2, 8, 16 % $\mathbf{U}_g$ = 30–80 cm/s Barracuda framework	Geometry: Cylindrical Bed ($d_p \times H$) = 15.2×300 cm Grid ($L \times H$) = 1.52×3.26 cm Particle: Sand, d_p = 380 µm, ρ_p= 2.65 g/cm3, Biomass, $d_p \times L$ = 6.35×12.7 mm, ρ_p = 0.824 g/cm^3	Measurement technique/ experimental study: Optical fibre Results compared: Bubble size and bubble velocity	Observation: Statistical analysis with 1st, 2nd, and 3rd moment of bubble size and velocity were compared for different biomass loading and superficial velocity.

2.6. **Summary**

The hydrodynamic of the bubbling fluidized bed has been extensively studied. However, after analyzing the past experimental and computational studies, the following shortcomings are noticed.

1) Most of the mono–dispersed experimental studies have considered the single size/ narrow size distribution of particles. Whereas, solids in industries generally have wide size distribution.
2) Most of the studies have used the probes such as optical or capacitance to measure the gas/ solids volume fraction, which affects the local hydrodynamics of BFB.
3) Imaging can only capture the flow pattern along the walls, and therefore, these measurements are limited to a pseudo 2D rectangular bed.
4) High temporal and spatial resolution is required to measure the hydrodynamics in gas-solid BFB. Most of the non–invasive techniques lack either in temporal or spatial resolution. For instance, ECT/ ECVT has poor spatial resolution whereas, X-ray and γ–ray have poor temporal resolution.
5) EE model to simulate the gas-solid BFB is mostly used in the previous studies. Solids are inherently assumed as a continuum, thus, requiring closure models to determine the solid-solid and gas-solid interaction. The empiricism in these closure models can affect the EE predictions.
6) EL model removes the empiricism of closure model determining the solid-solid interaction by considering the solids as actual particles. However, the gas-solid interaction is still determined by empirical correlation.
7) The requirement of high computational power limits the usage of EL simulations, and therefore, a limited number of particles can be used to

simulate the EL model. Consequently, either a small domain or large particle size system can only be simulated.

8) Most of the simulations have been validated by comparing either the flow pattern or mean values. The validation of fluctuations such as granular temperature representing the turbulence in BFB could result in the higher discrepancy.
9) Transient study of mixing from segregated to mixed state and contribution of the bubble to reach the steady state mixing is limited.
10) Most of the studies, either experiments or simulations have considered spherical particles. However, irregular shape particles are commonly encountered in practice. Particles of different shape will project different area on the gas flow thereby, resulting in different drag force experienced by the particles. Therefore, a shape factor of irregularly shaped particles will dominate the hydrodynamics of BFB.
11) Solid particles in some processes are not only irregular but also porous such as biomass particles in pyrolysis. Consequently, computational studies performed considering such solid particles as spherical and non–porous could result in the wide discrepancy.
12) Agglomeration/ attrition of particles during fluidization is not considered in most of the studies.
13) Scale up studies of the fluidized bed are limited. The industrial fluidized bed are designed and scale up either based on either empirical correlation or experiments conducted on small scale geometry. Scaling up of reactors may not yield the desired results because of the heterogeneous nature of gas-solid fluidized bed.

Since the conceptualization of BFB in 1926, understanding of the characteristics of BFB and the factors affecting has improved a lot. However, there are still many shortcomings in the present knowledge. This thesis tries to cover certain limitations so that, our understanding of the hydrodynamics of BFB could be enhanced.

3 Effect of drag models on CFD-DEM predictions of mono-dispersed BFBs

"Reproduced from V. Agrawal, Y.H. Shinde, M.T. Shah, R.P. Utikar, V.K. Pareek, J.B. Joshi, Effect of drag models on CFD–DEM predictions of bubbling fluidized beds with Geldart D particles, Adv. Powder Technol. 29 (2018), 2658–2669. Copyright [2018] The Society of Powder Technology Japan"

3.1. Introduction

The literature review (chapter-2) suggested that the available gas-solid flow models, both EE and EL models, require a gas-solid drag closure, for which several different models have been proposed to cater different flow conditions. The models have been derived by using empirical, semi-empirical, theoretical and direct numerical simulation (DNS) methods. This study investigates the effect of six different drag models (Di Felice, Syamlal-O'Brien, Gidaspow, EMMS, BVK and Ayeni models) on flow predictions by conducting CFD-DEM simulations of mono-dispersed BFBs.

In CFD–DEM, the flow of solids is resolved by solving the force balance equation, which includes the gravity, drag, contact, and other forces around each discrete particle. The drag represents interphase exchange force between the gas and solids, and modeling it accurately is vital for reliable predictions [44,48,49]. Several drag models have been proposed in the literature, which can be classified into five categories: (i) those derived from the pressure drop in packed bed experiments (Ergun [39], Gibilaro [127,128] and Ayeni [44]), (ii) those obtained by correcting single particle drag models using settling experiments (Wen-Yu [40], Di Felice [129] and Syamlal–O'Brien [41]), (iii) hybrid models (Gidaspow [42]) , (iv) multi-scale models (e.g., energy minimization multi-scale (EMMS) [130] and sub-grid scale filter [131–

133], and (v) those derived from direct numerical simulations (HKL [116,117], BVK [43] and Tenneti et al. [134,135]). These models differ in their derivation method and applicability to different types of gas-solid flows.

As a result, many CFD studies have been conducted to investigate the effect of drag models on flow predictions [44,46–51,136–142]. Most of these studies have used EE models, while a few studies have employed the CFD–DEM model (Li and Kuipers [51], Ku et al. [48], Ayeni et al. [44], Koralkar and Bose [49], Di Renzo et al. [143] and Zhang et al. [144]). Furthermore, the majority of previous studies were conducted for either Geldart A or B particles. Only Ayeni et al. [44], Koralkar and Bose [49] and Ku et al. [48] have investigated the effect of drag models on CFD–DEM simulations of BFBs with Geldart D particles. The fluidization of different Geldart particles types manifests different behaviors [65,145–149] owing to the different relative magnitudes of inter-particle cohesive forces and interphase interactions in the bed [146]. Thus, simulation of particles from a particular Geldart group requires selection of an appropriate drag model. Ku et al. [48] assessed the Gidaspow, Di Felice, and HKL models, and concluded that their predictions for the pressure drop and its fluctuations agreed with each other. They observed that the Gidaspow model resulted in the lowest fluctuation frequency, whereas the Di Felice model resulted in the highest. Ayeni et al. [44] derived a new drag correlation based on the theoretical derivation of the gas-solid drag proposed by Joshi [150], and Pandit and Joshi [151]. The new model yielded a lower drag than the Gidaspow, and Syamlal–O'Brien model, thus resulting in lower bed expansion and showing reasonable quantitative agreement with the experimental data [56]. Koralkar and Bose [49] found that different drag models resulted in similar radial velocity profiles. However, the simulation predictions did not agree with the experimental data throughout the flow domain, and the local quantitative agreement

differed from case to case. Previous CFD–DEM studies [44,49] investigated drag models by simulating the NETL Challenge problem [56] over a limited range of fluidization velocities ($2 - 4\ \boldsymbol{U}_{mf}$). Thus, it is still necessary to assess drag models for a range of fluidization velocities. Furthermore, the previous two CFD–DEM studies [44,49] did not examine all available drag models.

Despite several studies, the origin of discrepancies in CFD predictions arising from the use of different drag models is largely unknown. As a result, the selection of drag models often depends on a trial and error approach. This study investigates the effect of drag models on CFD–DEM predictions by applying the Syamlal–O'Brien, Di Felice, Gidaspow, EMMS, BVK, and Ayeni models to simulate two different BFB systems (Goldschmidt et al. [13] and NETL challenge problem [56]). Both BFBs were pseudo-2D beds composed of Geldart D particles. Correlations of the drag models were first compared and analyzed. Then, CFD–DEM simulations were conducted, and predictions of the pressure drop, particle height, velocities, and granular temperature were compared with experimental data and critically analyzed.

3.2. Gas-solid drag models

Gas-solid drag represents the exchange of momentum that occurs between the two phases. Fundamentally, drag on a solid particle immersed in a fluid flow has two constituents: wall shear or skin drag, and form drag or fluid pressure in the direction of the flow [152]. Skin drag represents the friction between the particle surface and the fluid, whereas form drag represents the energy dissipation associated with boundary layer separation and formation of eddies or wakes [152]. In a gas-solid flow, the drag is typically represented as a combination of both the wall and form drag [152]. The drag force on a single isolated spherical particle can be written as follows:

$$\boldsymbol{f}_D = \frac{1}{2}\rho_G {U_{slip}}^2 A_P C_{D,\infty} = \frac{1}{2}\rho_G\left(|\boldsymbol{u}_G - \boldsymbol{u}_S|(\boldsymbol{u}_G - \boldsymbol{u}_S)\right)\frac{\pi}{4}{d_P}^2\, C_{D,\infty} \quad (1)$$

where $\boldsymbol{f}_D$ is the drag force, ρ_G is the density of the gas, U_{slip} is the slip velocity, A_P is the projected surface area of the particle, $C_{D,\infty}$ is the drag coefficient on a single particle in an infinite domain, $\boldsymbol{u}_G$ is the gas velocity, $\boldsymbol{u}_S$ is the solid velocity, and d_P is the particle diameter. The value of $C_{D,\infty}$ depends on the particle Reynolds number. At low particle Reynolds numbers ($Re_P \ll 1$), $C_{D,\infty}$ is calculated using Stokes' law [153] as $24/Re_P$ [154]. At high Re_P, the empirical correlations proposed by Schiller and Naumann [155] and DallaValle [156] are generally used to calculate $C_{D,\infty}$. For the drag force on single particle in a multi-particle system, the correlation for $C_{D,\infty}$ is modified (henceforth referred to as $C_{D,H}$), and a correction factor (CF) is introduced to account for the effect of neighboring particles, as follows:

$$\boldsymbol{f}_{D,H} = CF\ \frac{1}{2}\rho_G(|\boldsymbol{u}_G - \boldsymbol{u}_S|_H(\boldsymbol{u}_G - \boldsymbol{u}_S)_H)\ \frac{\pi}{4}{d_P}^2\, C_{D,H} \quad (2)$$

Where the subscript H represents the hindered flow condition. To represent the drag on all particles in a unit control volume, Eq. (2) is further modified as:

$$\boldsymbol{F}_D = CF\ \frac{1}{2}\rho_G(|\boldsymbol{u}_G - \boldsymbol{u}_S|_H(\boldsymbol{u}_G - \boldsymbol{u}_S)_H)\ \frac{\pi}{4}{d_P}^2\ C_{D,H}\left(\frac{\epsilon_S}{V_P}\right) =$$

$$\frac{3}{4}\frac{\rho_G\epsilon_S(|\boldsymbol{u}_G-\boldsymbol{u}_S|_H(\boldsymbol{u}_G-\boldsymbol{u}_S)_H)}{d_P}\left(CF\ C_{D,H}\right) \quad (3)$$

where ϵ_S is the volume fraction of solids, ϵ_G is the gas volume fraction, and V_P ($= \frac{\pi}{6}{d_P}^3$) is the volume of a single particle. The ratio $\frac{\epsilon_S}{V_P}$ represents the number of particles in a unit volume. In Eq. (3), both $C_{D,H}$ and CF are functions of ϵ_G, and the functional relationship can be derived either empirically or from direct numerical simulations. Different drag models have adopted various ways of applying $C_{D,H}$ and CF.

Table 3.1 Drag models applied to particles in a unit volume

$\boldsymbol{F}_D = \beta\lvert\boldsymbol{u}_G - \boldsymbol{u}_G\rvert$
β = interphase exchange coefficient
$Re_p = \frac{\rho_G\lvert\boldsymbol{u}_G - \boldsymbol{u}_S\rvert d_p}{\mu_G}$
Gidaspow [42]
$\beta_{Wen-Yu} = \frac{3}{4}C_{D,Wen-Yu}\frac{\rho_G\epsilon_G\epsilon_S\lvert\boldsymbol{u}_G - \boldsymbol{u}_S\rvert}{d_p}\epsilon_G{}^{-2.65}$ $\quad \epsilon_G \geq 0.8$
$\beta_{Ergun} = \frac{150\epsilon_S{}^2\mu_G}{\epsilon_G d_p{}^2} + \frac{1.75\rho_G\epsilon_S\lvert\boldsymbol{u}_G - \boldsymbol{u}_S\rvert}{d_p}$ $\quad \epsilon_G < 0.8$
$C_{D,Wen-Yu} = \frac{24}{(\epsilon_G Re_p)}\left(1 + 0.15(\epsilon_G Re_p)^{0.687}\right)$ $\quad Re_P < 1000$
$C_{D,Wen-Yu} = 0.44$ $\quad Re_P \geq 1000$
Syamlal-O'Brien [41]
$\beta_{S-B} = \frac{3}{4}\frac{C_{D,S-B}}{V_{rs}{}^2}\frac{\rho_G\epsilon_G\epsilon_S\lvert\boldsymbol{u}_G - \boldsymbol{u}_S\rvert}{d_p}$
$C_{D,S-B} = \left(0.63 + \frac{4.8}{\sqrt{Re_p/V_{rs}}}\right)^2$
$V_{rs} = 0.5\left(A - 0.06Re_p + \sqrt{(0.06Re_p)^2 + 0.12Re_p(2B - A) + A^2}\right)$
$A = \epsilon_G{}^{4.14}$
$B = a\epsilon_G{}^{1.28}$ $\quad \epsilon_G \leq 0.85$
$B = \epsilon_G{}^{b}$ $\quad \epsilon_G > 0.85$
where a and b are tuning parameters.
Di Felice [129]
$\beta_{Di\,Felice} = \frac{3}{4}C_{D,DallaValle}\frac{\rho_G\epsilon_S\lvert\boldsymbol{u}_G - \boldsymbol{u}_S\rvert}{d_p}f(\epsilon_G, Re_p)$
$C_{D,DallaValle} = \left(0.63 + \frac{4.8}{\sqrt{Re_p}}\right)^2$
$f(\epsilon_G, Re_p) = \epsilon_G{}^{-\gamma}$
$\gamma = 3.7 - 0.65exp\left(\frac{-(1.5-x)^2}{2}\right)$
$x = log_{10}(Re_p)$
BVK [43]
$\beta_{BVK} = 18\mu_G\epsilon_G\epsilon_S\frac{F_{BVK}}{d_p{}^2}$

$$F_{BVK} = 10\frac{\epsilon_S}{{\epsilon_G}^2} + {\epsilon_G}^2\left(1 + 1.5\sqrt{\epsilon_S}\right) + \frac{0.413(\epsilon_G Re_p)}{24{\epsilon_G}^2}\left(\frac{\left(\frac{1}{\epsilon_G}\right)+3\epsilon_G\epsilon_S+\left(\frac{8.4}{\left(\epsilon_G Re_p\right)^{0.343}}\right)}{1+\frac{10^{3\epsilon_S}}{\left(\epsilon_G Re_p\right)^{(0.5+2\epsilon_S)}}}\right)$$

EMMS [130]

$\beta_{Ergun} = \frac{150{\epsilon_S}^2\mu_G}{\epsilon_G {d_p}^2} + \frac{1.75\rho_G\epsilon_S\lvert\boldsymbol{u}_G-\boldsymbol{u}_S\rvert}{d_p}$	$\epsilon_G < 0.74$
$\beta_{EMMS} = \frac{3}{4}\frac{\rho_g\epsilon_G\epsilon_S\lvert\boldsymbol{u}_g-\boldsymbol{u}_s\rvert}{d_p}C_{D,Wen-Yu}\omega(\epsilon_G)$	$\epsilon_G \geq 0.74$
$\omega(\epsilon_G) = -0.5760 + \frac{0.0214}{4(\epsilon_G-0.7463)^2+0.0044}$	$0.74 < \epsilon_G <= 0.82$
$\omega(\epsilon_G) = -0.0101 + \frac{0.0038}{4(\epsilon_G-0.7789)^2+0.0040}$	$0.82 < \epsilon_G <= 0.97$
$\omega(\epsilon_G) = -31.8295 + 32.8295\epsilon_G$	$\epsilon_G > 0.97$

Ayeni [44]

$$\beta_{Ayeni} = \frac{3\rho_G{\epsilon_G}^2\epsilon_S\lvert\boldsymbol{u}_G-\boldsymbol{u}_S\rvert}{d_p}C_{D,Ayeni}$$

$$C_{D,Ayeni} = \frac{6}{Re_p}\left[\frac{3.6\epsilon_S}{{\epsilon_G}^4}+1\right] + 0.11\left[\frac{40.91K^2{\epsilon_S}^2}{{\epsilon_G}^2}+1\right]$$

$$K = \left[\frac{\boldsymbol{U}_{mf}}{\boldsymbol{U}_G} + \left(1-\frac{\boldsymbol{U}_{mf}}{\boldsymbol{U}_G}\right)*\left(1-\frac{\epsilon_S}{\epsilon_{S,mf}}\right)\right]$$

where $\boldsymbol{U}_G$ is the inlet superficial velocity of the fluid, $\boldsymbol{U}_{mf}$ is the minimum fluidizing velocity, and $\varepsilon_{S,mf}$ is the volume fraction of the solids at the minimum fluidizing condition.

The drag models analyzed in the present study are summarized in Table 3.1. The primary difference between these models is the calculation of *CF* and $C_{D,H}$. Figure 3.1 shows the effect of voidage on the normalized $CF\ C_{D,H}$ at three different particle Reynolds numbers (Re_P =100, 500, and 1000). In all the drag models studied, the value of $CF\ C_{D,H}$ was calculated as $CF\ C_{D,H} = \frac{\boldsymbol{F}_D}{\left(\frac{1}{2}\rho_G(\lvert\boldsymbol{u}_G-\boldsymbol{u}_S\rvert_H(\boldsymbol{u}_G-\boldsymbol{u}_S)_H)\frac{\pi}{4}{d_P}^2\left(\frac{\epsilon_S}{V_P}\right)\right)}$. The value of $CF\ C_{D,H}$ was then normalized by the $CF\ C_{D,H}$ in the Gidaspow model.

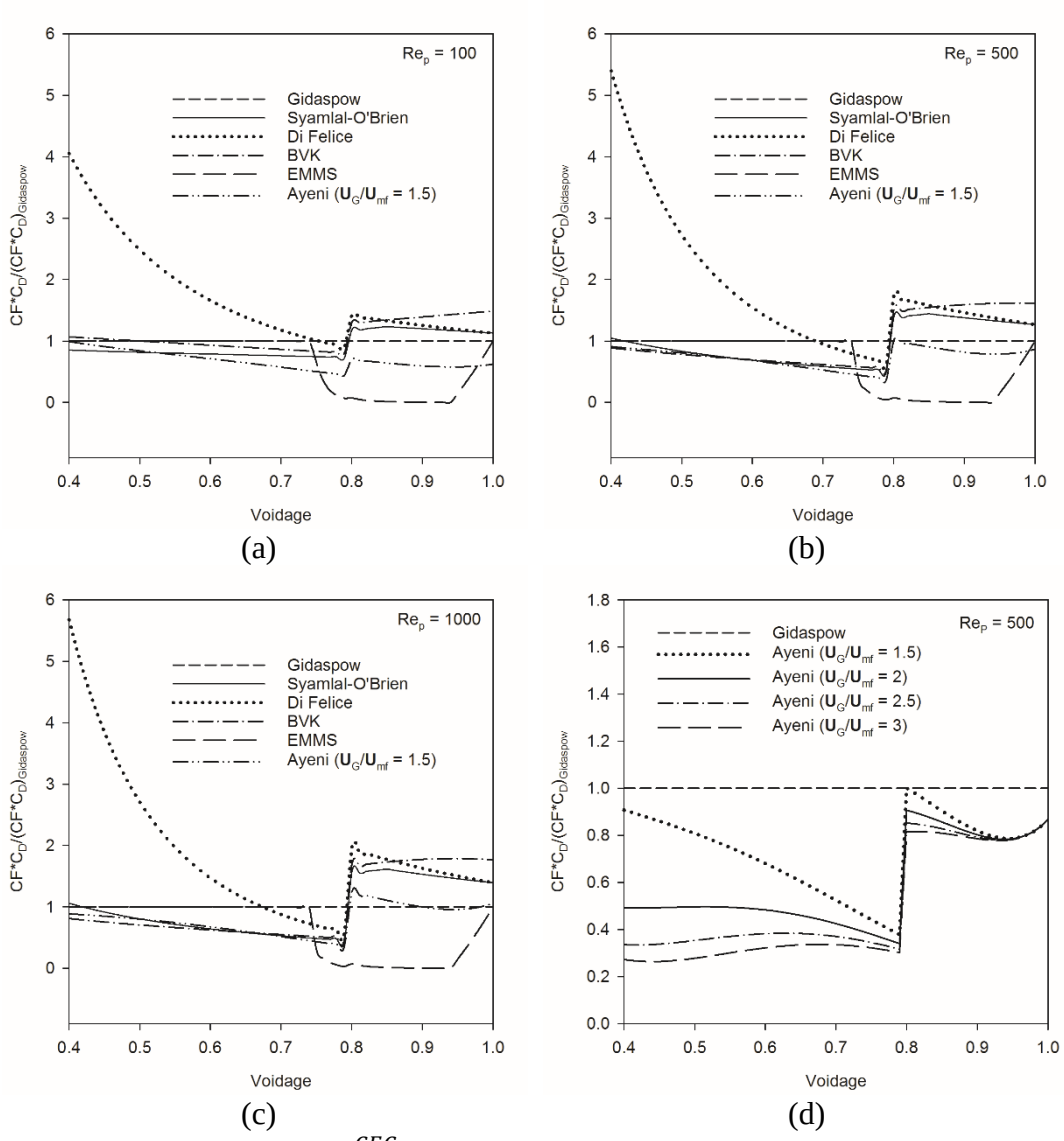

Figure 3.1 Variation in $\frac{CFC_{D,H}}{(CFC_{D,H})_{Gidaspow}}$ *with voidage at (a)* Re_p *= 100, (b)* Re_p *= 500, (c)* Re_p *= 1000, and (d)* Re_p *= 500 for the Ayeni model with* $\frac{U_G}{U_{mf}}$ *of 1.5, 2, 2.5, and 3*

The calculations were performed using the material properties (d_p = 3.256 mm, ρ_s =1131 kg/m^3, $\epsilon_{S,mf}$ = 0.45, and $\boldsymbol{U}_{mf}$ = 1.05 m/s) described in the NETL challenge problem. The Gidaspow model is a combination of the Wen-Yu [40] (ϵ_g > 0.8) and Ergun [39] (ϵ_g< 0.8) models (see Table 3.1), and it is discontinuous at the transition point (ϵ_g = 0.8). Consequently, the normalized $CF\ C_{D,H}$ undergoes an abrupt change at ϵ_g = 0.8. The values of $CF\ C_{D,H}$ in the Syamlal–O'Brien, and BVK models were

lower than the Gidaspow model for ϵ_G less than 0.8 and higher than the Gidaspow model for ϵ_G > 0.8. The Di Felice model resulted in a higher value for $CF\ C_{D,H}$ than the other models, which decreased exponentially with increasing voidage. The higher drag given by the Di Felice model can be attributed to a CF of ${\epsilon_G}^{-\gamma}$ (see Table 3.1), where γ varies from 3.12 to 3.48 with variation in Re_p from 100 to 1000. Further, the $C_{D,H}$ in the Di Felice model is the $C_{D,\infty}$ of DallaValle [156], whose value is also higher than the $C_{D,H}$ of the Gidaspow model for given Re_p and ϵ_G. The value of $CF\ C_{D,H}$ of the Syamlal–O'Brien model depends on tuning parameters (a and b) which need to be adjusted using the velocity and voidage at the minimum fluidization condition [157]. This tuning ensures that the model results in a single particle drag force at $\epsilon_g = 1$ and $\boldsymbol{U}_{mf}$ at $\epsilon_{S,mf}$. In this study, these tuning parameters were adjusted to 0.87 (a) and 2.12 (b) for the $\epsilon_{S,mf}$ and $\boldsymbol{U}_{mf}$ of the BFB system in the NETL challenge problem. The EMMS model resulted in values similar to those of the Gidaspow model over a voidage range of 0.4–0.74, while it yielded significantly lower values for ϵ_G > 0.74. Gas–solid flow in fluidized beds exhibits particle aggregation or formation of clusters. The gas must then flow around these clusters, which reduces the overall gas–solid drag. This reduction in drag is accounted for by the EMMS model. Hence, the drag calculated with the EMMS model is lower than the other models [158]. The Ayeni model slightly underestimated the Gidaspow model at an inlet fluidization velocity ($\boldsymbol{U}_G$) of 1.5$\boldsymbol{U}_{mf}$. The Ayeni model uses the ratio $\frac{\boldsymbol{U}_G}{\boldsymbol{U}_{mf}}$ in the correlation for $C_{D,H}$. The impact of the $\frac{\boldsymbol{U}_G}{\boldsymbol{U}_{mf}}$ ratio on $CF\ C_{D,H}$ at a constant Re_P of 500 is shown in Figure 3.1 (d). The value of $CF\ C_{D,H}$ decreased with increasing inlet gas velocity. At $\frac{\boldsymbol{U}_G}{\boldsymbol{U}_{mf}}$ = 3, the value of $CF\ C_{D,H}$ was ~5 times lower than that of the Gidaspow model for ϵ_G < 0.8.

The difference in the drag models can be perceived as differences in the value of $CF\ C_{D,H}$ which in turn depend on ϵ_G and Re_P. Both these parameters vary with the local hydrodynamics inside a BFB. Most drag models are derived by assuming homogeneous fluidization, whereas the EMMS and Ayeni models consider the heterogeneous nature of the fluidized bed. The EMMS model accounts for the formation of clusters, and the Ayeni model considers the suppression of bed expansion caused by energy dissipation under turbulent conditions. While explicit comparison of the drag models is helpful, their impact on the prediction of flow structures can only be investigated by conducting CFD simulations.

3.3. **CFD–DEM model**

This study uses the CFD–DEM gas-solid flow model implemented in the MFiX–DEM code [94–96]. The governing equation of gas and solid phase and the computation of drag and collisional force are given below

3.3.1. Governing equation of gas phase

The equation defining the conservation of mass and momentum of the gas phase, without considering phase change, chemical reaction, growth, aggregation and breakage phenomena are

Conservation of mass

$$\frac{\partial(\epsilon_G \rho_G)}{\partial t} + \nabla.(\epsilon_G \rho_G \boldsymbol{u}_G) = 0$$

Conservation of momentum

$$\frac{D}{Dt}(\epsilon_G \rho_G \boldsymbol{u}_G) = \nabla . \overline{\overline{S_G}} + (\epsilon_G \rho_G \boldsymbol{g}) - \boldsymbol{I}_{GS}$$

where $\boldsymbol{I}_{GS}$ is the gas–solid momentum transfer between gas and solid phase and $\overline{\overline{S_G}}$ is the gas–phase stress tensor, which is computed as

Gas–phase stress tensor

$$\overline{\overline{S_G}} = -P_G \bar{\bar{I}} + \overline{\overline{\tau_G}}$$

where P_G is the gas–phase pressure and $\overline{\overline{\tau_G}}$ is the gas–phase shear stress tensor given by

$$\overline{\overline{\tau_G}} = 2\mu_G \overline{\overline{D_G}} + \lambda_G \nabla . tr(\overline{\overline{D_G}}) \bar{\bar{I}}$$

and strain Rate Tensor, $\overline{\overline{D_G}}$ is given by

$$\overline{\overline{D_G}} = \frac{1}{2}[\nabla \boldsymbol{u}_G + (\nabla \boldsymbol{u}_G)^T$$

3.3.2. Governing equation of solid phase

Newton's equation of motion for discrete solid particles are

Translational force balance

$$m^{(i)} \frac{d}{dt}\left(\boldsymbol{u}_S^{(i)}(t)\right) = \boldsymbol{F}_T^{(i)} = m^{(i)}\boldsymbol{g} + \boldsymbol{F}_D^{(i\in k)}(t) + \boldsymbol{F}_C^{(i)}(t)$$

Where m is the mass of indivdual particle and i and k are particle and cell index respectively and $\boldsymbol{F}_D^{(i\in k)}$ is the total drag force (pressure + viscous) acting on i^{th} particle residing in k^{th}cell. $\boldsymbol{F}_C^{(i)}$ is the net contact force experienced by the i^{th} particle as a result of collision with the neighbouring particles and $\boldsymbol{F}_T^{(i)}$ is the total force on i^{th} particle (drag + contact + gravity) exerted by the neighbouring solid particles and gas in the k^{th} cell.

Rotational force balance

$$I^{(i)}\frac{\partial}{\partial t}\left(\boldsymbol{\omega}_S^{(i)}(t)\right) = \boldsymbol{T}^{(i)}$$

where $I^{(i)}$, $\boldsymbol{\omega}_S^{(i)}$ is the moment of inertia and angular velocity of i^{th} particle and $\boldsymbol{T}^{(i)}$ is the sum of all torques acting on the i^{th} particle.

3.3.3. Closure models

Gas-solid drag force

The governing equations of the two phases are coupled through an interphase drag. The Gas phase velocity interpolated to the i^{th} particle position, and i^{th} particle velocity is used to calculate the drag force on each particle residing in k^{th} cell. For simplicity, pressure is evaluated at the cell centre.

Drag force on i^{th} particle

$$\boldsymbol{F}_D^{(i\in k)} = -\nabla P_G\left(x^{(k)}\right)V_p{}^{(i)} + \frac{\beta^{(i)}V_p{}^{(i)}}{\varepsilon_S^{(k)}}\left(\boldsymbol{u}_G\left(\boldsymbol{X}^{(i)}\right) - \boldsymbol{u}_S^{(i)}\right)$$

where $\boldsymbol{u}_G\left(\boldsymbol{X}^{(i)}\right)$ is the mean velocity of gas–phase in k^{th} cell interpolated to i^{th} particle location and $\boldsymbol{u}_S^{(i)}$ is the velocity of i^{th} particle. $\boldsymbol{F}_D^{(i\in k)}$ is the drag on discrete i^{th} particle residing in a k^{th} cell. An equal and opposite drag force will be experienced by the gas phase as well. The average drag force $\boldsymbol{I}_{GS}$ experienced by the gas in k^{th} cell, exerted by all the particles residing in that cell is given by

Gas-solid momentum transfer on gas phase in k^{th} computational cell

$$\boldsymbol{I}_{GS} = -\epsilon_S^{(k)}\nabla P_G\left(x^{(k)}\right) + \frac{1}{\vartheta^{(k)}}\sum_{i=1}^{N_p^{(k)}}\frac{\beta^{(i)}V_p{}^{(i)}}{\varepsilon_S^{(k)}}\left(\boldsymbol{u}_G\left(\boldsymbol{X}^{(i)}\right) - \boldsymbol{u}_S^{(i)}\right)$$

$N_p^{(k)}$ is number a of particles residing in k^{th} computational cell and $\vartheta^{(k)}$ is the volume of k^{th} cell.

Solid–solid contact force

Both particle-particle and particle-wall collisions are modeled using the soft sphere approach [37], in which the overlap between two particles is represented as a spring and dashpot system. The spring causes elastic collisions, and the dashpot represents the dissipation of kinetic energy due to inelastic collisions. Parameters such as the spring constant, restitution coefficient, and friction coefficient are used to calculate contact forces. The implementation of this soft sphere model in MFiX – DEM is shown in Table 3.2

Table 3.2 Contact force model implemented in MFiX-DEM [94]

$\boldsymbol{F}_C^{(i)}(t) = \sum_{\substack{j=1 \\ j\neq i}}^{N}\left(\boldsymbol{F}_{C,n}^{(ij)}(t) + \boldsymbol{F}_{C,t}^{(ij)}(t)\right)$
$\boldsymbol{T}^{(i)}(t) = \sum_{\substack{j=1 \\ j\neq i}}^{N}\left(L^{(i)}\boldsymbol{\eta}^{(ij)} \times \boldsymbol{F}_t^{(ij)}(t)\right)$
Normal contact force
$\boldsymbol{F}_{C,n}^{(ij)}(t) = \boldsymbol{F}_{s,n}^{(ij)}(t) + \boldsymbol{F}_{d,n}^{(ij)}(t)$
Tangential contact force
$\boldsymbol{F}_{C,t}^{(ij)}(t) = \boldsymbol{F}_{s,t}^{(ij)}(t) + \boldsymbol{F}_{d,t}^{(ij)}(t)$
where $\boldsymbol{F}_{s,n}^{(ij)}$ and $\boldsymbol{F}_{d,n}^{(ij)}$ represents spring and dashpot force between particle 'i' and 'j' in the normal direction
Normal spring contact force
$\boldsymbol{F}_{s,n}^{(ij)}(t) = -k_n\delta_n\boldsymbol{\eta}^{(ij)}$
Normal overlap between particles
$\delta_n = 0.5(d_p^{(i)} + d_p^{(j)}) - \lvert\boldsymbol{X}^{(i)} - \boldsymbol{X}^{(j)}\rvert$
Unit vector along the line of contact pointing from particle 'i' to particle 'j'
$\boldsymbol{\eta}^{(ij)} = \frac{\boldsymbol{X}^{(j)}-\boldsymbol{X}^{(i)}}{\lvert\boldsymbol{X}^{(j)}-\boldsymbol{X}^{(i)}\rvert}$
Tangential spring contact force
$\boldsymbol{F}_{s,t}^{(ij)}(t) = -k_t\boldsymbol{\delta}_t$
Tangential displacement 'δ_t'

$$\boldsymbol{\delta}_t = \boldsymbol{u}_{S,t}^{(ij)}\, min\left(\frac{|\delta_n|}{\boldsymbol{u}_S^{(ij)}.\boldsymbol{\eta}^{(ij)}}, \Delta t\right)$$

where $\boldsymbol{u}_{S,t}^{(ij)}$ is the relative velocity of point of contact between particle 'i' and 'j' in tangential direction.

The relative velocity of the point of contact between particle 'i' and 'j'

$$\boldsymbol{u}_S^{(ij)} = \boldsymbol{u}_S^{(i)} - \boldsymbol{u}_s^{(j)} + \left(L^{(i)}\boldsymbol{\omega}_S^{(i)} + L^{(j)}\boldsymbol{\omega}_S^{(i)}\right) \times \boldsymbol{\eta}^{(ij)}$$

where $L^{(i)}$and $L^{(j)}$ are the distance of contact point from the center of particle 'i' and 'j' respectively.

$$L^{(i)} = \frac{|\boldsymbol{X}^{(j)} - \boldsymbol{X}^{(i)}|^2 + 0.25*\left(d_p^{(i)^2} - d_p^{(j)^2}\right)}{2|\boldsymbol{X}^{(j)} - \boldsymbol{X}^{(i)}|}$$

$$L^{(j)} = \left|\boldsymbol{X}^{(j)} - \boldsymbol{X}^{(i)}\right| - L^{(i)}$$

Normal '$\boldsymbol{u}_{S,n}^{(ij)}$' and tangential '$\boldsymbol{u}_{S,t}^{(ij)}$' component of contact velocity respectively are

$$\boldsymbol{u}_{S,n}^{(ij)} = \boldsymbol{u}_S^{(ij)}.\boldsymbol{\eta}^{(ij)}\boldsymbol{\eta}^{(ij)} \equiv \left(\boldsymbol{u}_S^{(i)} - \boldsymbol{u}_S^{(j)}\right).\boldsymbol{\eta}^{(ij)}\boldsymbol{\eta}^{(ij)}$$

$$\boldsymbol{u}_{S,t}^{(ij)} = \boldsymbol{u}_S^{(ij)} - \boldsymbol{u}_S^{(ij)}.\boldsymbol{\eta}^{(ij)}\boldsymbol{\eta}^{(ij)}$$

Tangential contact force when $\left(\boldsymbol{F}_t^{(ij)}| > \nu|\boldsymbol{F}_n^{(ij)}|\right)$ is true. In this case sliding is assumed to occur.

$$\boldsymbol{F}_t^{(ij)} = -\nu\left|\boldsymbol{F}_n^{(ij)}\right|\boldsymbol{t}^{(ij)} \qquad if\ \boldsymbol{t}^{(ij)} \neq 0$$

$$\boldsymbol{F}_t^{(ij)} = -\nu\left|\boldsymbol{F}_n^{(ij)}\right|\frac{\delta_t}{|\delta_t|} \qquad if\ \boldsymbol{t}^{(ij)} = 0, \delta_t \neq 0$$

$$\boldsymbol{F}_t^{(ij)} = 0 \qquad otherwise$$

Tangent to the plane of contact

$$\boldsymbol{t}^{(ij)} = \frac{\boldsymbol{u}_{S,t}^{(ij)}}{|\boldsymbol{u}_{S,t}^{(ij)}|}$$

3.4. **Simulation setup**

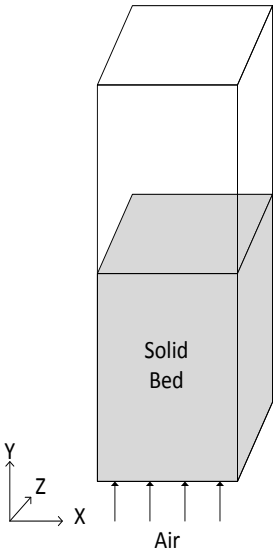

	System-1 Goldsmith et al. (2004)		System-2 NETL Challenge	
Dimensions (x×y×z) (m)	0.15×0.70×0.015		0.23×1.22×0.76	
N_p	24480		92276	
d_p (mm)	2.49		3.256	
ρ_p (kg/m^3)	2526		1131	
$\boldsymbol{U}_{mf}$ (m/s)	1.25		1.05	
Collision properties	Part-part	Part-wall	Part-part	Part-wall
Coeff. of normal restitution	0.97	0.97	0.84	0.92
Coeff. of friction	0.1	0.09	0.35	0.35
Grid size (x×y×z) (mm^3)	5×5×5		6.6×6.5×6.9	
$\boldsymbol{U}_G$ (m/s)	1.56, 1.88, 2.50		2.19, 3.28, 4.38	

Figure 3.2 Schematic diagram of the pseudo-2D fluidized bed

Simulations were conducted for pseudo-2D fluidized beds. A schematic diagram of the beds, along with their dimensions, flow conditions, material properties and initial conditions is shown in Figure 3.2. A uniform Cartesian grid was used to discretize the flow domain. At the bottom of the bed, the gas entry had a uniform flow rate. The atmospheric pressure was applied at the top of the bed. Transient simulations were conducted using a fluid time step of 0.0001s. The particle time step in the MFiX–DEM code is implicitly calculated from the normal component of both the restitution coefficient and the spring constant. As drag is the dominant force, the spring stiffness constant does not significantly affect particle motion [81,95]. Therefore, a spring constant of 800 N/m was used to reduce computational effort. Other collision properties such as the coefficient of restitution and coefficient of friction are dependent on the material properties of the solids. The values used for these collision properties were given by Goldschmidt et al. [13] and the NETL challenge problem [56]. A

tangential to normal spring constant ratio of 1/3 was applied. Second-order spatial discretization was used for the gas phase, while first-order and second-order temporal discretization was used for the gases and solids, respectively.

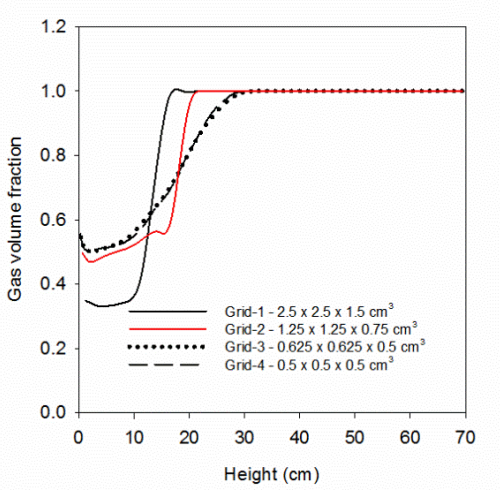

Figure 3.3 Effect of grid size on the axial profile of the gas volume fraction

To ensure a grid-independent solution, the BFB system from Goldschmidt et al. was simulated with four different grid sizes. The effect of the grid size on the time-averaged axial profile of the gas volume fraction is shown in Figure 3.3, which shows that the variation in the predictions decreased with a reduction in grid size. Predictions for two fine grid sizes, grids 3 and 4, showed minor differences. In addition, grids 1–4 resulted in average particle heights (Eq. 4) of 6.68, 8.84, 9.95 and 9.84 cm respectively. Thus, a grid of 0.5 (x) × 0.5 (y) × 0.5 (z) cm^3 was used for the simulations. A similar parametric study was conducted to determine the time required to reach steady state. A flow time of 15 s with time-averaging for the last 10 s was found to be sufficient to ensure steady state results.

3.5. **Results and discussion**

3.5.1. Simulation results for BFB system in Goldschmidt et al.

Goldschmidt et al. [13] obtained experimental bed expansion data with a high-speed imaging technique. A qualitative comparison of the bubble eruption observed in the experiments and in the current simulations at three inlet gas velocities is shown in Figure 3.4. Both the experimental and simulation results are for the same instant in the eruption of a bubble. At $1.25\boldsymbol{U}_{mf}$ and $1.5\boldsymbol{U}_{mf}$ (Figure 3.4 (a)), only the Di Felice, and Syamlal–O'Brien models produced a bed expansion similar to that of the experiments. The other drag models (Figure 3.4 (a), (b)) resulted in slight fluidization without the formation of bubbles and with the bed merely fluctuating around the initial condition. At $2\boldsymbol{U}_{mf}$ (Figure 3.4 (c)), all the drag models resulted in bed expansion with the formation of bubbles.

The qualitative comparison of bed heights at bubble eruption was analyzed further by comparing the average particle heights (Table 3.3). The instantaneous average particle height was calculated using the approach from Goldschmidt et al. [13]:

$$\langle h_p \rangle_{bed} = \frac{\sum_i^{N_p} h^{(i)}}{N_p} \tag{4}$$

where $\langle h_p \rangle_{bed}$ is the average particle height, $h^{(i)}$ is the axial position of the i^{th} particle, and N_p is the number of particles. In the simulations, $\langle h_p \rangle_{bed}$ was calculated from particle data captured at a frequency of 200 Hz, and these instantaneous particle height values were time-averaged to obtain the average particle height.

At all three gas velocities, the Di Felice model resulted in average particle heights that were close to the experimental values with discrepancies of less than 16% (Table 3.3). Simulation with the Syamlal–O'Brien model predicted average particle heights with

discrepancies in the range of 11–22%. At $2\boldsymbol{U}_{mf}$, the Gidaspow, BVK, EMMS, and Ayeni models yielded average particle heights in the range of 7–8 cm, which is close to the initial particle height of 7.5 cm and significantly less than the experimental value of 9.20 cm. At $1.5\boldsymbol{U}_{mf}$ and $2\boldsymbol{U}_{mf}$, all drag models except the Di Felice model resulted in average particle heights that were lower than the experimental values, with discrepancies as high as 25–45%. The higher particle height obtained with the Di Felice model can be explained by its higher estimation of drag compared to the other models (see Figure 3.1). The lower bed expansion with the Ayeni model can be attributed to the decrease in drag with increasing inlet gas velocity (Figure 3.1 (d)). The EMMS model resulted in average particle heights similar to that calculated with conventional models; at high solid volume fractions, the drag values from the EMMS and conventional models were similar (Figure 3.1). It should be noted that the predictions in the present study differ from those reported by Goldschmidt et al. [13]. This is because Goldschmidt et al. used a hard-sphere model for particle-particle collisions, whereas the present study applied a soft-sphere collision model

Table 3.3 Comparison of experimental data and simulation results for the average particle height

Models	Case 1: $1.25\boldsymbol{U}_{mf}$		Case 2: $1.5\boldsymbol{U}_{mf}$		Case 3: $2\boldsymbol{U}_{mf}$	
	Value (cm)	Discrepancy (%)	Value (cm)	Discrepancy (%)	Value (cm)	Discrepancy (%)
Exp.	9.20		11.40		13.50	
Syamlal–O'Brien	8.15	–11.41	8.98	–21.23	10.94	–18.96
Di Felice	10.60	15.22	11.55	1.32	13.20	–2.22
Gidaspow	7.28	–20.87	8.00	–29.82	9.84	–27.11
EMMS	7.28	–20.87	7.99	–29.91	10.06	–25.48
BVK	7.16	–22.14	7.64	–32.98	9.28	–31.26
Ayeni	7.93	–13.80	7.74	–32.11	7.42	–45.04

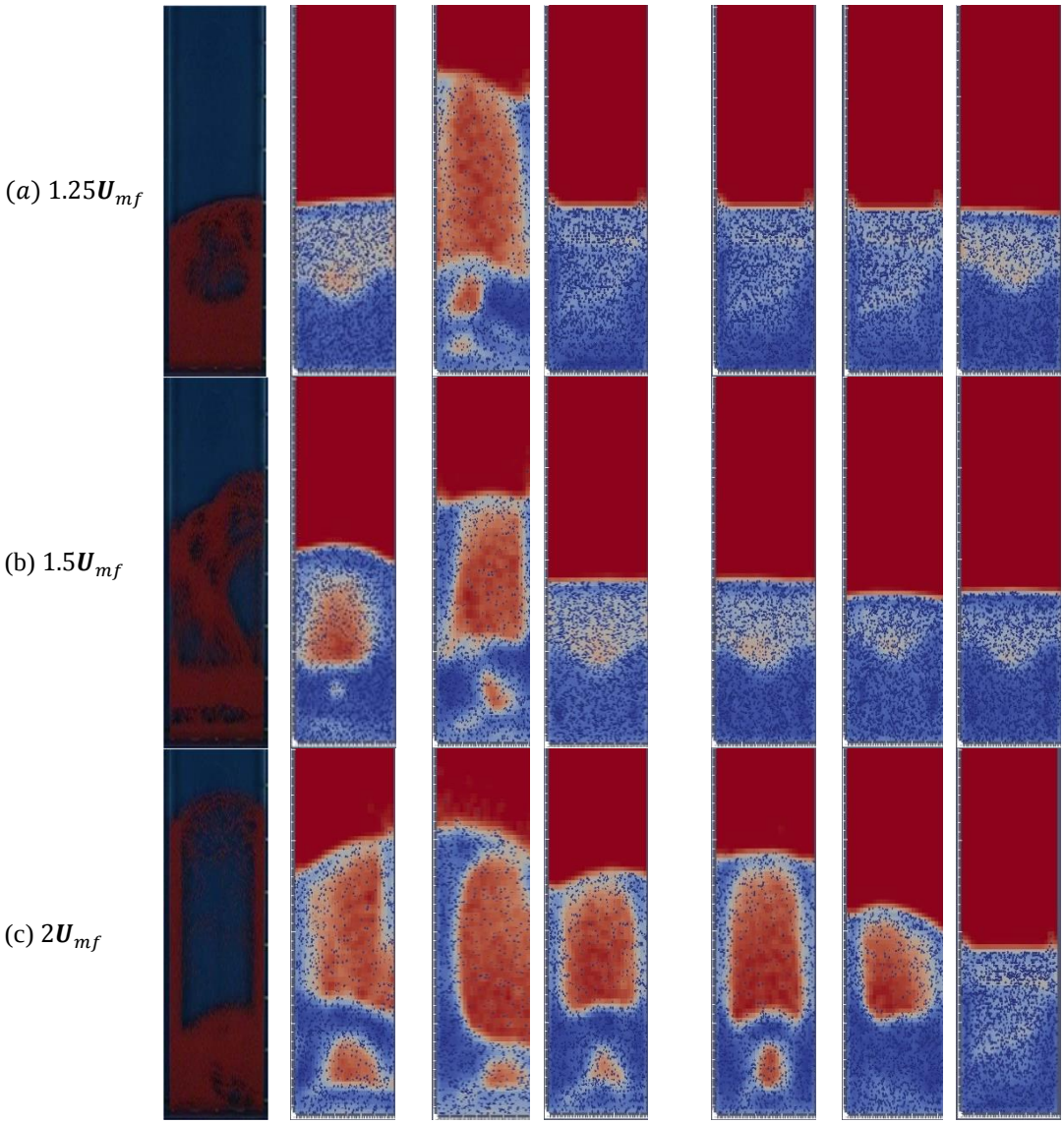

Figure 3.4 Instantaneous particle positions at bubble eruption for (a) $1.25\boldsymbol{U}_{mf}$*, (b)* $1.5\boldsymbol{U}_{mf}$*, and (c)* $2\boldsymbol{U}_{mf}$

3.5.2. Simulation results for NETL challenge problem

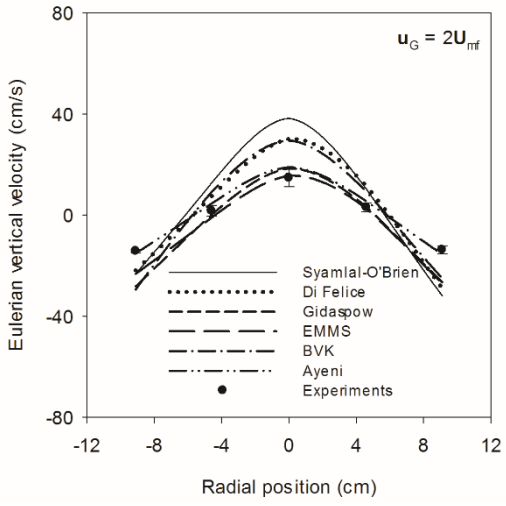

(a)

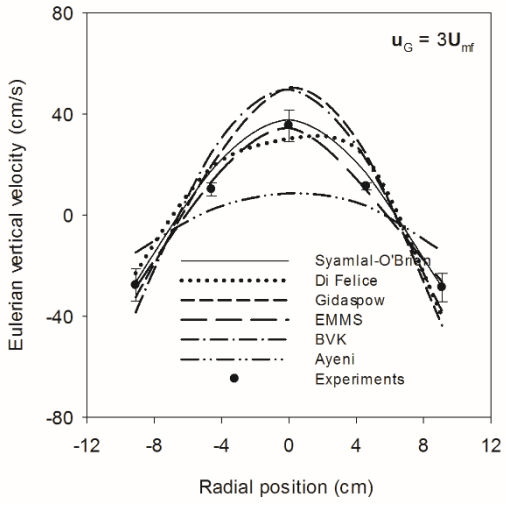

(b)

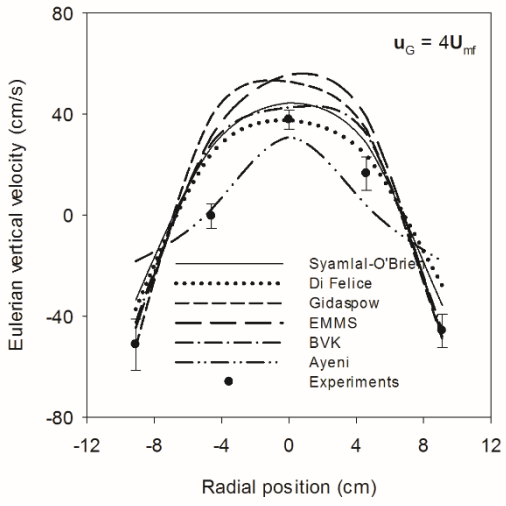

(c)

Figure 3.5 Radial profiles of the Eulerian vertical velocity of particles

The NETL challenge problem [56] provides a radial distribution of velocity and granular temperature obtained with high-speed particle image velocimetry. The NETL experiments were conducted at higher fluidization velocities ($2 - 4\boldsymbol{U}_{mf}$) and included more particles than the Goldschmidt et al. experiments; see Figure 3.2.

Figure 3.5 shows time-averaged radial profiles of the Eulerian vertical velocities of the particles. The Eulerian velocity was calculated by averaging the y-velocity of all individual particles in a given subsection at each time step. These velocities were calculated for five subsections (each 4.6 cm × 4.6 cm × 7.6 cm) at the height of 7.6 cm. All of the drag models were able to reproduce the core-annulus structure of the radial profiles. At $2\boldsymbol{U}_{mf}$ (Figure 3.5 (a)), the Gidaspow, EMMS, and Ayeni model results had good agreement with the three experimental data points at the center of the bed. However, for data points near the walls, only the Ayeni model showed good agreement. The Syamlal–O'Brien, Di Felice, and BVK models resulted in higher predicted values in the core region and lower values near the walls. At $3\boldsymbol{U}_{mf}$ (Figure 3.5 (b)), the Syamlal–O'Brien, EMMS, and Di Felice model results showed reasonable agreement at all radial positions. The Gidaspow, and BVK models resulted in higher predicted values in the core region and lower values near the wall. At $4\boldsymbol{U}_{mf}$, the Syamlal–O'Brien, Di Felice and BVK model results showed reasonable agreement at all radial positions; the Gidaspow and EMMS models resulted in overprediction in the core region. The Ayeni model exhibited significant underprediction in the core region at $3\boldsymbol{U}_{mf}$ and $4\boldsymbol{U}_{mf}$. This observation differs from the results reported by Ayeni et al. [44], which showed agreement at all three fluidization velocities. The reason for the discrepancy between the results of the present study and Ayeni et al. [44] is currently unknown and needs further investigation. It was observed in Section 3.5.1 that the Di Felice model resulted in higher bed expansion than the other drag models. As shown

in Figure 3.1, the Di Felice model results in higher drag than the other models at high solid volume fractions. However, for the NETL BFB system, the Di Felice model results showed good agreement with the experimental data as well as the simulation results for the other drag models.

Figure 3.6 shows the time-averaged radial profiles of the Eulerian horizontal velocities of particles. All of the drag models were qualitatively able to reproduce the experimental data. Quantitatively, however, only the Ayeni model results were reasonably comparable. At $2\boldsymbol{U}_{mf}$ and $3\boldsymbol{U}_{mf}$, all drag models, except the Ayeni model, overpredicted in one radial half of the bed and underpredicted in the other half. At $4\boldsymbol{U}_{mf}$, the EMMS and Ayeni models resulted in reasonable predictions. Interestingly, the Di Felice model, which resulted in reasonable predictions for the vertical velocity, did not provide close quantitative predictions for the horizontal velocity.

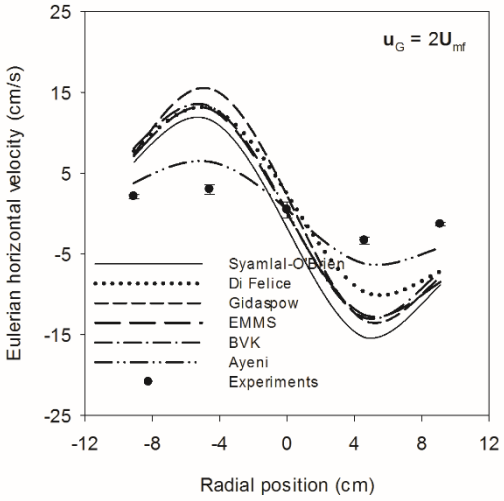

(a)

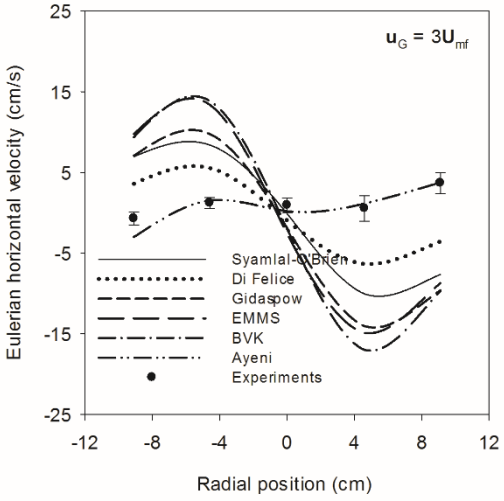

(b)

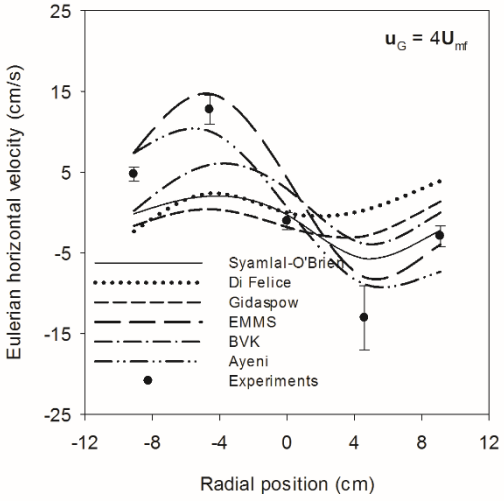

(c)

Figure 3.6 Radial profiles of the Eulerian horizontal velocity of particles

The time-averaged radial profiles of the granular temperature are shown in Figure 3.7. The granular temperature was calculated using the following equations:

$$\boldsymbol{u}_S^{(k)} = \frac{\sum_{i=1}^{N_p^{(k)}} \boldsymbol{u}_S^{(i\in k)}}{N_p^{(k)}} \tag{5}$$

$$\theta^{(k)} = \frac{\sum_{i=1}^{N_p^{(k)}} \left(\boldsymbol{u}_S^{(i\in k)} - \boldsymbol{u}_S^{(k)}\right)^2}{N_p^{(k)}} \tag{6}$$

where $\boldsymbol{u}_S^{(k)}$ is the mean of all particle velocities in the k^{th} subsection, $N_p^{(k)}$ is the number of particles in the k^{th} subsection and $\theta^{(k)}$ is the granular temperature calculated from all particle velocities, $\boldsymbol{u}_S^{(i)}$, in the k^{th} subsection of the bed.

The Ayeni model resulted in values closer to the experimental data at $2\boldsymbol{U}_{mf}$ and $3\boldsymbol{U}_{mf}$, but at $4\boldsymbol{U}_{mf}$, it resulted in lower values than the experimental data. All of the other drag models overpredicted the granular temperature by orders of magnitude. The discrepancies in the granular temperature predictions with the different drag models range from 1–517%. It should be noted that previous studies [44,49,87] did not compare simulation results with granular temperature data.

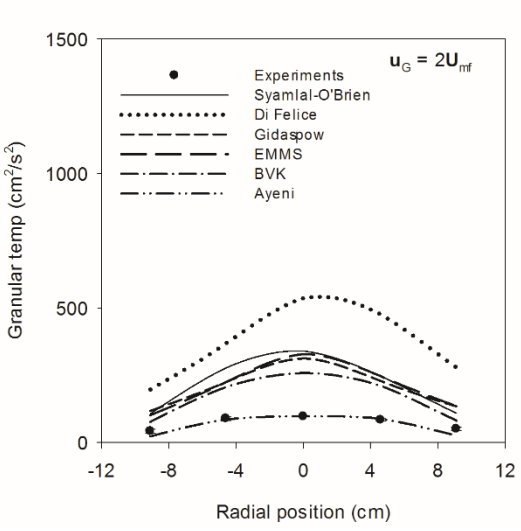

(a)

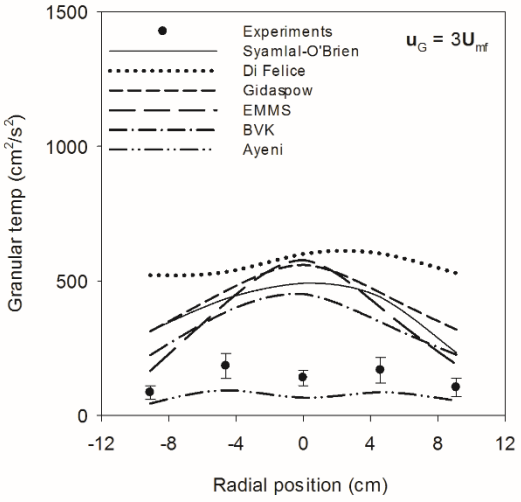

(b)

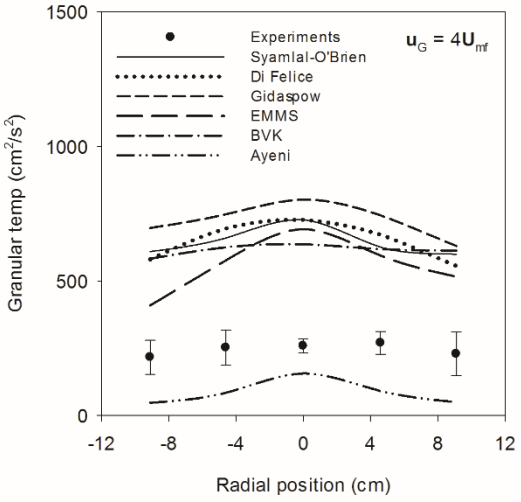

(c)

Figure 3.7 Radial profiles of the granular temperature

The time-averaged pressure drop between heights of 4.13 and 34.61 cm above the distributor for three fluidization velocities is shown in Figure 3.8. While simulations with the Syamlal–O'Brien, EMMS, and BVK models overpredicted the pressure drop at all three velocities, simulations with the Di Felice, and Gidaspow models underpredicted at $4\boldsymbol{U}_{mf}$ and overpredicted at $2\boldsymbol{U}_{mf}$ and $3\boldsymbol{U}_{mf}$. The Ayeni model results showed no change in pressure drop with the increase in fluidization velocity from 2 to $4\boldsymbol{U}_{mf}$. This is because the increase in pressure drop was compensated for by the decrease in drag force with increasing inlet gas velocity.

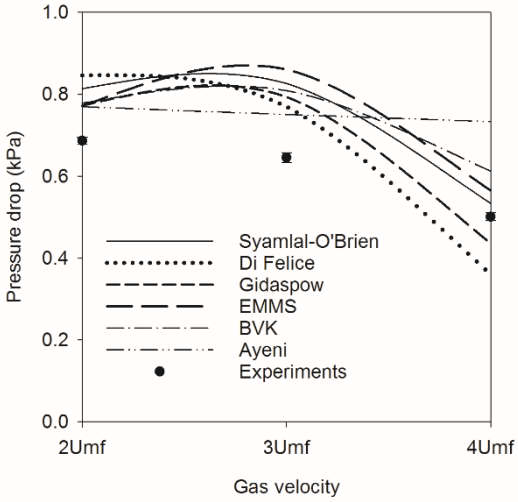

Figure 3.8 Pressure drop for different inlet gas velocities

3.5.3. Discussion

The CFD–DEM simulations using different drag models predicted similar qualitative trends, but there was significant variation in the predicted values. This inconsistency can be attributed to differences in the drag force. Both Re_p and ϵ_G depend on local flow conditions; hence, the drag force varies with location inside the bed. As a fluidized bed is a chaotic system, variation in the drag propagates over time and the flow domain. As a result, the simulations using different drag models resulted in differing predictions and exhibited dissimilar fluidization behavior. Further, none of the drag models resulted in consistent predictions for the two BFB systems considered

in this study. For example, the Di Felice model yielded reasonable predictions of the average particle height for the Goldschmidt et al. BFB system and Eulerian vertical velocity at $3\boldsymbol{U}_{mf}$ and $4\boldsymbol{U}_{mf}$ for the NETL system, but failed to replicate the experimental granular temperature and Eulerian horizontal velocity for the NETL system. Similarly, the Ayeni model resulted in reasonable predictions for the horizontal velocity and granular temperature, but not for the vertical velocity and pressure drop in the NETL BFB system.

The experimental data and simulation predictions were compared in parity plots in Figure 3.9. The diagonal line represents equality between the experimental values and the simulation results. The simulation results with the different drag models underestimated the average particle height (Figure 3.9 (a)), but overestimated the pressure drop and granular temperature (Figure 3.9 (b)). The discrepancies in the particle velocity (Figure 3.9 (a)) were rather scattered, with data points located both above and below the diagonal line. Consequently, the discrepancy percentage for each model with the experimental data was calculated. For a given drag model, the resulting discrepancy percentages for different parameters were summed, and this value was defined as the overall discrepancy. The minimum overall discrepancy was found for the Ayeni model, followed in increasing order by the Di Felice, Syamlal–O'Brien, EMMS, BVK, and Gidaspow models.

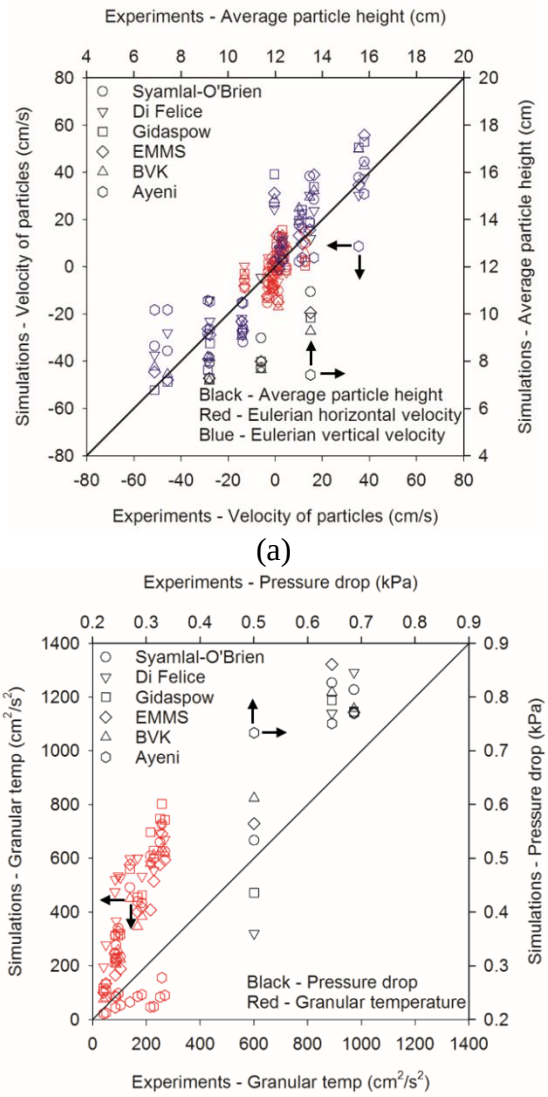

Figure 3.9 Comparison between experimental data and simulation results (a) Eulerian vertical and horizontal velocities and average particle height, and (b) granular temperature and pressure drop

Figure 3.10 shows a comparison between the simulation results for the NETL bed in this study and those reported by Ayeni et al. [44], Eleghannay and Tafti [87], Koralkar and Bose [49] and Lungu et al. [50]. Lungu et al. [50] performed an EE simulation while the other three studies performed EL simulations. Koralkar and Bose [49] used MFiX–DEM code, and Eleghannay and Tafti [87] used their GenIDLEST in-house code. The comparison shows significant variations in the predictions. This may be a result of differences in the modeling approaches and/or differences in implementation of the CFD–DEM model in the different codes.

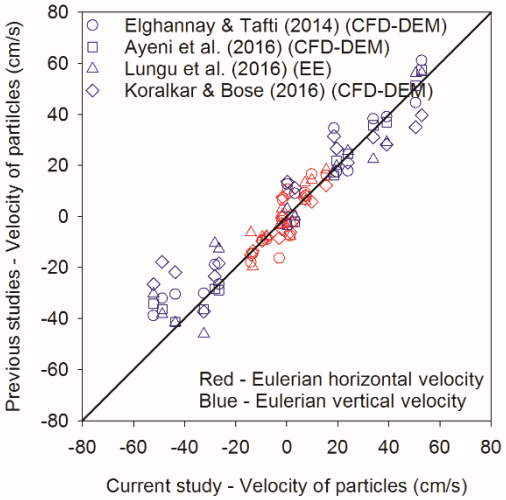

Figure 3.10 Comparison between predictions of the current study and previous studies using the Gidaspow model

3.6. **Conclusion**

The effect of drag models on CFD–DEM predictions was analyzed for the BFB systems described in Goldschmidt et al. and the NETL challenge problem. For the BFB system investigated by Goldschmidt et al., the Di Felice model resulted in reasonable predictions of the average particle height, with less than 16% discrepancy between the predictions and experimental data. The other drag model results predicted low particle heights, with discrepancies in the range of 11–45%. The simulations with models other than the Di Felice and Syamlal–O'Brien did not predict the formation of bubbles at an inlet velocity of $1.25\boldsymbol{U}_{mf}$. For the BFB system in the NETL challenge problem, all drag models showed reasonable qualitative agreement with the experimental data. However, no single model resulted in close quantitative predictions. The Ayeni model resulted in reasonable predictions for the horizontal velocity and granular temperature of particles, but failed to predict the variation in pressure drop with fluidization velocity. Analysis of the overall discrepancy suggests that the Ayeni and Di Felice models resulted in minimum discrepancies, while the conventional Gidaspow model resulted in the maximum discrepancy

4 Effect of initial bed configuration in bi–dispersed BFB

4.1. Introduction

The previous chapter focuses on simulations of mono-dispersed BFBs, while this chapter focuses on simulations of bi-dispersed BFB. Bi-dispersed BFB with sand and biomass were considered to study the pyrolysis process, in line with the other research work on pyrolysis occurring in our group. This study investigates the effect of four different types of initial bed conditions (case–1: homogeneous mixture of sand and biomass, case–2: biomass at top and sand at bottom, case–3: biomass at bottom and sand at top, case–4: biomass at left and sand at right) on the extent and time required to achieve the steady-state mixing.

Bi-dispersed fluidized beds, where a bed consists of two different types of solids, are important to several processes. The performance of this type of fluidized beds largely depends on the extent of mixing or segregation of solids. For example in fast pyrolysis, biomass is fluidized with sand as a heat transfer medium, and the heat transfer between the sand and biomass governs the extent of pyrolysis and type of products [1]. In a titanium refining industry, mixing of chlorine gas and rutile and coke solid particles critically defines the yield and reaction rate of the system [31].

Typically, the extent of mixing between two solids in a bi-dispersed bed depends on inlet velocity of the gas, the configuration of solids bed and properties of phases. The effect of these parameters has been extensively studied both experimentally and computationally [24–27,29,123,159,160]. The key finding is that significant segregation is observed at a low fluidization velocity, whereas a high degree of mixing is observed at high fluidization velocities [25]. When we change the ratio of densities

or amount of two solids, significant variation in mixing/segregation was observed [24,25]. To understand the mixing phenomenon, it is critical to analyze the transient behavior of the bed. Rowe and Nienow [30] provided visual observations during fluidization of an initially segregated bed, where one type of solids was kept on the other. They observed the role of bubbles and the formation of the wake behind each bubble in the mixing of solids. Marzocchella et al. [112] investigated transient fluidization of a bi-dispersed bed. They found that the effect of fluidization velocity on the segregation of particles was sharp and directly correlated to initial bed composition. Bokkers et al. [23] conducted visual experiments and DPM simulations to study the extent of segregation induced by injecting a single bubble in a bi–dispersed fluidized bed. They observed a strong influence of the drag in the initial segregation and the behavior of the bubble in the bed. Feng and Yu [161] also conducted DPM simulations to investigate the role of drag and contact forces on the mixing/segregation behavior of a bi-dispersed bed. Their analysis provided critical values of drag forces on either jetsam or flotsam that can suppress or promote the segregation in the bed. Gorji-Kandi et al. [162] experimentally characterized the solid mixing rate in a bi-dispersed BFB. They proposed an empirical correlation to estimate the mixing rate constant as a function of dimensionless numbers (Archimedes, Reynolds, and Froude) under different operating conditions. Rhodes et al. [163] studied the mixing behavior in an initially segregated bed where solids were initially placed side-by-side. Recently, Sánchez-Prieto et al. [164] investigated radially segregated bed and characterized the time required for mixing. They investigated the axial and lateral diffusivity of solids to explain the mixing/segregation in the bed. It is clear from the previous studies that one of the critical parameters is the initial bed conditions which directly influences the

gas-solid hydrodynamics in the early stage of fluidization, and governs the rate of mixing.

The present study investigated the effect of different initial bed configurations on the rate of mixing of sand and biomass solids by assuming different initial positions of flotsam and jetsam in a bed. The investigation was conducted by conducting transient CFD–DEM simulations using different initial bed conditions. CFD–DEM methodology implemented in the MFiX–DEM code [94–96] was used and the solids were considered as the discrete particles. Initially, the model was validated by comparing the simulation predictions with the experimental data of Bai et al. [25]. The simulation results from different drag models were analyzed for appropriate selection of drag model. Consequently, further simulations were performed for four different initial bed conditions. The predictions of particle segregation number (PSN), the time required to achieve steady-state bed condition, the evolution of bubbles and their effect on mixing were analyzed.

4.2. Simulation setup

Simulations were conducted for a 2D geometry (Figure 4.1 (a)) having dimensions of the experimental setup of Bai et al. [25]. The bottom of the geometry was configured as velocity inlet for air, and the top was configured as pressure outlet with zero gauge pressure. An equal volume of sand and biomass was used to make a solid bed. The positions of sand and biomass were varied as shown in Figure 4.1 (b) to configure four different initial bed conditions. The sidewalls were defined by no-slip boundary condition for the gas phase. For the solid phase, particle–wall restitution coefficient was defined. Transient simulations were carried out using a fluid time step of 0.0001s, while a solid time step was implicitly calculated by the model using the normal and

tangential component of spring and restitution coefficients. Second-order spatial discretization was used for the gas phase. First-order and second-order temporal discretizations were used for the gases and solids, respectively. The contact force was calculated using the values of friction and restitution coefficients, and spring constant. Bai et al. [25] provided the values of the restitution coefficient, whereas the value of 800 N/m as spring constant and 0.1 as friction coefficient were selected by following previous studies [81,96].

Transient simulations were conducted using four initial bed configurations as shown in Figure 4.1 (b). The simulations were performed for a total of 15 s flow time. The average particle height, mixing index and gas-solid drag model was analyzed for all the simulated cases.

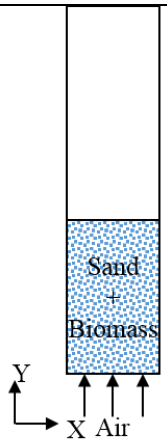

Dimensions (L × H) (cm^2)	10.2 × 81.6	
Grid size (x × y) (cm^2)	0.56 × 0.55	
Materials	Biomass	Sand
d_p (μm)	900, 550	550
ρ_p (g/cm^3)	1.3	2.6
$\boldsymbol{U}_{mf}$ (cm/s)	26.01	21.3
N_p ($d_{p,Biomass} = 900\mu m$)	7373	32250
N_p ($d_{p,Biomass} = 550\mu m$)	20700	20700
Initial ratio of volume fraction	0.5:0.5	
$\boldsymbol{U}_G$	1, 2 and 3 $\boldsymbol{U}_{mf}$ of sand	
Coefficient of restitution	0.97	

(a)

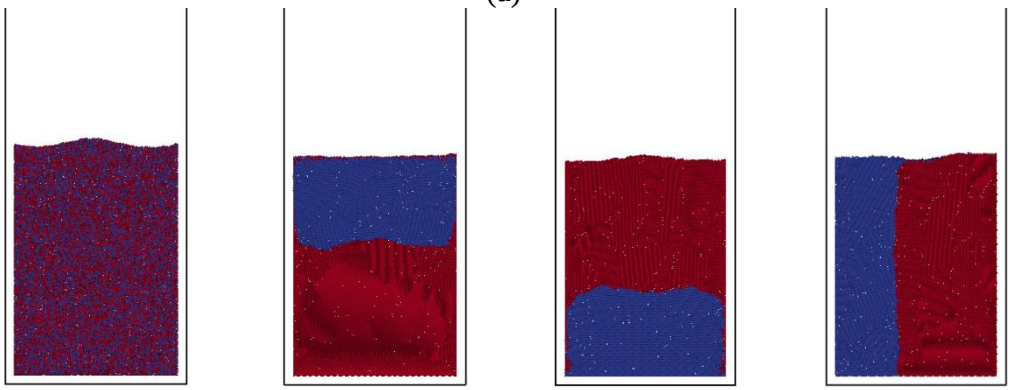

(b)

Figure 4.1 (a) Schematic diagram of simulated fluidized bed (Bai et al. [25]*); (b) initial bed configuration (case–1: homogeneous mixture of sand and biomass, case–2: biomass at top and sand at bottom, case–3: biomass at bottom and sand at top, case–4: biomass at left and sand at right)*

4.3. Characterization of mixing between two solids

4.3.1. Particle Segregation Number

Bai et al. [25] measured the extent of mixing as a particle segregation number (PSN) with 0 % representing a completely mixed condition and 100 % implying the completely segregated bed. The PSN is defined as the difference in average height of the two solid phases and is calculated as follows:

$$PSN = 2\left(\Delta h_{flotsam} - \Delta h_{jetsam}\right) \times 100\ \% \quad (1)$$

where the subscripts "flotsam" refers to the particles that tend to accumulate on the top and "jetsam" refers to the particles that tend to sink at the bottom of the bed. Δh is the dimensionless average height of solid phase s, which is calculated as:

$$\Delta h = \frac{\sum_k^N \epsilon_s^k h^k V^k}{H_0 \sum_k^N \epsilon_s^k V^k} \quad (2)$$

where ϵ_s^k is the volume fraction of solid phase s in the k$^{\text{th}}$ cell, h^k and V^k are the height and volume of k$^{\text{th}}$ cell and H_0 is the initial bed height. Eq 2 results in the average height of both the solid phases when they are in the fluidization condition, whereas the PSNs calculated in Bai et al. were reported for the collapsed bed. Thus, a correction factor to account for the collapsed bed condition was also proposed by Bai et al. [25]

$$h'^k = \frac{\mathrm{V}_G^k(0)}{\mathrm{V}_G^k(t)} \quad (3)$$

where, h'^k is the correction factor and $\mathrm{V}_G^k(0)$ and $\mathrm{V}_G^k(t)$ are the gas volume fraction in the k$^{\text{th}}$ cell at the start and at any time during the fluidization process respectively. The average particle height in the collapsed bed condition can be calculated as:

$$\Delta h = \frac{\sum_k^N \epsilon_s^k h^k h'^k V^k}{H_0 \sum_k^N \epsilon_s^k V^k} \quad (4)$$

The PSNs calculated by eq (4) were used to compare the simulation results with the experimental data.

4.3.2. Solids diffusivity

Mixing can be also be determined by measuring the diffusivity of solid particles inside the fluidized bed [66]. Solids diffusivity is typically determined by assuming the Fickian equation of diffusion [29].

$$\frac{\partial C}{\partial t} = D\nabla^2 C \quad (5)$$

Where, D is defined as the dispersion coefficient analogous to the diffusion coefficient. However, in the dispersion coefficient, the effect of convection and diffusion are lumped into a single parameter [29]. Dispersion coefficient can be determined by first measuring the concentration of flotsam at different locations and time and then using that concentration profile to calculate the dispersion coefficient from Eq 5 [164].

However, in the present study, another method given by Mostoufi and Chaouki [165] and Norouzi et al. [85] was used to calculate the dispersion coefficient. According to Norouzi et al. [85], the instantaneous excess axial displacement (Y) of a single flotsam particle can be calculated by

$$Y = h(t) - h(0) \tag{6}$$

where $h(t)$ is the instantaneous axial location of particle and $h(0)$ is the location at time t=0. The average excess axial displacement ($\bar{Y}$) at any time 't' will be

$$\bar{Y} = \frac{1}{N_{p,flotsam}} \sum_{1}^{N_{p,flotsam}} Y \tag{7}$$

where, $N_{p,flotsam}$ is the total number of particles in the flotsam phase. The mean square displacement (MSD) of the flotsam phase and subsequently dispersion coefficient in the axial direction (D_y) can be calculated as

$$MSD_Y = \frac{1}{N_{p,flotsam}} \sum_{1}^{N_{p,flotsam}} (Y - \bar{Y})^2 \tag{8}$$

$$D_y = \frac{1}{2} \frac{d(MSD_Y)}{dt} \tag{9}$$

The slope of the plot between MSD and time 't' will give the dispersion coefficient. Dispersion coefficient in the radial direction can be calculated using the similar approach.

4.4. **Results and Discussion**

4.4.1. Particle segregation number

Figure 4.2 compares the steady-state PSNs calculated from the simulation results and experimental data of Bai et al. [25]. A reasonable quantitative agreement can be seen in Figure 4.2 (a), which compares the predictions for 900 µm biomass and 550 µm sand at $3\boldsymbol{U}_{mf,Sand}$. Figure 4.2 (b) compares the PSNs for 550 µm biomass and 550 µm sand and shows a discrepancy between the experiments and predictions. The simulations resulted in a uniformly mixed bed with PSN varying from 0 to 20%, while the experiments resulted in a partially mixed state with PSN varying between 20 to 40%. It should be noted that the EE simulations of Bai et al. [25] also predicted similar discrepancy for the experimental condition of Figure 4.2 (b). This discrepancy can be attributed to the selection of the drag model. Several previous studies [46,48,49,51,137,141] have discussed the effect of drag models on simulation. For mono-dispersed fluidized beds, Chapter 3 showed that none of the available drag models could predict different sets of the experimental data. The present study also showed that the model resulted in good comparison at one set of operating conditions but resulted in wide discrepancy for the other set of operating condition. To improve the model validation, four different drag models, proposed by Gidaspow [42], Syamlal–O'Brien [41], Di Felice [129] and Beetstra–van der Hoef–Kuiper (BVK) [43], were simulated. The PSNs predicted by different drag models were compared with the experimental data (Figure 4.2 (c)). The Syamlal–O'Brien model consistently resulted in predictions closer to the experimental data. Consequently, the present study used the Syamlal–O'Brien drag model for all subsequent simulations. Further investigation was carried out by using three grid sizes. Figure 4.2 (d) shows that all the three grid sizes predicted values comparable to each other and therefore, the largest

grid of size 0.56 (x) × 0.55 (y) × 0.09 (z) cm^3 was selected for the subsequent simulations.

Figure 4.2 (f) shows the comparison of the predicted PSNs for biomass of size 550 μm at all three superficial velocities and that calculated using the empirical correlations of Nienow et al. [166] and Rice and Brainovich [167]. Nienow et al. [166] proposed a correlation relating the steady state mixing index with superficial gas velocity and densities of solids. Both correlations critically depend on the take–over velocity, which can be defined as the gas velocity at which the mixing index is 50%. It is to note that the calculation of the mixing index used in the correlations and present study is different. In the correlation, the mixing index was defined based on the ratio of the mass fraction of jetsam in the upper uniform part of the bed with that of an overall mass fraction of jetsam. In simulations, the mixing index was defined based on PSN. Consequently, take–over velocity was determined by performing the CFD–DEM simulations with increasing gas velocity and bed initially at a segregated state as shown in Figure 4.2 (c). The predictions were consistently closer to the correlation of Nienow et al. [166] for fluidization velocities of 1 and $2\boldsymbol{U}_{mf,Sand}$. However, at $3\boldsymbol{U}_{mf,Sand}$, the simulations slightly over predicted the PSN compared to that from the correlations. The comparison between the simulation results, experimental data and the values calculated from the available empirical correlation validated the model used in the study. The model was then used to investigate the transient phenomena of bubble formation and mixing inside the bed.

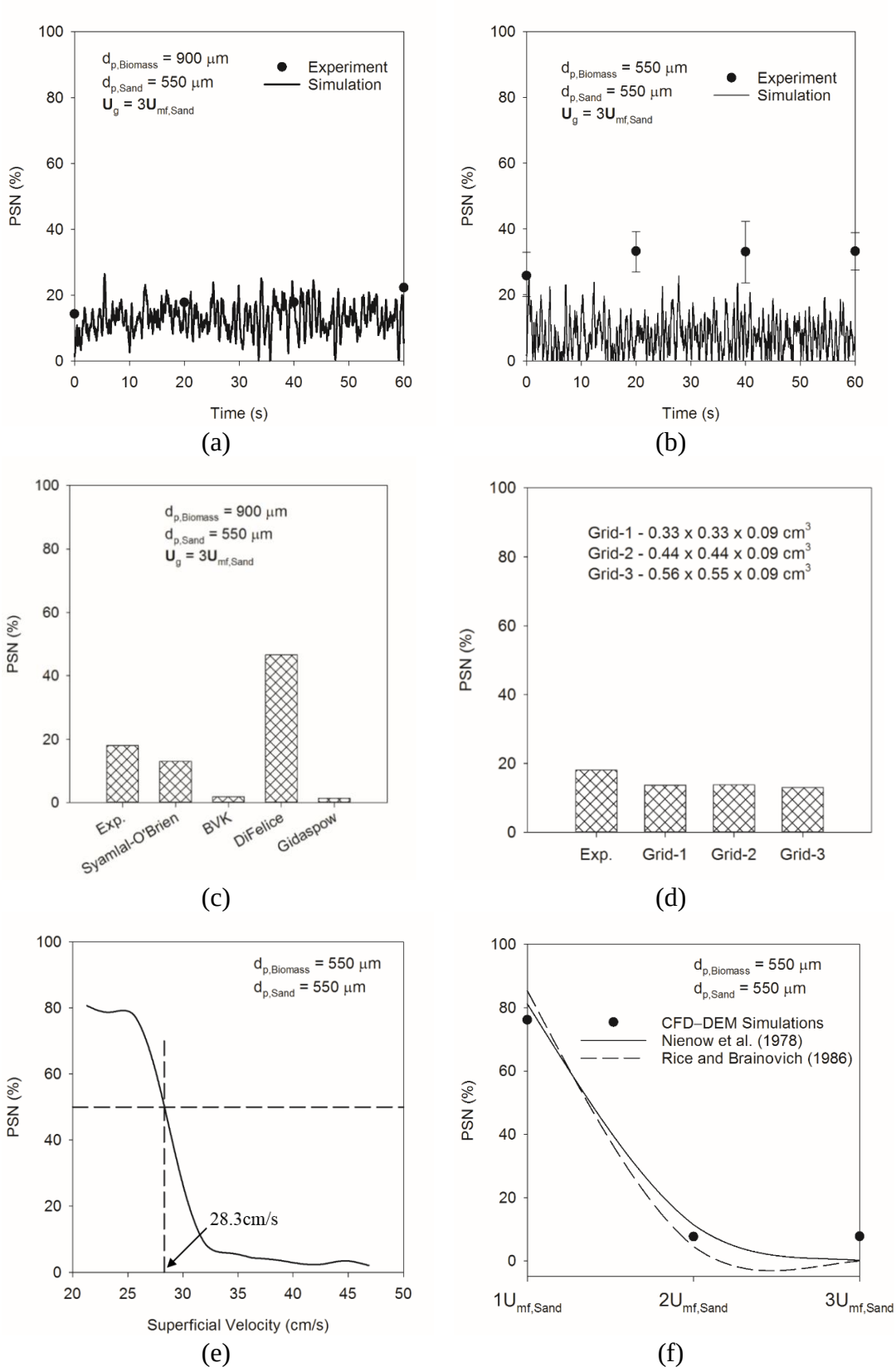

Figure 4.2 Comparison of PSN from experiments and simulation results, (a) and (b) Comparison of predicted PSN with experiments for biomass of 900 and 550 μm respectively, (c) effect of drag models, and (d) effect of grid size, (e) Calculation of take–over velocity and (f) comparison of simulation results with empirical correlation

4.4.2. Bubble evolution and mixing

To analyze the role of the formation, propagation and eruption of bubbles on the mixing of bi–dispersed solids, the instantaneous positions of sand and biomass particles ($d_{p,Biomass}$ = 900 µm and $d_{p,Sand}$ = 550 µm, $\boldsymbol{U}_G$ = 3$\boldsymbol{U}_{mf,Sand}$) were visualized in Figure 4.3. Figure 4.3 (b) depicts the formation of the first bubble, which starts at the interface between sand and biomass. The formation of the bubble at the interface and not at the bottom of the bed can be attributed to the difference between densities of the two solids [30]. As the bubble in the biomass phase propagated and grew in size, the subsequent bubble started developing in the sand phase (Figure 4.3 (c)). Sand and biomass particles at the bottom of their respective bubbles experienced an upward force from the wake and therefore, the particles lifted at a velocity similar to the velocity of bubbles [3,5]. Contrary, the particles above the roof of the bubble experienced an upward push. This force was not evenly distributed to all the particles due to the oval shape of the bubble. The particles at the centre experienced more push compared to the particles at the boundary, resulting in a dome-like structure. The particles at the periphery of the bubble moved downwards to balance the space created by the bubble movement. This type of motion induced by the bubble propagation was analogous to the reciprocating motion of the piston. The eruption of a bubble formed in the biomass phase in Figure 4.3 (d) ejected the particle in radially outward direction. Interestingly, Figure 4.3 (d) showed that the epicentre of particle ejection was not located at the top of the bubble but instead, it was inside the bubble. A similar analysis was reported by the Muller et al. [4], who performed PIV experiments in a 2D gas fluidized bed and showed that point of the epicentre was located at ~$d_b/5 - d_b/4$ distance from the top surface. The ejected particles collided with the wall and consequently lose their momentum, which resulted in sliding of biomass particles

towards the bottom of the bed. The propagation of bubble causing the formation of dome-like structure in the sand phase and formation of another bubble in the biomass phase and consequent pulling of particles by its wake caused the elongation of a bubble in the sand phase as seen in Figure 4.3 (e) and (f). This elongation resulted in shrinking of the area occupied by the sand at the interface, allowing further sliding of biomass particles towards the bottom of the bed. The elongation of the bubble in the sand phase was further enhanced by the formation of two small bubbles in the biomass phase as seen in Figure 4.3 (f). Sand particles at the top of the bubble were pulled by the wakes of two smaller bubbles in the biomass phase. The eruption of bubble initially formed in the sand phase is shown in Figure 4.3 (g), where the ejection of the particles was similar to that shown in Figure 4.3 (d). The roof of this bubble, however, had sand as well as biomass particles, forcing all the particles to move radially outwards and subsequently downward towards the bed. The bottom of the bed was expanded by the formation of another bubble in Figure 4.3 (g). This formation of a bubble at the bottom and its propagation and eruption at the top induced axial movement of particles. This phenomenon resulted in the mixing of particles. However, the lateral mixing, which enhances the rate of mixing, was induced by the formation and coalesce of bubbles inside the bed (Figure 4.3 (h) and (i)).

Further simulations with different segregated states were performed to study the effect of initial bed configuration. Figure 4.4 (a) and (d) shows the two segregated beds where sand was maintained at the top of the biomass (Case–3), and both sand and biomass were radially segregated (Case–4). In Case–3, a slug was formed (Figure 4.4 (b)), and it resulted in the inversion of biomass phase. Sand particles were pushed towards the bottom, and biomass particle floated on top of it (Figure 4.4 (c)). Similarly, in the case with radially segregated biomass and sand, the first bubble formed in the biomass

phase and it carried all the biomass particles with it (Figure 4.4 (e)). The sand particles, on the other hand, balanced the space created by the bubble which eventually resulted in the biomass phase positioned at the top of the sand phase (Figure 4.4 (f)). After the sand, and biomass phases had repositioned themselves, the behavior of the bed, as explained in the Case–2 system (Figure 4.3), was observed.

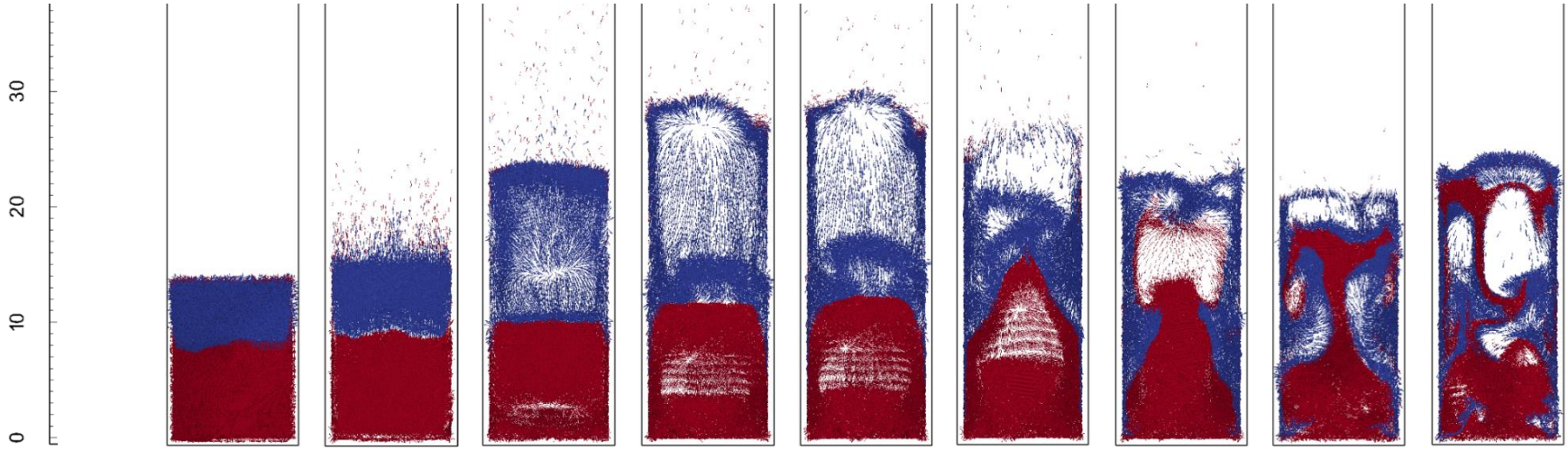

Figure 4.3 Effect of bubble evolution on mixing (case –2)

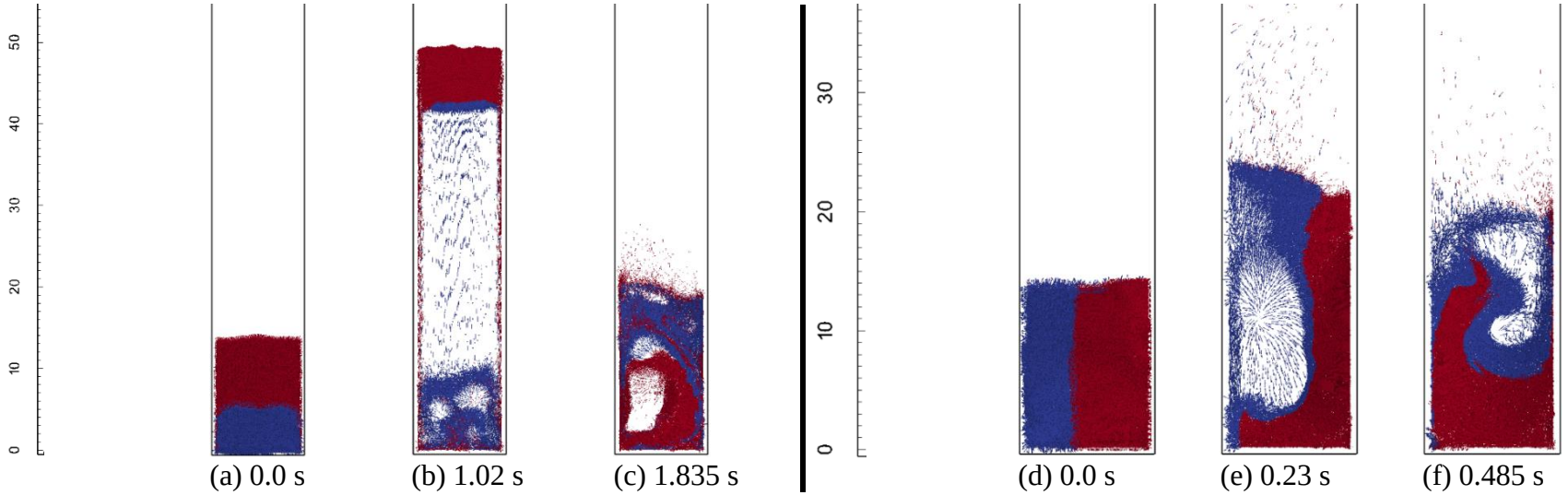

Figure 4.4 Bubble evolution for different initial bed configuration (case –3 and case –4)

4.4.3. Mixing time

Average particle height, defined by Goldschmidt et al. [13] was calculated for both the sand and biomass phase ($d_{p,Biomass}$ = 900 µm and $d_{p,Sand}$ = 550 µm, $\boldsymbol{U}_G = 3\boldsymbol{U}_{mf,Sand}$) to determine the mixing time, defined as the time required to achieve the steady state mixing. Three segregated state defined in the previous section and the uniformly mixed state were considered in this section to quantify the mixing time and also to determine if different initial configuration had any effect on the steady-state mixing. When the average particle height of both the phase coincide, then the system has attained the steady state mixing. Figure 4.5 depicts the steady state mixing realized for all four initial bed configurations, which was not affected by any initial bed configuration considered. However, there was a significant variation in the mixing time. Similar observation, where different initial bed configuration affects the mixing/ segregation time but not the extent of mixing was also made by the Zhang et al. [160]. In a Case where the bed was initially well mixed, the bed remains at that state even after fluidization. Consequently, mixing time is negligible for this case. Whereas, for the three segregated cases defined in Figure 4.1 (b), mixing time of approximately 2 s, 3 s and 3 s was calculated for Case–2, 3 and 4 respectively (Figure 4.5).The extra mixing time required by the Case–3 and 4 can be attributed to the time required for biomass phase to position itself on top of the sand phase, as discussed in the preceding section. The difference in mixing time can have implication in the efficiency of the process, where, the residence time of solids is very small. For example in a continuously fed system where, the residence time of solids is less than the mixing time then even though the solids can attain the desired extent of mixing, but the solid phases will not get the enough time to attain the steady state.

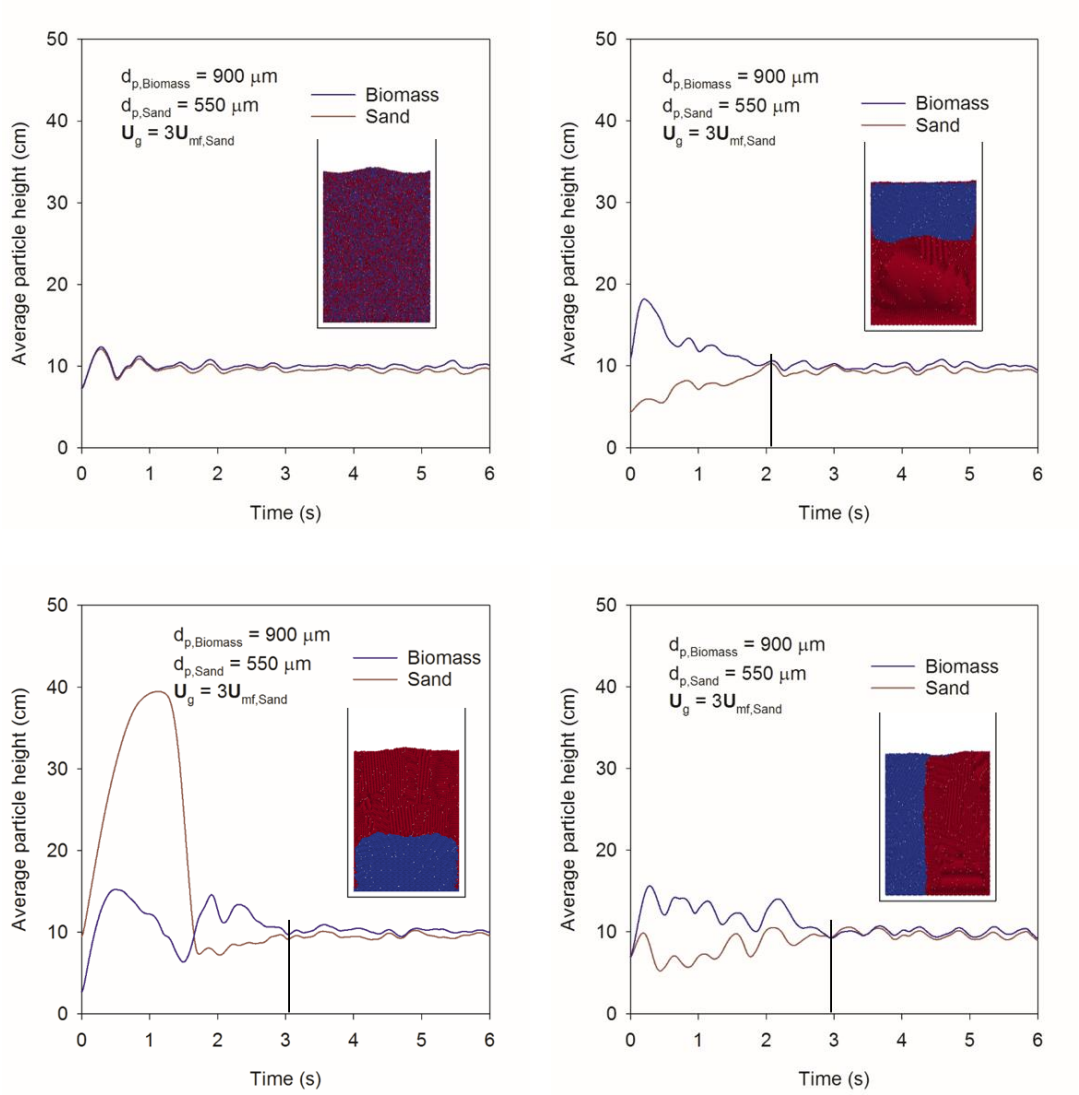

Figure 4.5 Mixing time calculated for different initial bed configuration

A correlation to calculate the mixing time was formulated by Sánchez-Prieto et al. [164] by calculating the time required by glass beads to achieve the steady state mixing. To determine the mixing index, Sánchez-Prieto et al. [164] used high speed imaging and differently colored glass beads arranged in an initial configuration depicted by Case–4. According to their correlation, the system considered in this study will require 0.3 s to reach the steady state mixing compared to 3 s determined in Figure 4.5 for Case–4. The difference in mixing time calculated from correlation and that determined in this study can be attributed to the mono–dispersed bed of glass bead,

considered by Sánchez-Prieto et al. [164] whereas; present study considered bi–dispersed fluidized bed consisting of sand and biomass.

4.4.4. Solids diffusivity

Dispersion coefficient analogous to diffusion coefficient defines how fast flotsam particles diffuse/mix with jetsam particles. Figure 4.6 (c) shows the dispersion coefficient in axial and radial directions calculated from Figure 4.6 (a) and (b) respectively using the method discussed in Section 4.3.2. In Figure 4.6 (a) and (b), the bed was initially segregated, and biomass was placed on top of the sand (Case–2). Dispersion coefficient was also calculated for other segregated initial bed configuration shown in Figure 4.1 (b) (Case–3 and 4). It could be seen from Figure 4.6 (c) that dispersion coefficient calculated in the lateral direction was much smaller than that obtained in the axial direction, consistent with the observation of Shen et al. [123] and Norouzi et al. [85]. Thus, the mixing process was non–uniform in the axial direction. This could be attributed to the solids motion induced by the bubble as discussed in Section 4.4.2. The lateral mixing, on the other hand, is caused by small bubbles either coalescing or breaking from the large bubbles.

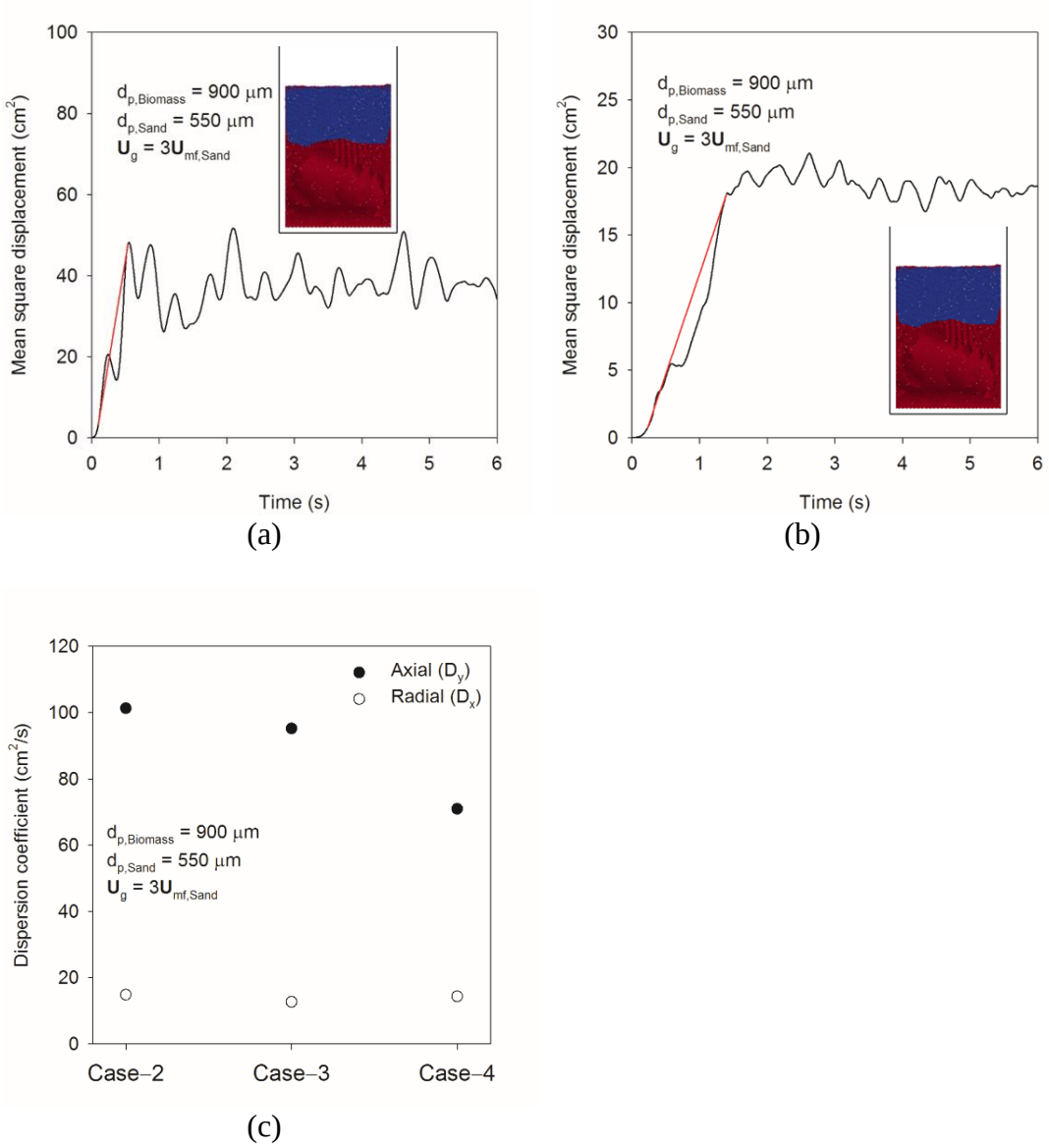

Figure 4.6 Calculation of solids diffusivity in (a) axial direction, (b) radial direction and (c) Dispersion coefficient for different initial bed configuration

4.5. **Conclusion**

Literature review on bi-dispersed BFB in Chapter 2 revealed that initial bed conditions directly influences the gas-solid hydrodynamics in the early stage of fluidization, and subsequently governs the rate of mixing. CFD–DEM simulations were, therefore, carried out to determine the extent and rate of mixing in the BFB that consisted of sand ($d_{p,Sand}$ = 550 μm) and biomass ($d_{p,Biomass}$ = 900 and 550 μm). The simulation predictions were validated with the experimental data of Bai et al. [25]. The effect of initial bed configurations (case–1, 2, 3, 4) on the mixing of two solids was then investigated. The evolution of bubbles owing to three segregated configurations was also studied. It was found that the Syamlal–O'Brien drag model predicted the PSN reasonably well for biomass of 900 μm mixed with sand of 550 μm but underpredicted the PSN for $d_{p,Biomass}$ = 550 μm and $d_{p,Sand}$ = 550 μm system. Similar steady state mixing was achieved for all fours cases, however, the time required to achieve that steady state varied significantly among the four cases with case–1 having the least mixing time followed by the case–2. The variation in the mixing time can be critical in a continuously fed reactive fluidized bed where reaction time is smaller than the mixing time, as solid phase tend to react before getting completely mixed. Improper mixing of solids causing poor heat and transfer at the time of reaction results in a decrease of efficiency of such fluidized bed. Moreover, mixing was found to be non–uniform in axial direction and governed by the bubble formation, propagation and eruption. Mixing in lateral direction was found to be governed by the coalescence of bubbles.

5 ECVT measurement of bubble properties

"Reproduced from V. Agrawal, Y.H. Shinde, M.T. Shah, R.P. Utikar, V.K. Pareek, J.B. Joshi, Estimation of Bubble Properties in Bubbling Fluidized Bed Using ECVT Measurements, Ind. Eng. Chem. Res. 57 (2018) 8319–8333. Copyright [2018] American Chemical Society"

5.1. Introduction

It is clear from the preceding chapters that the gas-solid hydrodynamics in a BFB depends on the formation, growth, and eruption of bubbles. It is vital to measure the bubble properties and their variation in the bed. Many experimental studies have, therefore, been conducted to determine the bubble properties (reviewed in Chapter 2). It was found that, most of the experiments were conducted using the intrusive techniques, where, probe affects the local hydrodynamics of BFB. Non-intrusive techniques, on the other hand, have either low temporal or spatial resolution. Also operational feasibility is a challenge in few non-intrusive techniques such as radioactive particle tracking (RPT), and positron emission particle tracking (PEPT). This chapter presents a systematic investigation of measurement of bubble properties such as size, velocity and frequency using ECVT.

BFB experiments have been conducted using different invasive and non-invasive measurement techniques. The non-invasive techniques are more desirable as they neither interfere with flow nor require transparent equipment. Typically, non-invasive techniques such as X-ray tomography, γ-ray tomography, electrical capacitance tomography (ECT), magnetic resonance imaging (MRI), RPT, and PEPT are used. Each of these techniques has advantages and disadvantages in terms of operational feasibility and resolution of data [69]. ECT has advantages such as fast imaging speed

and low operational hazards [69]. Consequently, ECT (data obtained for a single 2D plane) and ECVT (data acquired for a 3D volume) were used in several BFB studies as summarized in Table 1 [55,63,168–171].

Despite its extensive use, capacitance tomography also has several limitations including variation in capacitance at one location causing the signal reconstruction to be sensitive to errors and noise [69]. Further, the resolution of the reconstructed images is significantly influenced by the number of electrodes and applied image reconstruction algorithm [170,172]. Several algorithms such as linear back propagation (LBP) [173], Landweber iterative (LI) [174], Tikhonov regularization principle (TRP) [175,176], algebraic reconstruction technique (ART) [177], simultaneous iterative reconstruction technique (SIRT) [178], neural network multi-criteria optimization image reconstruction technique (NN-MOIRT) [179,180], combination of the TRP and ART [181], modified LI [182,183], total variation iterative soft thresholding (TV-IST) [171,184] and others have been proposed in the literature. Of these algorithms, LBP, NN-MOIRT, and TV-IST were used in previous BFB studies (Table 5.1). Cui et al. [185] highlighted that the performance of the algorithms varied significantly with imaging tasks and hence, the selection of an algorithm must be task-specific.

LBP algorithm is the simplest and fastest [63], and hence, it has been most commonly used in the previous studies (Table 5.1). However, it results in relatively low-resolution images that demonstrate a surface enclosing bubbles with a gradual transition of volume fraction [186,187]. Owing to the blurring of the boundaries, the estimation of the bubble size critically relies on a cut-off value of solids volume fraction (also referred as a threshold) that distinguishes a bubble from the dense phase. Halow and Nicoletti [186] discussed the limitation concerning the selection of the threshold value.

The previous studies used a threshold value between 0.3 and 0.35 to post-process their captured data. For example, Hulme and Kantzas [52] used a threshold of 0.3, whereas Asegehegn et al. [54] used a threshold of 0.33 to calculate the bubble diameter in a 2D fluidized bed. Holland et al. [53] determined that measurements from ECVT and MRI were consistent with each other at a threshold of 0.315. Weber and Mei [55] also used 0.315 to calculate the bubble diameter; however, they also highlighted the unavailability of a method to determine the threshold. White [188,189] performed experiments by maintaining a hollow sphere inside a static bed and repeated these experiments using spheres of different size. He also used the LBP algorithm and constructed contours of solids volume fraction at three thresholds (0.2, 0.5, and 0.8). He could not estimate the size of a 6.5 cm diameter sphere with any of these values. He attributed this deficiency to the poor spatial resolution of the ECT images and concluded that a variable threshold must be used to estimate the size of different spheres.

The present study proposes an iterative method to determine an optimum threshold value for post-processing of each 2D image obtained by ECVT. For this, static fluidized bed experiments with a known size beaker maintained at different positions of the bed are conducted. These experiments are repeated for different sizes of beakers, and the captured ECVT data are used to develop an iterative method to calculate an optimum threshold value. Then, experiments with three fluidization velocities are conducted, and the captured data are post-processed using the LBP algorithm with the developed method for optimum thresholds to estimate bubble sizes. Further, rise velocities, frequency, and evolution of bubbles at varying fluidization velocity are also estimated and analyzed.

Table 5.1 Previous BFB studies using either ECT or ECVT

	Sensor details			Experiment details					Estimated properties	Contribution
	Dia. (cm)	Freq. (Hz)	Algorithm	Particle Dia. (μm)	Solid density (gm/cm^3)	Geldart classification	U_{mf} (cm/s)	Gas velocity (U/U_{mf})		
Halow et al. [187]	15.24	62.5	-	704, 300, 4475, 3075, 3175	1.14	B and D	19.0, 8.0, 82.2, 80.1, 84.1	1-4	(b), (c)	Empirical correlations of bubble size and velocity
Yang and Liu [190]			LBP	--	--		--	--	(e)	Fluidization regimes were identified and a method to calculate the velocity of solids was proposed.
Makkawi and Wright [63]	13.8	100	LBP	530	2.6	B	37	0.54-6.4	(e)	Fluidization regimes were identified based on the calculated transition velocity.
Makkawi and Wright [191]	13.8	20-100	LBP	530	2.6	B	27	3.33	(a), (c), (d)	The effect of measurement frequency was investigated. The authors recommended at least 4000 data points to achieve statistically invariant estimations of bubble velocity and frequency.
White [188]	20		LBP	113, 153	3.333, 4.645	A, B			(b)	Need of a variable threshold to capture various sphere diameters was emphasized.
McKeen and Pugsley [168]	14	100	LBP	79	1.4	A		U = 5, 10, 15 and 20	(b), (c)	Data from ECT experiments were compared with CFD simulation results.
Makkawi and Wright [192]	13.8	100	LBP	90, 350, 530, 1850	2.5	B/A, B and D	-	$(U-U_b)$~0.2 to 0.6	(c), (d)	The effect of measurement span was studied and minimum 60 s measurement was recommended to get reproducible results.
Du et al. [169]	5,10, 30	100	NNMOIRT	60	1.4	A	-		(a), (b)	Data from ECVT were compared with those from an optical probe. Flow behavior in void phase and emulsion phase was characterized based on the two-region model.
Holland et al. [53]	5	80	NNMOIRT	58	0.6	A	0.014	2.8-7.0	(a)	Images of solids volume fraction distribution obtained from ECVT were compared with those from MRI.
Chandrasekera et al. [79]	5	80	NNMOIRT	1200	0.96	D	30	<1	(a)	MRI and ECVT data on the size of a jet were compared with each other.
Rautenbach et al. [170]	10.4	100	LBP	Combination of sizes from 100 - 1000	2.6	B and D	-	-		The statistical method was used to analyze the uniformity of fluidizing gas distribution.
Rautenbach et al. [80]	10.4	100	LBP	265.85, 800.35	2.485	B and D	4, 27	-	(b), (d)	Estimations of bubble diameter and frequency obtained by ECT and X-ray tomography were compared.
Weber and Mei [55]	10	52	NNMOIRT	185	2.483	B	3.17	1,2,4 and 6	(a), (b), (d)	Estimated bubble properties were analyzed.
Chandrasekera et al. [171]	5		TV-IST	300	1	A	5	1.16 – 2.4	(b), (d)	Bubble diameters calculated using TV-IST were compared with those calculated using Darton's empirical correlation.
Ye et al. [193]	-	-	LBP, LI	-	-		-	-	-	The effect of a number of electrodes on capacitance data and reconstructed image in multi-plane ECT was investigated.
Guo et al. [172]	6.0	100	TRP	65	1.37	A	0.275	4.25 – 46.5	(a), (b)	Modification of conventional TRP algorithm was proposed.

Abbreviations::
(a) LBP = Linear Back Propagation
(b) NNMOIRT = Neural Network Multi-criteria Optimization Image Reconstruction
(c) LI = Landweber Iterative
(d) TV-IST = Total Variation Iterative Soft Thresholding
(e) TRP = Tikhonov Regularization Principle

Estimated properties:
(a) Solids volume fraction distribution
(b) Bubble size
(c) Bubble velocity
(d) Bubble frequency
(e) Transition in flow regime

5.2. **Experiments**

5.2.1. Setup

Figure 5.1 displays a schematic of the experimental setup consisting of a cylindrical fluidized bed, 20 cm diameter (d_{bed}) and 120 cm height (H). The fluidized bed column was attached to a 15 cm long plenum chamber, which was filled with 2 cm glass marbles for uniform gas distribution. Between the column and plenum chamber, a perforated distributor with 302 uniformly spaced holes of 1 mm was placed. Further, a nylon mesh of 250 µm was placed on top of the distributor to prevent the solids from sinking. Sand was used as the solid, which had a mean diameter of 320 µm with a size distribution of 100–600 µm measured by a Malvern Mastersizer (Figure 5.2 (a)) and can be classified as Geldart B type. The average sphericity of the sand particles was 0.7 as determined by image analysis. The minimum fluidization velocity ($\boldsymbol{U}_{mf}$) of sand was calculated by measuring the pressure drop across the bed at different air velocities. From the pressure drop profile (Figure 5.2 (b)), $\boldsymbol{U}_{mf}$ was determined to be 5.8 cm/s. Consequently, the experiments were performed with an initial bed height of 35 cm using three different fluidizing air velocities, 1.25, 1.85, and 2.5 $\boldsymbol{U}_{mf}$.

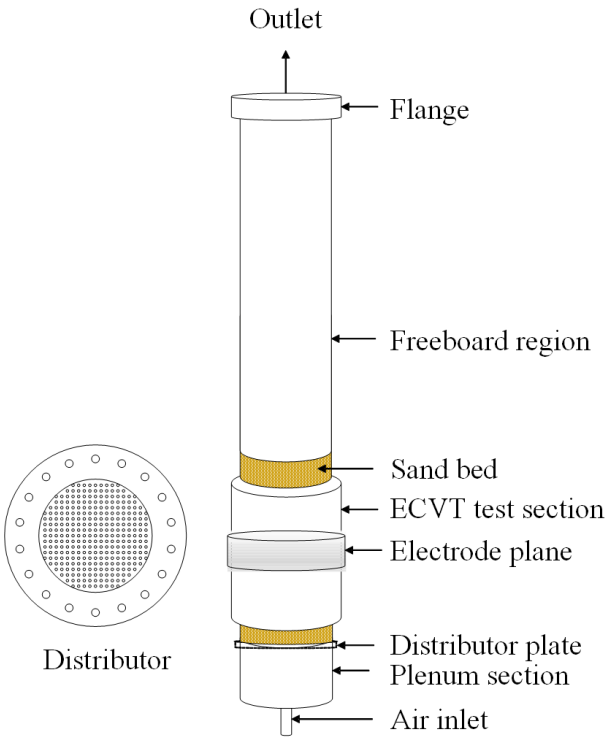

(a)

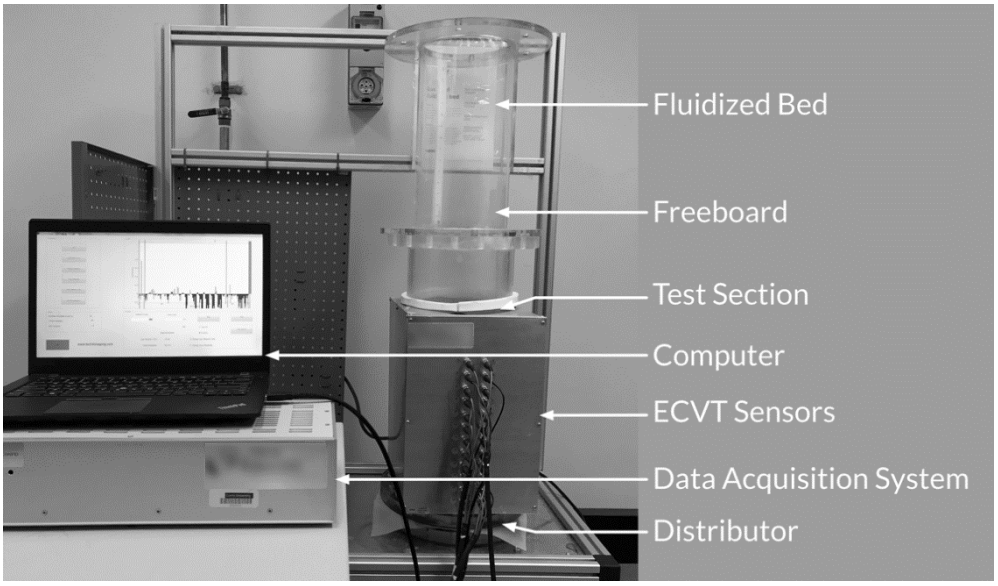

(b)

Figure 5.1 (a) Schematic diagram of the experimental setup and (b) fluidized bed with ECVT sensor and data acquisition system

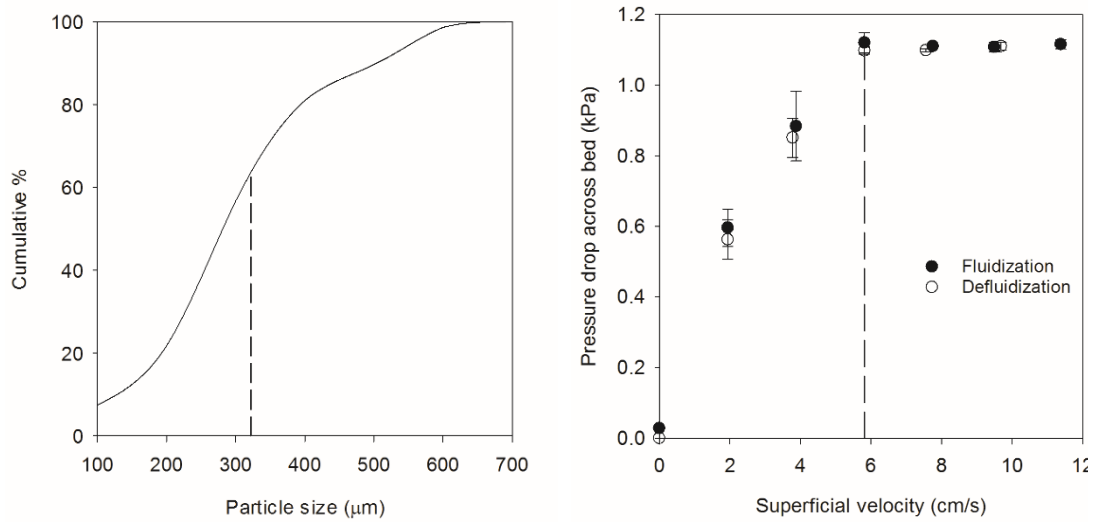

(a) (b)

Figure 5.2 (a) Particle size distribution and (b) variation of pressured drop across the bed with fluidization velocity

5.2.2. Measurement technique

The experimental setup with an ECVT sensor embedded 5 cm above the distributor is displayed in Figure 5.1 (b). The sensor, developed and supplied by Tech4Imaging [194], had a 20 cm diameter and 35 cm length. It consisted of four planes of electrodes with six electrodes on each plane (total 24 electrodes) arranged along the wall. The capacitance between an electrode and another electrode surrounding the bed was captured by the data acquisition system. Such measurements were performed by 24 electrodes. The captured capacitance data were translated to the distribution of solids volume fraction using an image reconstruction algorithm, which provided an image of the flow domain covered by the sensor at a resolution of a 1 cm × 1.75 cm × 1 cm (x × y × z) with 8000 voxels. For calibration of the ECVT sensor, the capacitance was measured for an empty test section and then the section entirely filled with sand. These capacitance data were used to normalize the measurements between 0 and 1 with 0 representing an empty column and 1 representing a completely filled column having the solids volume fraction of 0.63. Before conducting further experiments, tests were

conducted by measuring solids volume fraction in an empty, completely filled, and half–filled column. As recommended by Makkawi and Wright [191], solids volume fraction data were recorded for 60 s at 50 Hz frequency for each experiment. The instantaneous data was time-averaged to report steady-state values. All experiments were conducted three times, and the time-averaged values with error bars representing maximum and minimum values were reported.

5.2.3. Selection of image reconstruction algorithm

The translation of capacitance data to solids volume fraction is a critical post-processing step that is performed using an image reconstruction algorithm. Algorithms such as LBP, NN-MOIRT, and TV-IST were used in previous studies (Table 5.1). In the present study, the effect of the image reconstruction algorithm was investigated by comparing the images from the LBP, LI, and NN-MOIRT algorithms. For this, the bed was completely filled with sand to the upper end of the sensor, and an empty glass beaker of known size was maintained at the center of bed as displayed in Figure 5.3 (a). Then, data were recorded and images were constructed. As indicated in Figure 5.3 (b), LBP resulted in clearer images of the object (beaker) in both horizontal and vertical planes compared to those from the other two algorithms. NN-MOIRT resulted in blurry images, whereas LI resulted in a sharp image in the horizontal plane with a distorted image in the vertical plane. In the LBP images, the transition from dense to lean phase was blurry; whereas an oval shape of the object was visible for the cylindrical beaker. It is clear from Figure 5.3 (b) that a sharp transition between two phases was not captured by any of the algorithms. Of the three algorithms, LBP yielded sharper images that could be used with an optimized threshold to reconstruct the object. Hence, LBP was selected for the post-processing of the data.

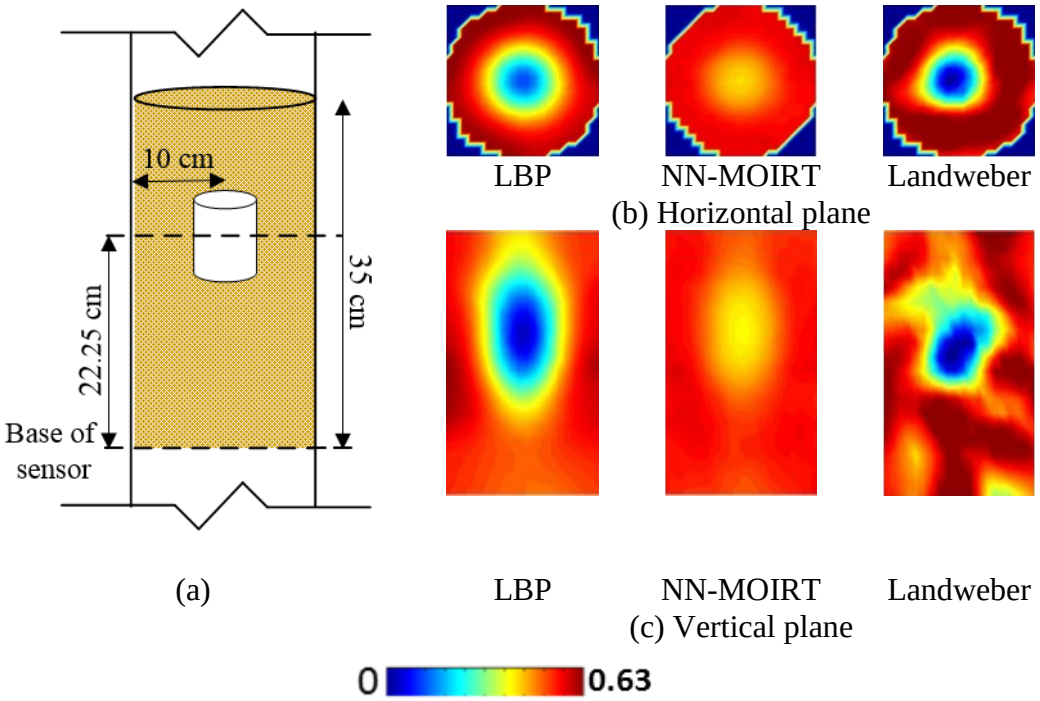

Figure 5.3 (a) Schematic diagram of a stationary bed with empty beaker (Diameter – 5.8 cm), and (b) and (c) comparison of solids volume fraction contours from three image reconstruction algorithms

5.2.4. Calculation of bubble diameter

White [188] conducted static fluidized bed experiments with spherical balls inside the bed and determined that a constant threshold could not capture all the spheres. He recommended a variable threshold for different size balls. To determine a relation between the threshold and size of the bubble, extensive calibration experiments were performed as follows. ECVT data were recorded for the static bed with an empty glass beaker as indicated in Figure 5.3 (a). These experiments were repeated for four different glass beakers (3.5, 5.8, 8.8, and 11.6 cm diameter). It is noteworthy that the selected range of the beaker diameters represents a range of possible bubble diameters in the experimented BFB. Horizontal plane images (Figure 5.3 (b)) at the center of the measurement volume were extracted for all the glass beakers; they were further post-processed using MATLAB to obtain the diameter of the beakers. The contour plot (Figure 5.3 (b)) indicates a gradual transition of solids volume fractions at the bubble surface. MATLAB code was used to calculate the number of pixels having a solids

fraction less than a given threshold in a given horizontal image captured at a particular axial location. The calculated number of pixels was multiplied by the pixel size of 1 × 1 cm^2 and then the calculated value was converted to the beaker diameter. Table 5.2 presents the calculated beaker diameters using different thresholds. The use of a constant threshold resulted in a considerable error. For example, the threshold of 0.189, 0.252, or 0.315 could not detect the presence of a 3.5 cm beaker, whereas threshold above 0.441 significantly overestimated the beaker diameter. Consequently, an optimum threshold that minimizes the error between the predicted and actual beaker diameters were determined by trial and error (Table 5.2).

Table 5.2 Bubble diameters calculated using a constant threshold for a beaker maintained at the center of the bed

Actual diameter (cm)	Beaker diameter (cm) Threshold						Optimum threshold/beaker diameter	Error % in bubble diameter	
	0.189	0.252	0.315	0.378	0.441	0.504		Optimum threshold	Constant threshold 0.315
3.5	0	0	0	3.57	6.08	8.74	0.378/3.57	2	100
5.8	0	1.72	4.47	6.38	8.49	11.2	0.3465/5.86	1.03	22.93
8.8	5.94	6.86	8.14	9.62	11.2	13.5	0.34/8.74	-0.68	7.5
11.6	5.94	7.4	8.39	9.84	11.2	13.1	0.4536/11.61	0.1	27.67

It is known that ECVT is a “soft-field” technique, where measurements depend on the location of an object in the sensor domain. Thus, the optimum threshold found for the beakers maintained at the center of the bed may not be applicable to bubbles at different locations. Consequently, additional calibration experiments were conducted by keeping the beakers at various axial and radial locations. For these experiments, the axial and radial locations were selected in such a way that the base of beakers was located at 10 and 20 cm from the base of the sensor and the sidewall of beakers were positioned at 5 and 10 cm from the wall of the sensor. Figure 5.4 (a) shows positions

of beakers. It should be noted that the selected locations were not near the wall or upper end or bottom part of the sensor. This is because the images of the beakers kept near the sensor ends were highly distorted and least accurate in terms of resolution owing to electric field fringing effect (Tech4imaging, private communication). Figure 5.4 (b) shows the optimum threshold for different beaker sizes kept at various locations. Depending on the size of the beaker, the variation in optimum threshold with location was within 10%.

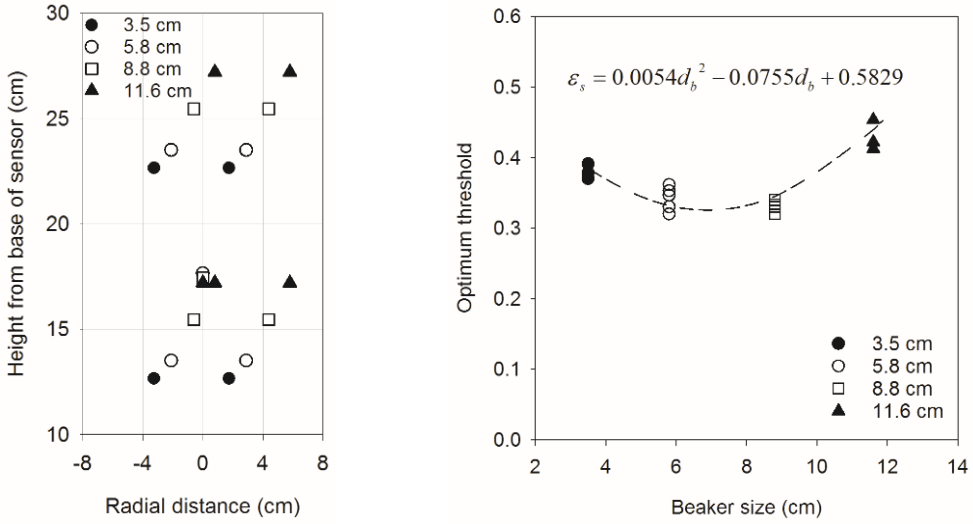

(a) (b)

Figure 5.4 (a) Positions of beakers in the sensor domain and (b) optimum thresholds for different beakers kept at variation locations

Calibration was performed using the average optimal threshold for a given beaker, whereas, the minimum and maximum of optimum threshold were used to establish error bounds on the calculated bubble diameters. An error of ±20% was observed for smaller bubbles (diameter ~ 3.5 cm). The error gradually decreased with increasing bubble diameter. For 11.6 cm bubble, the error was less than ±5%. Consequently, a polynomial function correlating the averaged optimum threshold and bubble diameter was derived.

$$\epsilon_s = 0.0054{d_b}^2 - 0.0755d_b + 0.5829 \quad (1)$$

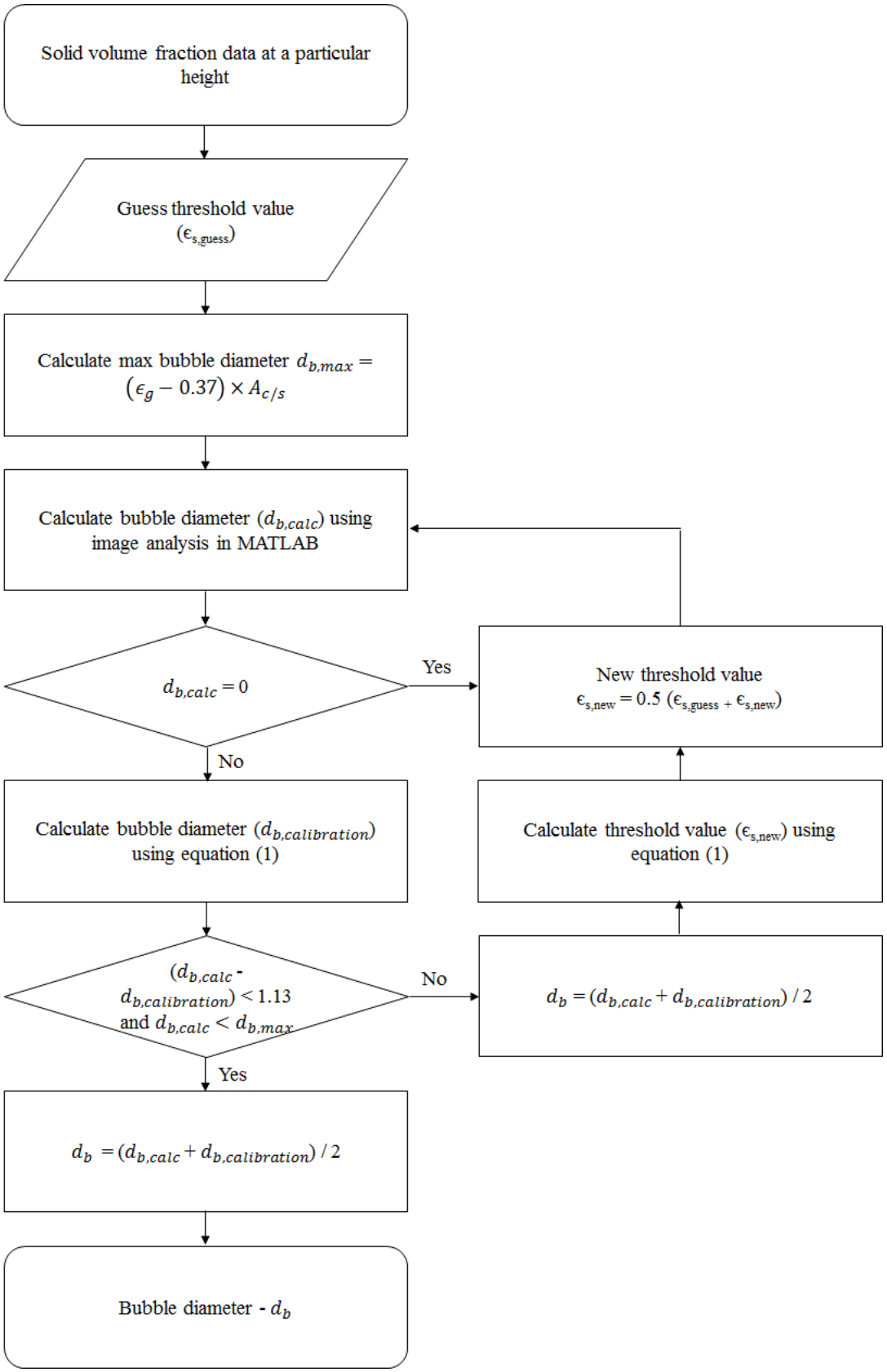

Figure 5.5 Algorithm to calculate bubble diameter

Where, ϵ_s is the averaged optimum threshold and d_b is the bubble diameter. This function was used in the iterative algorithm (Figure 5.5) to calculate bubble diameters. The convergence criteria of the algorithm had two conditions. Firstly, the difference between the bubble diameter calculated by image analysis ($d_{b,calc}$) applying a given threshold and that from the polynomial equation ($d_{b,calibration}$) should be less than one pixel area. Secondly, the $d_{b,calc}$ must be less than or equal to the maximum possible diameter ($d_{b,max}$) which is defined as the diameter of a bubble formed by available excess gas in that particular horizontal plane ((ϵ_g - 0.37) × $A_{c/s}$).

5.2.5. Calculation of bubble velocity

Makkawi and Wright [192] proposed a simple method to calculate bubble rise velocity from instantaneous solids volume fraction data. Following this method, time-series of cross-sectional averaged solids volume fractions at two axial heights (h_1 and h_2) were plotted (Figure 5.6 (a)). Both these time-series were observed oscillating. Assuming a single bubble evolution in the bed (discussed in Section 5.3.2), each large dip in the time series implied the detection of a bubble. When the two time-series were compared, a particular dip at a time t_1 in the time-series at height h_1 could be mapped to a dip at time t_2 in the time-series at height h_2 (with $t_2 > t_1$). For all mapped dips, this implied that the bubble detected at height h_1 was again detected at height h_2, however, after some time Δt (= $t_2 - t_1$). Both (h_2 - h_1) and Δt were used to calculate the rise velocity of the bubble. However, the time series also included fluctuations within a small number of larger dips as displayed in Figure 5.6 (b). For these dips, the identification of a single minima and mapping of the dips was rather difficult. To overcome this challenge, the time series were further post-processed as described below.

For each time series, the consecutive maximum of different peaks (as indicated in colored dots in Figure 5.6 (b)) was determined. These maxima are written as

$$max\ of\ \epsilon_s = \left(\epsilon_{s,max}\right)_{t_1}, \left(\epsilon_{s,max}\right)_{t_2}, \ldots \ldots \left(\epsilon_{s,max}\right)_{t_i}, \ldots, \left(\epsilon_{s,max}\right)_{t_N} \quad (2)$$

Where ϵ_s is the solids volume fraction, $\left(\epsilon_{s,max}\right)_{t_i}$ is the maximum solids volume fraction of a peak at time t_i, the subscript i denotes a time interval number, and t_1 to t_N are the time when $\epsilon_{s,max}$ occurs. These maximum values were used to normalize the time series as follows:

$$\epsilon_{s,norm} = (\epsilon_s)_t - \left(\epsilon_{s,max}\right)_{t_i} \qquad t_i \leq t < t_{i+1} \quad (3)$$

Where $\epsilon_{s,norm}$ is the normalized solids volume fraction and $(\epsilon_s)_t$ is the solids volume fraction at any time t. Eq (3) implies that the signal is normalized by using successive maxima. Assume $\left(\epsilon_{s,max}\right)_{t_1}$ and $\left(\epsilon_{s,max}\right)_{t_2}$ are two consecutive maxima. Then, values between times t_1 and t_2 are normalized by using $\left(\epsilon_{s,max}\right)_{t_1}$. The resulting normalized time series at h_1 and h_2 are displayed in Figure 5.6 (c) with all values less than zero. The normalized time series included dips of different magnitudes with each having distinct minima, and therefore, the mapping of the dips was easier. Rise velocity was calculated for all mapped dips in the two normalized time-series and the average of the calculated velocities was reported as bubble rise velocity at a given height $(h_1 + h_2)/2$. For data collected over 60 s, 90–100 mapped dips were obtained and it was determined that 50 mapped dips were sufficient to obtain statistically invariant data.

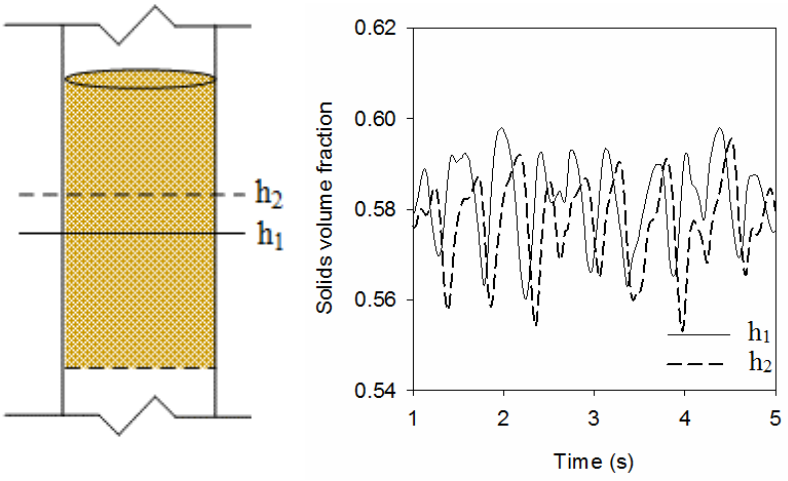

(a)

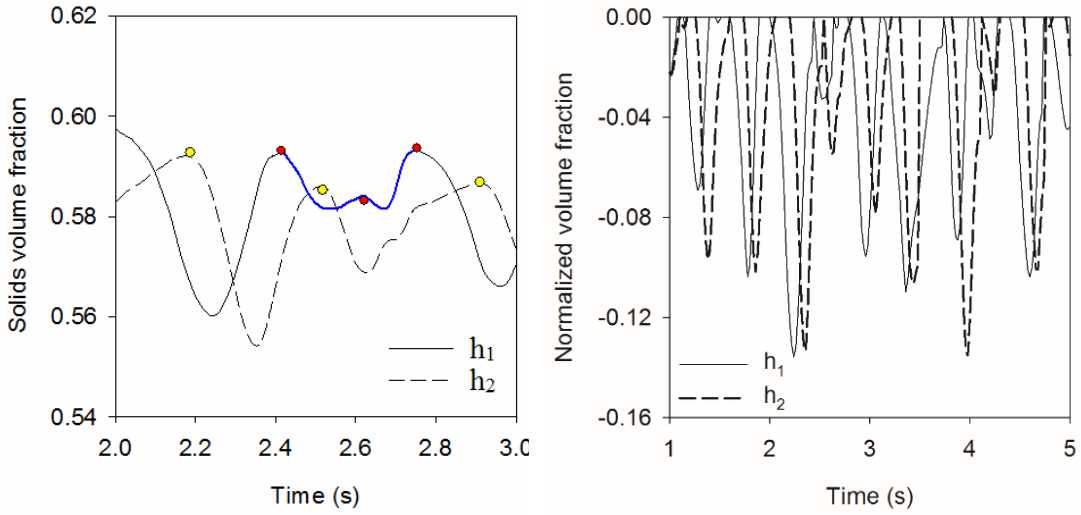

(b) (c)

Figure 5.6 (a) Variation of solids volume fraction at two heights, (b) fluctuations within a dip, and (c) normalized time series

5.3. **Results and discussion**

5.3.1. Distribution of solids volume fraction

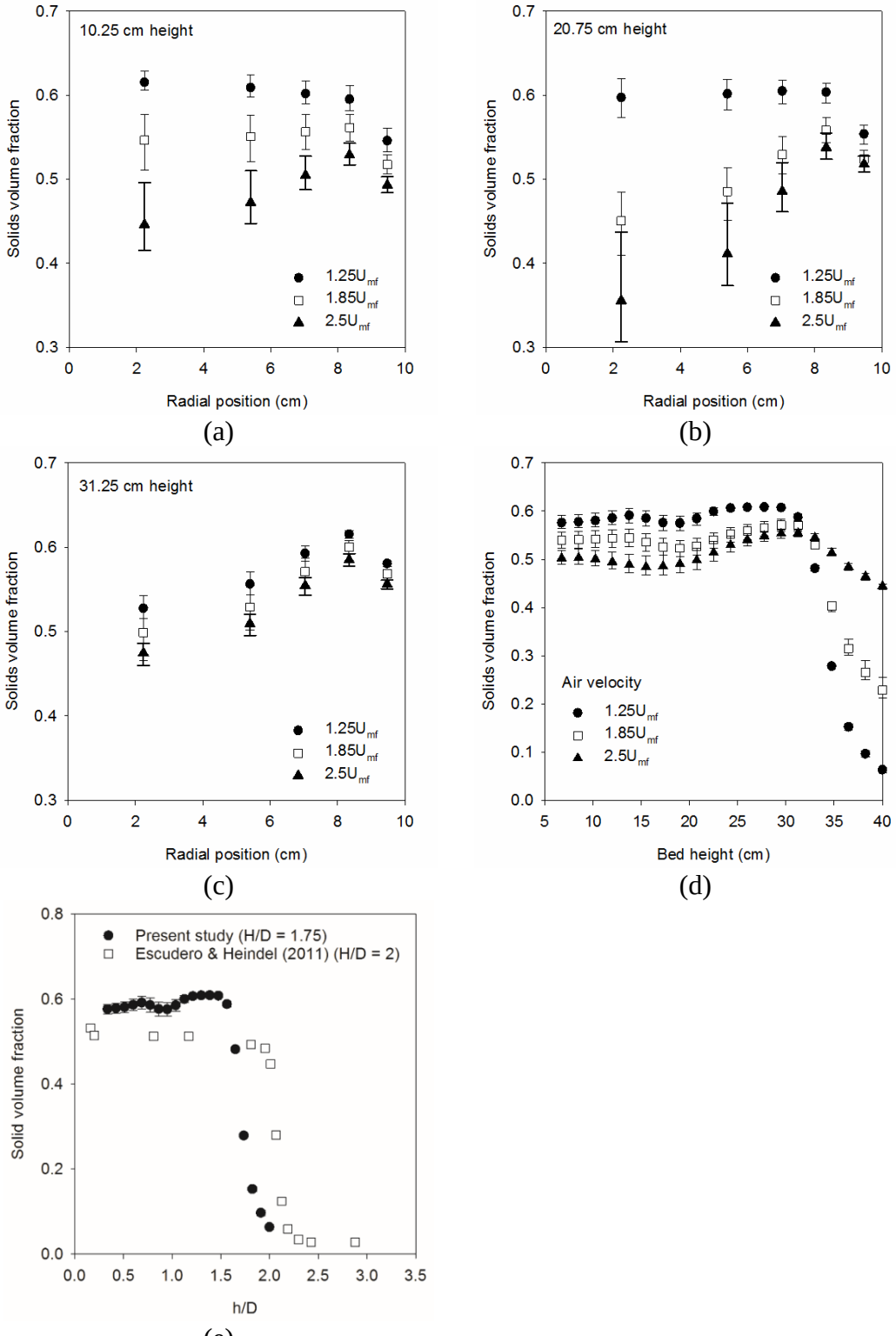

Figure 5.7 Radial profiles of solids volume fraction at (a) 10.25 cm, (b) 20.75, (c) 31.25 cm, (d) axial profile of solids volume fraction (e) comparison of axial profile of solids volume fraction with literature data

Time-averaged radial distributions of solids volume fraction at three different axial locations (10.25, 20.75, and 31.25 cm above the distributor) are displayed in Figure 5.7 (a), (b), and (c), respectively. At 10.25 and 20.75 cm, profiles at 1.25 $\boldsymbol{U}_{mf}$ were flat with values close to the maximum packing of 0.63. This was mainly due to low excess gas available for bubble formation at such a low fluidization velocity. At higher velocities (1.85 and 2.5 $\boldsymbol{U}_{mf}$), higher excess gas caused bubble formation leading to lower solids volume fraction and a core-annulus structure with high solids volume fraction near the wall and low values at the center of the bed. Escudero and Heindel [72] also observed a core-annulus structure at higher fluidization velocity at a height above H/D of one. They observed that rising gas bubbles coalesced and migrated toward the center of the bed, causing high gas holdup in the center region. They also observed that larger bubbles erupt at the top of the bed and throw solids towards the wall. Both the coalescence and eruption of bubbles causes a core-annulus profile in fluidized beds. Solids volume fraction decreased with an increase in gas velocity at all three velocities (Figure 5.7). However, the decrease near the wall was minor compare to that at the center of the bed. This implies that higher fluidization velocity does not promote mixing near the wall; rather it causes channeling of gas in the center region. The variation of solids volume fraction along the height is indicated in Figure 5.7 (d). It remained virtually constant; however, it decreased with an increase in fluidization velocity. After a height of approximately 27–30 cm, solids volume fraction declined, with the decline being rather steep for 1.25 $\boldsymbol{U}_{mf}$ compared to the other two velocities. This decline can be attributed to the eruption of bubbles and expansion of the bed near the top. At a low velocity of 1.25 $\boldsymbol{U}_{mf}$, bed expansion was less than the sensor height and hence, the solids volume fraction began declining at approximately 27 cm height and approached zero at 40 cm height. At 2.5 $\boldsymbol{U}_{mf}$, bed expansion covered the entire

sensor height (up to 40 cm) and thus, the decline in solids volume fraction began at approximately 32 cm height; however, the bed had more than 40% solids at 40 cm height. The axial profile of solids volume fraction at 1.25 $\boldsymbol{U}_{mf}$ was also compared with the data of Escudero and Heindel [72], who conducted BFB experiments of Geldart B particles using X-ray. A good qualitative agreement was found for the solids volume fraction profile (Figure 5.7 (e)). The discrepancy in values can be attributed to the differences in the column diameter, initial bed height, and particle properties.

5.3.2. Bubble evolution

The time series of solids volume fraction at 22.5 cm height for all three fluidization velocities are displayed in Figure 5.8 (a). The time series indicated fluctuations around a certain average value that decreased with an increase in the velocity. The scale of fluctuations increased with an increase in the air velocity. This suggests that the bed became increasingly chaotic with a rise in air velocity. For 2.5 $\boldsymbol{U}_{mf}$, fluctuations in the time series with a small number of peaks between 30–32 s are indicated in Figure 5.8 (b). Each dip represents a bubble. Corresponding to the first dip in Figure 5.8 (b), contours of solids volume fraction in a 2D slice at 22.5 cm height are displayed in Figure 5.8 (c). These contours demonstrate the evolution of a single bubble passing through the 22.5 cm bed height. The bubble that formed between 30.2 and 30.32 s was attached to the wall and then increased in size between 30.32 and 30.44 s. It then detached from the wall between 30.48 and 30.50 s, and began growing opposite to its previous position. The detachment of the bubble may have caused the minor dip beginning at approximately 30.5 s in the time series. After the detachment, the bubble continued growing between 30.50 and 30.60 s. It then gradually disappeared from the 2D frame during the last few fractions of a second. The contours clearly suggest a

single bubble passing through a given height with both bubble size and position varying with time.

The evolution of 3D bubbles corresponding to 2D contours of Figure 5.8 is shown in Figure 5.9, where 2D contours in a vertical plane and corresponding 3D bubbles obtained by applying a constant (0.315) and optimum thresholds are presented for a period of 0.30 s, starting from 30.2 s. It can be seen that both the 2D contours and reconstructed bubbles captured the complex flow behavior within the fluidized bed. However, the images reconstructed using the constant threshold missed a large number of bubbles as highlighted in Figure 5.9 (a), (e), (f), (g), and (h). The reconstructed bubbles using the constant threshold were also much smaller compared to voids seen in the 2D contours. On the other hand, the reconstructed bubbles using the optimal threshold were consistent with the 2D contours. Using optimum threshold, several additional bubbles were identified. However, optimal threshold was not able to identify bubbles that were close to each other. For example, in Figure 5.9 (g), one can visually distinguish three bubbles but the optimum threshold method resulted in a single elongated bubble. Such discrepancy was also noticed when two bubbles were very close to each other at the same axial plane. When two bubbles were sufficiently apart (such as in Figure 5.9 (i)), the optimal threshold method could identify two distinct bubbles. It is possible to further increase the number of bubbles identified by using high-resolution ECVT sensor and further tuning of the algorithm.

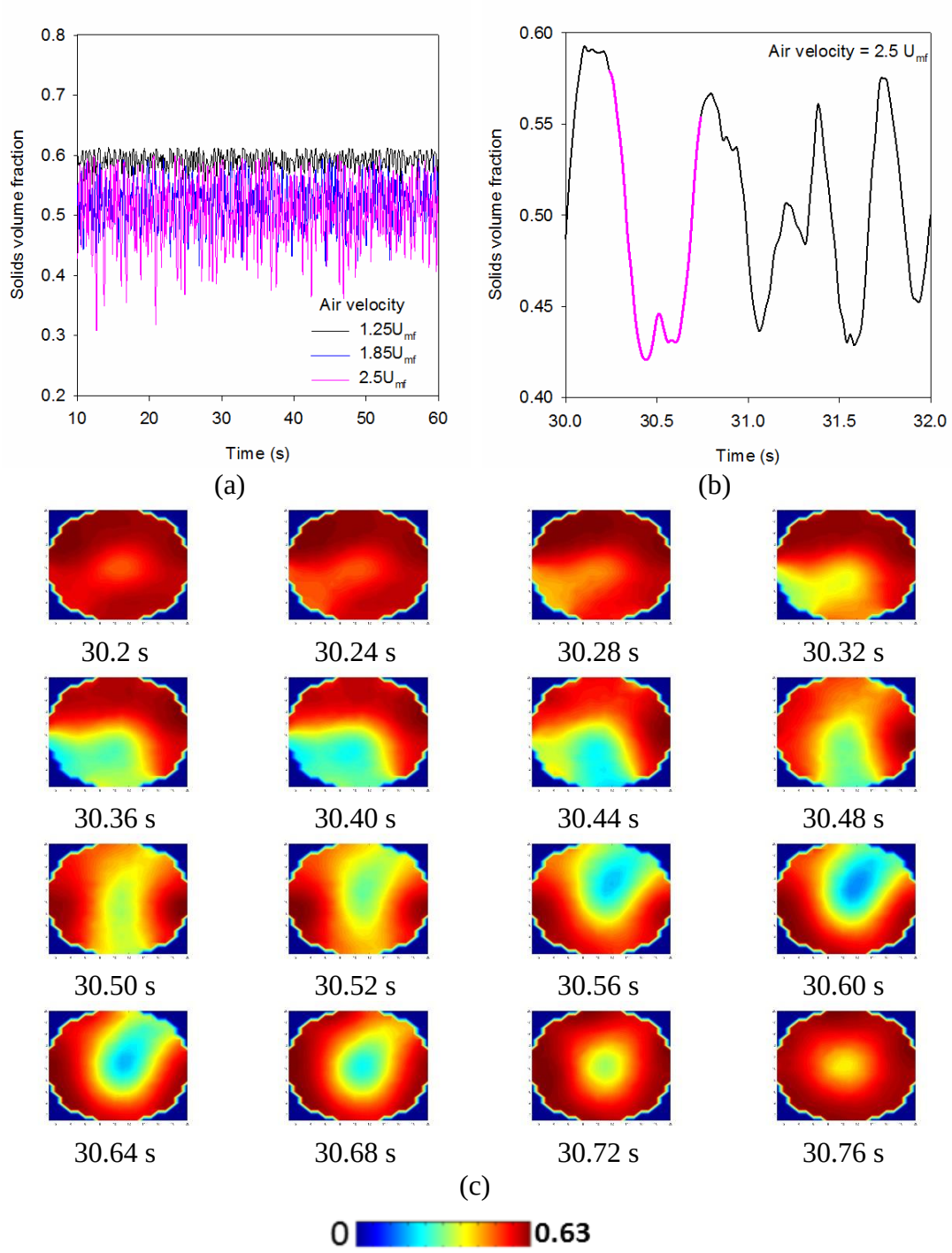

Figure 5.8 (a) Time series of solids volume fraction at 22.5 cm height, (b) fluctuations in the time series between 30 and 32 s, and (c) evolution of a bubble in a cross section at 22.5 cm height.

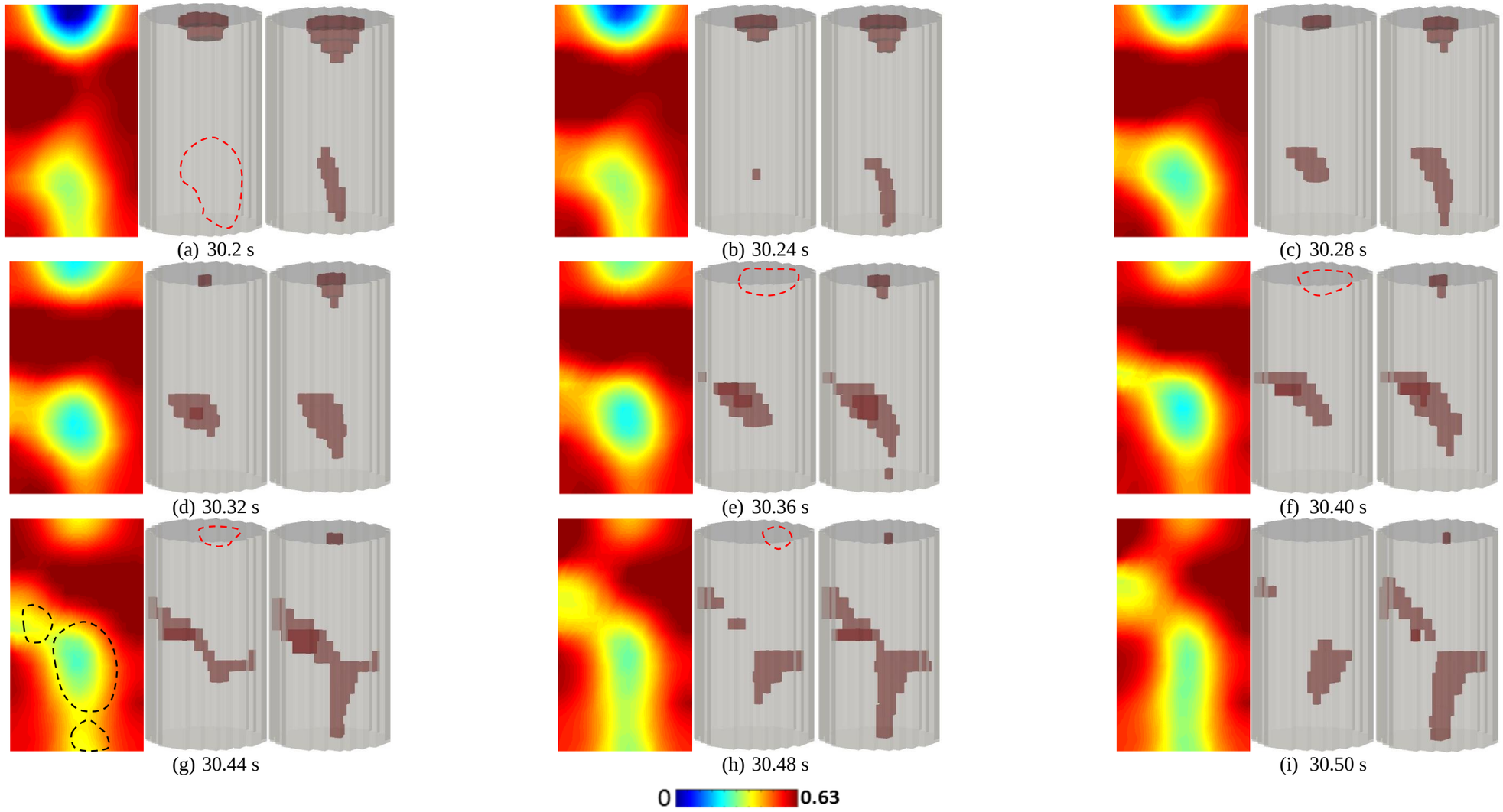

Figure 5.9 Contour of solid volume fraction and calculated 3D bubbles from constant (0.315) and optimum threshold

5.3.3. Bubble frequency

Makkawi and Wright [191] used time series of average solids volume fraction at a particular height to calculate the bubble cycle frequency, which is defined as half of the total number of times a signal passes over its mean (N_c) in a given time interval. Using this method, bubble frequency (f_b) is equal to $N_c \,/\, 2T$, where T represents the total sampling period in seconds. The variation in bubble frequency with distance from the distributor is displayed in Figure 5.10 (a). Bubble frequency decreased with bed height and increased with superficial air velocity. Many researchers [34,61,191,195] analyzed bubble frequency by plotting the power spectra density (PSD) of solids volume fraction time series. In PSD analysis, the dominant frequency is considered as the bubble frequency in the case of BFB and amplitude can be linked to bubble size. For a single bubble of uniform size, a sharp single peak appears in the PSD plots [61]. In the case of BFB, a wide band of dominant frequencies is observed; this signifies that different sizes of bubbles appear either at the same locations or at different times. Figure 5.10 (b), (c), and (d) display the PSDs of solids volume fraction time series at 22.5 cm height for the three air velocities. The amplitude in PSDs increases with an increase in air velocity. This was consistent with higher bubble size resulting from higher air velocity. The PSDs indicated no clear peak or single dominant frequency; however, they had several peaks appearing over the band of 1 to 4 Hz. This implies that different sizes of bubbles pass through a given bed height as indicated in Figure 5.8 (c).

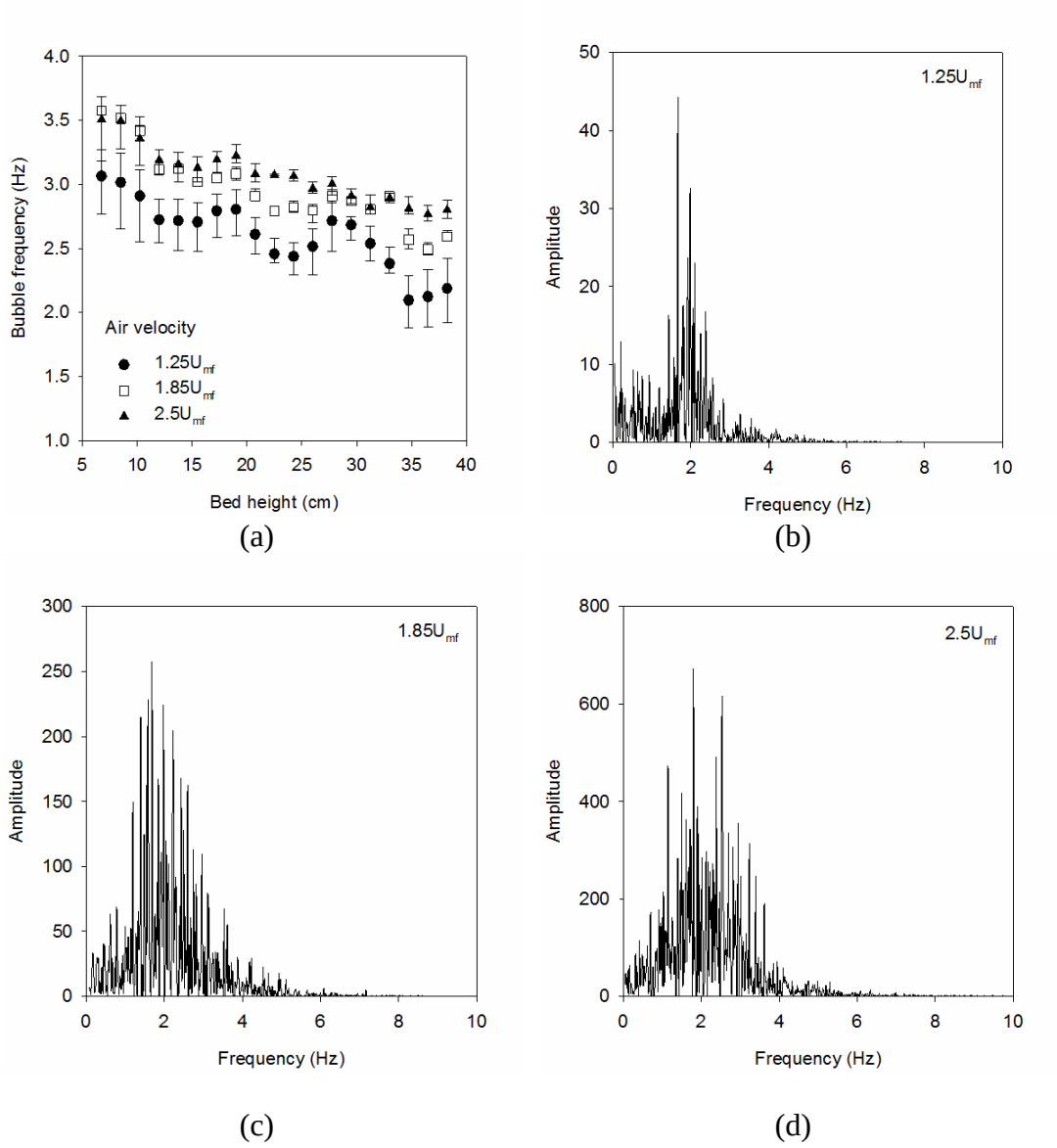

Figure 5.10 (a) Variation of bubble frequency along bed height; (b), (c), and (d) power spectra density plots of solids volume fraction time series at 1.25, 1.85, and 2.5$\boldsymbol{U}_{mf}$, respectively

5.3.4. Bubble diameter

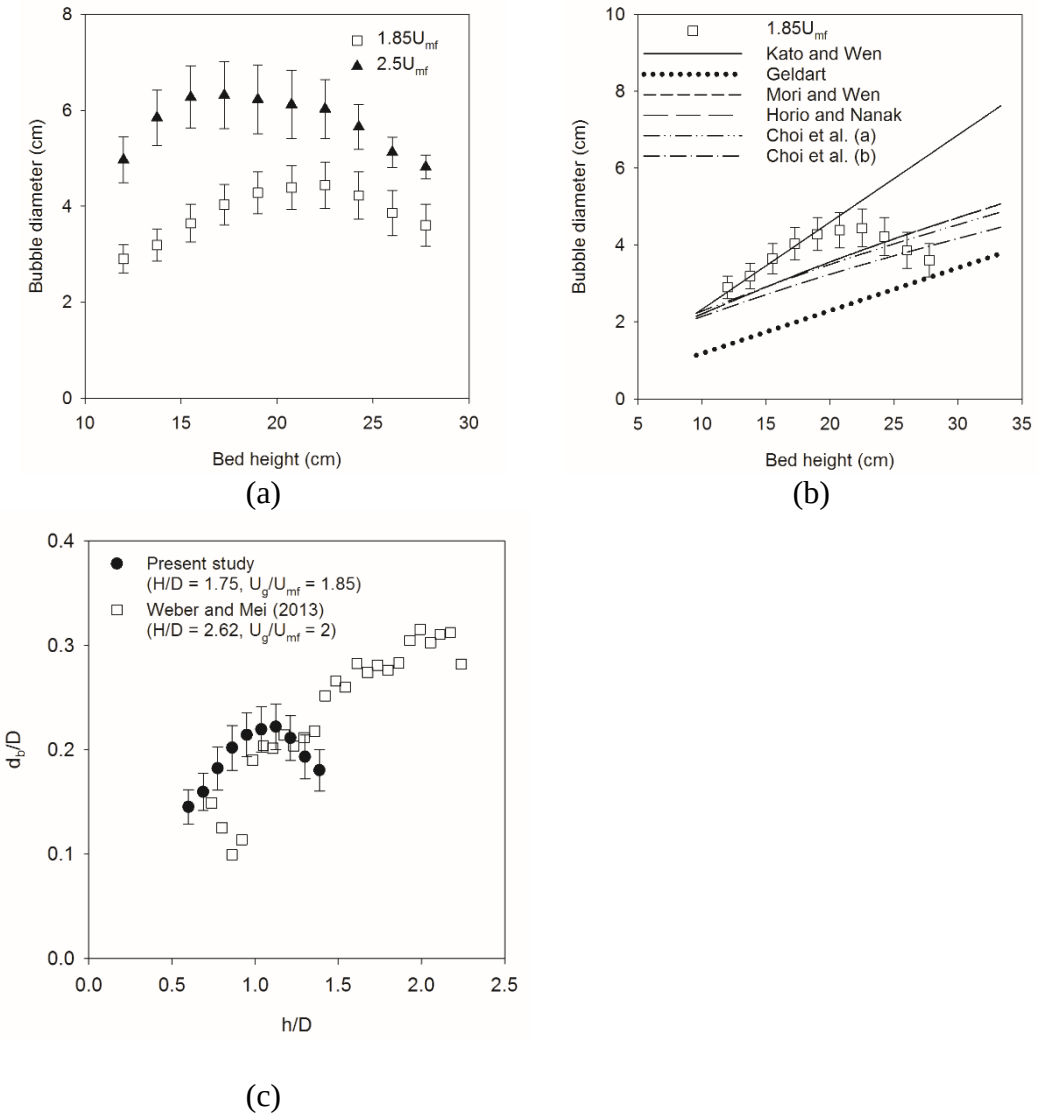

Figure 5.11 (a) Variation of bubble diameter along bed height (b) comparison between calculated bubble diameters from ECVT data and those calculated from empirical correlations, and (c) comparison of axial profile of bubble diameter with literature data

Bubble diameters at axial locations between 12 – 27 cm bed heights, where the calibration experiments were conducted, were calculated for superficial air velocities of 1.85 and 2.5 $\boldsymbol{U}_{mf}$ by applying the iterative method described in Section 5.2.4. Figure 5.11 (a) displays a variation of bubble diameter with axial distance from the distributor. At both 1.85 and 2.5 $\boldsymbol{U}_{mf}$, bubble size increased between ~12 to 20 cm

bed heights and then decreased. The increase in bubble size can be attributed to coalescence of smaller bubbles formed at the bottom section, whereas the decrease in bubble size can be attributed to the splitting of bubbles.

A comparison of the calculated bubble diameters from the ECVT data with those calculated from different empirical correlations [8,12,196–199] is displayed in Figure 5.11 (b). The growth of the bubble diameter between 12 and 20 cm bed height reasonably agreed with that calculated by the correlation of Kato and Wen [8]. The estimated bubble diameters were closer to the correlations of Choi et al. [199], Horio and Nonaka [12], and Mori and Wen [197], whereas the correlation of Geldart [196] significantly underestimated the estimated values. In 20–27 cm bed height, a declining trend of bubble diameter from the ECVT data did not match with a monotonically increasing profile of the empirical correlations. The calculated bubble diameters of the present study were also compared with that reported by Weber and Mei [55] (Figure 5.11 (c)). Up to the bed height of 1.25 h/D, both the data sets showed increasing bubble diameter with values comparable to each other. After h/D of 1.25, the current data showed a decrease in bubble diameter whereas those of Weber and Mei [55] showed a steady increase.

The declining trend of bubble diameter after the bed height of 20 cm can be attributed to splitting of bubbles as captured in Figure 5.9. Shen et al. [14] also observed a sharp decline in bubble diameter at a top section of the bed. He defined a critical height h^* after which bubbles became unstable due to its size and then split into more than one. However, it should be noted that the current data suggest the bubble splitting at the middle height of the bed (~20 cm) whereas Shen et al. [14] reported such phenomena at extremely top part of the bed. Werther [198] reported a stable bubble diameter after a certain height, where the equilibrium between coalescence of smaller bubbles and

splitting of larger bubbles established. However, the current data did not show a stable bubble diameter. Besides splitting of bubble at the middle of the bed, another possible reason for this discrepancy might be the wide particle size distribution used in the present study. Beestra et al. [200], Rautenbach et al. [80,201] and Brouwer et al. [202] have reported a decrease in bubble diameter with the presence of fines in the bed. Furthermore, bi-dispersed fluidized bed experiments [112,125,126] suggested that fine particles segregated at the top of the bed at low fluidization velocity. Such segregation can also affect bubble properties in the different region of the bed. In the present study, particles size varied from 100 to 600 µm with 6% particles less than 100 µm.

5.3.5. Bubble rise velocity

Bubble rise velocities at three axial locations (10.25, 17.25, and 24.25 cm from the distributor) were calculated using the method described in Section 5.2.5. Figure 5.12 (a) indicates that bubble rise velocity increased with an increase in both air velocity and bed height. This can be attributed to the growth in bubble size between 10–25 cm height (Figure 5.11), resulting in a higher buoyancy of the bubbles. At 1.25 $\boldsymbol{U}_{mf}$, the increase in the rise velocity was observed between 10.25 and 17.25 cm heights; the increase was muted between 17.25 and 24.25 cm. For both 1.85 and 2.5 $\boldsymbol{U}_{mf}$, the bubble rise velocity increased steadily from 10.25 to 24.25 cm height. Different empirical correlations are available in the literature to predict bubble rise velocity in gas-solid fluidized beds [11,203,204]. The bubble rise velocities estimated from the ECVT data were compared with those calculated using empirical correlations (Figure 5.12 (b)). The trend of the estimated values agreed with that calculated using the correlations [11,66,198,203,204]. Quantitatively, the estimated values were closer to those from the correlation of Werther [198]; the correlation of Dry et al. [204] resulted in significantly higher values. The discrepancy between the experimental values and

those from the correlation of Dry et al. [204] was also observed at the other two air velocities; whereas experimental values were consistently in agreement with those from the correlation of Werther [198]

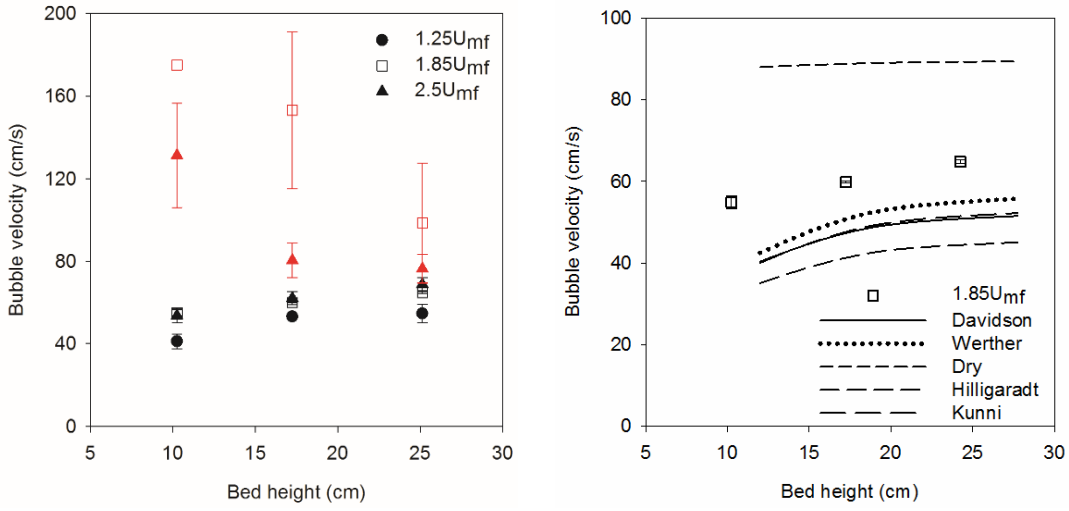

(a) (b)

Figure 5.12 (a) Variation of bubble rise velocity along bed height and (b) comparison between calculated bubble velocity from ECVT data and those calculated from empirical correlations

Previous studies [63,205] also used the cross-correlation (CC) method to calculate the bubble rise velocity. In this method, the CC function $\left(R(j)\right)$ (eq. 4) from the solids volume fraction time series captured at two heights (h_1 and h_2) was calculated as

$$R(j) = \frac{1}{n}\sum_{i=1}^{n} x(i\Delta) \times y(i\Delta + j\Delta) \qquad j = 1,2,3,\ldots,m \qquad (4)$$

Where, x and y are the solids volume fraction time series at h_1 and h_2 respectively, Δ is the sampling interval, n is the number of sample intervals, m is the number of samples in the CC function and j is the time delay. The CC function will give the time interval (k′) when the similarity index between the two time series is maximum. The time lag ($\tau_{max} = \mathrm{k}'\Delta$) is then used to calculate the bubble rise velocity ($h_2 - h_1/\tau_{max}$). In the current study, rise velocity calculated from CC and signal

analysis method described in Section 5.2.5 were compared in Figure 5.12 (a). It should be noted that the CC function values for 1.25 $\boldsymbol{U}_{mf}$ is not reported in Figure 5.12 (a), as no time lag could be determined for two time series. For 1.85 $\boldsymbol{U}_{mf}$ and 2.5 $\boldsymbol{U}_{mf}$, the CC method resulted in significantly higher values than those calculated by signal analysis. Further, the values from the CC method did not show an increasing bubble velocity as resulted by the empirical correlations. In the CC method, the lag was found at the highest similarity between two time series, whereas the signal analysis method uses the average lag calculated for all mapped dips in two time series. The CC method is influenced by noise and frequency of measurement, whereas the signal analysis method filters out the noise before mapping of dips. Thus, the values from the signal analysis method is more reliable and resulted in values that were qualitatively consistent with the empirical correlations.

5.4. **Conclusion**

BFB experiments (sand-air, D = 20 cm, and H/D = 1.75) were performed at three fluidization velocities (1.25, 1.85, and 2.5 $\boldsymbol{U}_{mf}$). ECVT was used to measure the distribution of solids volume fraction, which was further analyzed to estimate diameter, rise velocity, and frequency of bubbles. The previous studies used a constant threshold value between 0.3 and 0.35 to post-process their data and estimate the size of bubbles. The present study conducted extensive calibration experiments using a static fluidized bed with a known size beaker. It was determined that a low threshold value between 0.189 and 0.315 could not detect the presence of small bubbles (< 3.5 cm). The data from the calibration experiments were used to develop an iterative method to determine the optimum threshold for each 2D image. The profiles of the bubble diameter along the bed height indicated bubble growth up to the middle height

(~20 cm) of the bed, after which bubble diameter decreased. The growth of the bubbles was consistent with that calculated by the empirical correlation of Kato and Wen [8]. The growth of bubbles also caused an increase in the bubble rise velocity. The estimated bubble rise velocities reasonably agreed with the correlation of Werther [198]. The estimated bubble frequency was in a band of 2–4 Hz at three fluidization velocities. The contours of solids volume fraction and 3D bubbles calculated by optimum threshold suggested that the size and shape of the bubbles continuously varied owing to the coalescence, elongation, attachment and detachment with the wall, breakup, and eruption of the bubbles.

6 Closure

6.1. Conclusion

In this thesis, gas-solid hydrodynamics of mono and bi-dispersed BFBs was investigated by conducting CFD simulations (chapters - 3 and 4) and experiments (chapter-5). The experiments were conducted using the ECVT technique, while the simulations were performed using CFD-DEM gas-solid flow model. Chapter-wise specific conclusions are summarised below.

Chapter–3: Effect of drag model on CFD–DEM predictions of mono–dispersed BFBs

This study investigated the effect of six different drag models namely Syamlal–O'Brien, Di Felice, Gidaspow, EMMS, BVK, and Ayeni models on CFD–DEM predictions of two different BFB systems given by Goldschmidt et al. [13] and NETL challenge problem [56]. The key conclusions of this study are:

1) Di Felice model predicts higher drag force compared to other drag models considered in this study. Consequently, bubble size obtained from Di Felice model was also larger and comparable to experimental data of Goldschmidt et al. at 1.5 and 2 $\boldsymbol{U}_{mf}$. Whereas, Di Felice overpredicted the bubble size at 1.25 $\boldsymbol{U}_{mf}$. The simulation using other drag models except for Di Felice and Syamlal–O'Brien, did not even predict the bubble formation at 1.25 $\boldsymbol{U}_{mf}$.
2) For the experimental data of Goldschmidt et al., the discrepancy in predicting the average particle height by all the drag models and at all superficial velocity was within the range of 11–45 % with Di Felice predicting the least discrepancy of less than 16 %.

3) All drag models were able to capture the core–annulus structure of BFB, as can be deduced from the profiles of Eulerian vertical velocity and volume fraction contours.
4) The qualitative profile of horizontal and vertical velocity was captured by all the drag models for experimental data of NETL challenge problem. However, quantitatively, different drag models gave closer predictions at different gas velocity. For instance, Eulerian vertical velocity was reasonably predicted by EMMS at 2 and 3 $\boldsymbol{U}_{mf}$ whereas, at 4 $\boldsymbol{U}_{mf}$, EMMS overpredicted the Eulerian vertical velocity. Whereas, Di Felice captured the Eulerian vertical velocity reasonably well at 4 $\boldsymbol{U}_{mf}$.
5) There was a wide discrepancy in predicting the granular temperature by all the drag models and at all superficial velocities except by the Ayeni model, which predicted well at 2 $\boldsymbol{U}_{mf}$. However, at 3 and 4 $\boldsymbol{U}_{mf}$, Ayeni underpredicted the granular temperature.
6) None of the drag models were able to predict the flow properties at all the flow conditions consistently. However, analysis of overall discrepancy suggested that the Ayeni and Di Felice models result in minimum discrepancy, while commonly used Gidaspow model results in the maximum discrepancy.

Chapter–4: Effect of initial bed configuration on mixing in bi–dispersed BFB

The effect of initial bed configuration on the extent and time of mixing was studied by conducting CFD–DEM simulations of bi-dispersed BFBs with four different initial bed conditions. The key conclusions of this study are

1) CFD–DEM simulations using Syamlal–O'Brien drag model reasonably predicted the PSN for biomass of size 900 μm mixed with sand of 550 μm.

However at another operating condition ($d_{p,Biomass}$ = 550 µm and $d_{p,Sand}$ = 550 µm), Syamlal–O'Brien underpredicted the PSN. This finding was consistent with our finding in Chapter–3, where no drag model consistently predicted the flow properties at different flow conditions.

2) Bubble formation in the bi–dispersed fluidized bed was consistent with the Rowe and Nienow [30] observation, with the first bubble forming in the flotsam biomass phase.
3) For the three segregated configurations considered, the ideal initial segregated configuration was Case–2, when biomass was at the top of the sand phase. In the other two configurations (Case–3 and Case–4), biomass and sand tend to first realign themselves to the ideal configuration (Case–2) and then start mixing with each other. Consequently, mixing time required for Case–3 and Case–4 is more than that required for Case–2.
4) Mixing is non–uniform in the axial direction, as determined by the dispersion coefficient. This could be validated by our observation that, in the axial direction, mixing is governed by the formation, propagation, and eruption of the bubbles while in the lateral direction, it is governed by coalescence of bubbles.

Chapter–6: ECVT measurements of bubble properties

The experiments of a mono-dispersed BFB were conducted using the ECVT technique to determine the bubble properties – diameter, rise velocity and eruption frequency. The key conclusions of this study are:

1) Owing to "soft–field" nature of ECVT, optimal threshold value differed for the beakers of the same size but kept at a different location.

2) An iterative algorithm was proposed to determine optimal threshold for a given ECVT image. The proposed algorithm was able to predict the bubble diameter consistent with the empirical correlation of Kato and Wen [8] up to the middle height of the bed. After that, bubble diameter calculated from empirical correlations increased monotonically with bed height whereas, that calculated from iterative algorithm starts decreasing, owing to bubble splitting.
3) 3D bubble reconstructed using the optimal threshold was able to capture the complex bubbling phenomena – formation, propagation and splitting which were also observed in 2D contours of solids volume fraction.
4) Signal analysis method was proposed to calculate the bubble rise velocities from the raw ECVT data of solids volume fraction, and the results were reasonable with the correlation of Werther [198].
5) The contours of solids volume fraction and 3D bubbles calculated by optimum threshold suggested that the size and shape of the bubbles continuously varied owing to the coalescence, elongation, attachment, and detachment with the wall, breakup, and eruption of the bubbles.

6.2. Recommendation for future work

Based on the investigations conducted in this thesis, following recommendations for future work are made.

1) In the present DEM simulations as well as in literature, most of the particles are assumed to be spherical, neglecting their artefacts such as porous nature, or irregular shape. These features can change the hydrodynamic behaviour of the bed. Therefore, comprehensive comparison should be made between CFD-

DEM models with spherical particles and ones that include irregular and porous nature of the particle.

2) Effect of drag models on CFD–DEM predications under different operating condition was carried out for Geldart–D type particles. Similar simulations for Geldart–B and Geladrt–A particles and for bi–dispersed BFB should also be performed to comprehensively understand the ability of available drag models in predicting the hydrodynamics of gas–solid BFB.
3) Most of the experiments to determine the extent of mixing in bi–dispersed BFB have been carried out by using the collapsed bed. In collapsed bed, air supply to bi-dispersed BFB is suddenly switched off and then fraction of solids is measured by sieving the collapsed bed or using the non-invasive tomographic technique. Mixing of solids has also been measured by high speed imaging, which allows the calculation of mixing at the walls only. Therefore, efforts should be made to develop a non-invasive techniques that can measure the mixing of solids in 3D fluidized bed and under the dynamic condition.

In summary, both experiment and simulation work is required to understand multiscale nature of gas-solid flows. The experimental work should be planned to provide accurate measurement of bubble properties and mixing/segregation of solids in bi-dispersed bed. Simulations, on the other hand, should complement the experiments and the uncertainty affecting the results of CFD such as the effect of different drag models should be comprehensively understood and efforts should be made to minimize these uncertainties.

References

[1] S. Aramideh, Numerical simulation of biomass fast pyrolysis in fluidized bed and auger reactors, Iowa State University, 2014.

[2] M. Alizadeh, N. Mostoufi, S. Pourmahdian, R. Sotudeh-Gharebagh, Modeling of fluidized bed reactor of ethylene polymerization, Chem. Eng. J. 97 (2004) 27–35. doi:10.1016/S1385-8947(03)00133-5.

[3] M. Stein, Y.. Ding, J.P.. Seville, D.. Parker, Solids motion in bubbling gas fluidised beds, Chem. Eng. Sci. 55 (2000) 5291–5300. doi:10.1016/S0009-2509(00)00177-9.

[4] C.R. Müller, J.F. Davidson, J.S. Dennis, A.N. Hayhurst, A Study of the Motion and Eruption of a Bubble at the Surface of a Two-Dimensional Fluidized Bed Using Particle Image Velocimetry (PIV), Ind. Eng. Chem. Res. 46 (2007) 1642–1652. doi:10.1021/ie0611397.

[5] X. Fan, D.J. Parker, Z. Yang, J.P.K. Seville, J. Baeyens, The effect of bed materials on the solid/bubble motion in a fluidised bed, Chem. Eng. Sci. 63 (2008) 943–950. doi:10.1016/j.ces.2007.06.045.

[6] K.A. Buist, A.C. van der Gaag, N.G. Deen, J.A.M. Kuipers, Improved magnetic particle tracking technique in dense gas fluidized beds, AIChE J. 60 (2014) 3133–3142. doi:10.1002/aic.14512.

[7] R.F. Mudde, H.B.M. Schulte, H.E.A. van den Akker, Analysis of a bubbling 2-D gas-fluidized bed using image processing, Powder Technol. 81 (1994) 149–159. doi:10.1016/0032-5910(94)02873-7.

[8] K. Kato, C.Y. Wen, Bubble assemblage model for fluidized bed catalytic

reactors, Chem. Eng. Sci. 24 (1969) 1351–1369. doi:10.1016/0009-2509(69)85055-4.

[9] R.C. Darton, R.D. LaNauze, J.F. Davidson, D. Harrison, Bubble Growth Due to Coalescence in Fluidized Bed, Trans Inst Chem Eng. 55 (1977) 274–280.

[10] J. Werther, Influence of the distributor design on bubble characteristics in large diameter gas fluidized beds, in: Fluid. Cambridge Univ. Press. London, 1978: pp. 7–12.

[11] K. Hillegardt, J. Werther, Local bubble gas hold-up and expansion of gas/solid fluidized beds, Ger. Chem. Eng. 9 (1986) 215–221. http://cat.inist.fr/?aModele=afficheN&cpsidt=8772846.

[12] M. Horio, A. Nonaka, A generalized bubble diameter correlation for gas-solid fluidized beds, AIChE J. 33 (1987) 1865–1872. doi:10.1002/aic.690331113.

[13] M.J.V. Goldschmidt, R. Beetstra, J.A.M. Kuipers, Hydrodynamic modelling of dense gas-fluidised beds: comparison and validation of 3D discrete particle and continuum models, Powder Technol. 142 (2004) 23–47. doi:10.1016/j.powtec.2004.02.020.

[14] L. Shen, F. Johnsson, B. Leckner, Digital image analysis of hydrodynamics two-dimensional bubbling fluidized beds, Chem. Eng. Sci. 59 (2004) 2607–2617. doi:10.1016/j.ces.2004.01.063.

[15] A. Busciglio, G. Vella, G. Micale, L. Rizzuti, Analysis of the bubbling behaviour of 2D gas solid fluidized beds: Part I. Digital image analysis technique, Chem. Eng. J. 140 (2008) 398–413. doi:10.1016/j.cej.2007.11.015.

[16] S. Sánchez-Delgado, C. Marugán-Cruz, A. Soria-Verdugo, D. Santana,

Estimation and experimental validation of the circulation time in a 2D gas–solid fluidized beds, Powder Technol. 235 (2013) 669–676. doi:10.1016/j.powtec.2012.11.012.

[17] D. Geldart, The size and frequency of bubbles in two- and three-dimensional gas-fluidised beds, Powder Technol. 4 (1970) 41–55. doi:10.1016/0032-5910(70)80007-9.

[18] J. Werther, O. Molerus, The local structure of gas fluidized beds —I. A statistically based measuring system, Int. J. Multiph. Flow. 1 (1973) 103–122. doi:10.1016/0301-9322(73)90007-4.

[19] P.N. Rowe, H. Masson, Fluidised bed bubbles observed simultaneously by probe and by X-rays, Chem. Eng. Sci. 35 (1980) 1443–1447. doi:10.1016/0009-2509(80)85138-4.

[20] D.J. Gunn, H.H. Al-Doori, The measurement of bubble flows in fluidized beds by electrical probe, Int. J. Multiph. Flow. 11 (1985) 535–551. doi:10.1016/0301-9322(85)90074-6.

[21] C.E.J. van Lare, H.W. Piepers, J.N. Schoonderbeek, D. Thoenes, Investigation on bubble characteristics in a gas fluidized bed, Chem. Eng. Sci. 52 (1997) 829–841. doi:10.1016/S0009-2509(96)00442-3.

[22] E.A. Whitemarsh, D.R. Escudero, T.J. Heindel, Probe effects on the local gas holdup conditions in a fluidized bed, Powder Technol. 294 (2016) 191–201. doi:10.1016/j.powtec.2016.02.035.

[23] G.A. Bokkers, M. van Sint Annaland, J.A.M. Kuipers, Mixing and segregation in a bidisperse gas–solid fluidised bed: a numerical and experimental study,

Powder Technol. 140 (2004) 176–186. doi:10.1016/j.powtec.2004.01.018.

[24] Y. Zhang, B. Jin, W. Zhong, Experimental investigation on mixing and segregation behavior of biomass particle in fluidized bed, Chem. Eng. Process. Process Intensif. 48 (2009) 745–754. doi:10.1016/j.cep.2008.09.004.

[25] W. Bai, N.K.G. Keller, T.J. Heindel, R.O. Fox, Numerical study of mixing and segregation in a biomass fluidized bed, Powder Technol. 237 (2013) 355–366. doi:10.1016/j.powtec.2012.12.018.

[26] O.O. Olaofe, K.A. Buist, N.G. Deen, M.A. van der Hoef, J.A.M. Kuipers, Segregation dynamics in dense polydisperse gas-fluidized beds, Powder Technol. 246 (2013) 695–706. doi:10.1016/j.powtec.2013.05.047.

[27] Z. Peng, E. Doroodchi, Y. Alghamdi, B. Moghtaderi, Mixing and segregation of solid mixtures in bubbling fluidized beds under conditions pertinent to the fuel reactor of a chemical looping system, Powder Technol. 235 (2013) 823–837. doi:10.1016/j.powtec.2012.11.047.

[28] O.O. Olaofe, A. V. Patil, N.G. Deen, M.A. van der Hoef, J.A.M. Kuipers, Simulation of particle mixing and segregation in bidisperse gas fluidized beds, Chem. Eng. Sci. 108 (2014) 258–269. doi:10.1016/j.ces.2014.01.009.

[29] E. Sette, D. Pallarès, F. Johnsson, Experimental quantification of lateral mixing of fuels in fluid-dynamically down-scaled bubbling fluidized beds, Appl. Energy. 136 (2014) 671–681. doi:10.1016/j.apenergy.2014.09.075.

[30] P.N. Rowe, A.W. Nienow, Particle mixing and segregation in gas fluidised beds. A review, Powder Technol. 15 (1976) 141–147. doi:10.1016/0032-5910(76)80042-3.

[31] S. Cooper, C.J. Coronella, CFD simulations of particle mixing in a binary fluidized bed, Powder Technol. 151 (2005) 27–36. doi:10.1016/j.powtec.2004.11.041.

[32] B.G.M. van Wachem, J. van der Schaaf, J.C. Schouten, R. Krishna, C.M. van den Bleek, Experimental validation of Lagrangian–Eulerian simulations of fluidized beds, Powder Technol. 116 (2001) 155–165. doi:10.1016/S0032-5910(00)00389-2.

[33] I. Hulme, E. Clavelle, L. van der Lee, A. Kantzas, CFD Modeling and Validation of Bubble Properties for a Bubbling Fluidized Bed, Ind. Eng. Chem. Res. 44 (2005) 4254–4266. doi:10.1021/ie049837j.

[34] A. Acosta-Iborra, C. Sobrino, F. Hernández-Jiménez, M. de Vega, Experimental and computational study on the bubble behavior in a 3-D fluidized bed, Chem. Eng. Sci. 66 (2011) 3499–3512. doi:10.1016/j.ces.2011.04.009.

[35] F. Alobaid, B. Epple, Improvement, validation and application of CFD/DEM model to dense gas–solid flow in a fluidized bed, Particuology. 11 (2013) 514–526. doi:10.1016/j.partic.2012.05.008.

[36] M.A. van der Hoef, M. van Sint Annaland, N.G. Deen, J.A.M. Kuipers, Numerical Simulation of Dense Gas-Solid Fluidized Beds: A Multiscale Modeling Strategy, Annu. Rev. Fluid Mech. 40 (2008) 47–70. doi:10.1146/annurev.fluid.40.111406.102130.

[37] P.A. Cundall, O.D.L. Strack, A discrete numerical model for granular assemblies, Géotechnique. 29 (1979) 47–65. doi:10.1680/geot.1979.29.1.47.

[38] C.R. Müller, D.J. Holland, a. J. Sederman, S. a. Scott, J.S. Dennis, L.F.

Gladden, Granular temperature: Comparison of Magnetic Resonance measurements with Discrete Element Model simulations, Powder Technol. 184 (2008) 241–253. doi:10.1016/j.powtec.2007.11.046.

[39] S. Ergun, Fluid flow through packed columns, Chem. Eng. Prog. 48 (1952) 89–94.

[40] C.Y. Wen, Mechanics of fluidization, in: Chem. Eng. Prog. Symp. Ser., 1966: pp. 100–101.

[41] M. Syamlal, T. O'Brien, The Derivation of a Drag Coefficient Formula from Velocity-Voidage Correlations, Tech. Note,US Dep. Energy, Off. Foss. Energy, NETL,Morgantown, WV. (1987). https://www.researchgate.net/profile/Madhava_Syamlal/publication/242419434_The_Derivation_of_a_Drag_Coefficient_Formula_from_Velocity-Voidage_Correlations/links/00b7d52fa545283c82000000/The-Derivation-of-a-Drag-Coefficient-Formula-from-Velocity-Voidage-Co.

[42] J. Ding, D. Gidaspow, A bubbling fluidization model using kinetic theory of granular flow, AIChE J. 36 (1990) 523–538. doi:10.1002/aic.690360404.

[43] R. Beetstra, M.A. van der Hoef, J.A.M. Kuipers, Numerical study of segregation using a new drag force correlation for polydisperse systems derived from lattice-Boltzmann simulations, Chem. Eng. Sci. 62 (2007) 246–255. doi:10.1016/j.ces.2006.08.054.

[44] O.O. Ayeni, C.L. Wu, K. Nandakumar, J.B. Joshi, Development and validation of a new drag law using mechanical energy balance approach for DEM–CFD simulation of gas–solid fluidized bed, Chem. Eng. J. 302 (2016) 395–405. doi:10.1016/j.cej.2016.05.056.

[45] B.G.M. van Wachem, J.C. Schouten, C.M. van den Bleek, R. Krishna, J.L. Sinclair, Comparative analysis of CFD models of dense gas–solid systems, AIChE J. 47 (2001) 1035–1051. doi:10.1002/aic.690470510.

[46] W. Du, X. Bao, J. Xu, W. Wei, Computational fluid dynamics (CFD) modeling of spouted bed: Assessment of drag coefficient correlations, Chem. Eng. Sci. 61 (2006) 1401–1420. doi:10.1016/j.ces.2005.08.013.

[47] E. Esmaili, N. Mahinpey, Adjustment of drag coefficient correlations in three dimensional CFD simulation of gas–solid bubbling fluidized bed, Adv. Eng. Softw. 42 (2011) 375–386. doi:10.1016/j.advengsoft.2011.03.005.

[48] X. Ku, T. Li, T. Løvås, Influence of drag force correlations on periodic fluidization behavior in Eulerian–Lagrangian simulation of a bubbling fluidized bed, Chem. Eng. Sci. 95 (2013) 94–106. doi:10.1016/j.ces.2013.03.038.

[49] N. V. Koralkar, M. Bose, Performance of drag models for simulation of fluidized beds with Geldart D particles, Adv. Powder Technol. 27 (2016) 2377–2398. doi:10.1016/j.apt.2016.11.008.

[50] M. Lungu, H. Wang, J. Wang, Y. Yang, F. Chen, Two-Fluid Model Simulations of the National Energy Technology Laboratory Bubbling Fluidized Bed Challenge Problem, Ind. Eng. Chem. Res. 55 (2016) 5063–5077. doi:10.1021/acs.iecr.5b04511.

[51] J. Li, J.A.M. Kuipers, Gas-particle interactions in dense gas-fluidized beds, Chem. Eng. Sci. 58 (2003) 711–718. doi:10.1016/S0009-2509(02)00599-7.

[52] I. Hulme, A. Kantzas, Determination of bubble diameter and axial velocity for a polyethylene fluidized bed using X-ray fluoroscopy, Powder Technol. 147

(2004) 20–33. doi:10.1016/j.powtec.2004.08.008.

[53] D.J. Holland, Q. Marashdeh, C.R. Müller, F. Wang, J.S. Dennis, L.-S. Fan, L.F. Gladden, Comparison of ECVT and MR Measurements of Voidage in a Gas-Fluidized Bed, Ind. Eng. Chem. Res. 48 (2009) 172–181. doi:10.1021/ie8002073.

[54] T.W. Asegehegn, M. Schreiber, H.J. Krautz, Investigation of bubble behavior in fluidized beds with and without immersed horizontal tubes using a digital image analysis technique, Powder Technol. 210 (2011) 248–260. doi:10.1016/j.powtec.2011.03.025.

[55] J.M. Weber, J.S. Mei, Bubbling fluidized bed characterization using Electrical Capacitance Volume Tomography (ECVT), Powder Technol. 242 (2013) 40–50. doi:10.1016/j.powtec.2013.01.044.

[56] B. Gopalan, M. Shahnam, R. Panday, J. Tucker, F. Shaffer, L. Shadle, J. Mei, W. Rogers, C. Guenther, M. Syamlal, Measurements of pressure drop and particle velocity in a pseudo 2-D rectangular bed with Geldart Group D particles, Powder Technol. 291 (2016) 299–310. doi:10.1016/j.powtec.2015.12.040.

[57] A.N. Chandran, S.S. Rao, Y.B.G. Varma, Fluidized bed drying of solids, AIChE J. 36 (1990) 29–38. doi:10.1002/aic.690360106.

[58] T.E. Broadhurst, H.A. Becker, Onset of fluidization and slugging in beds of uniform particles, AIChE J. 21 (1975) 238–247. doi:10.1002/aic.690210204.

[59] W.-C. Yang, Bubbling fluidized beds, in: Handb. Fluid. Fluid-Particle Syst., CRC Press, 2003: pp. 64–123.

[60] J.R. Grace, Contacting modes and behaviour classification of gas—solid and other two-phase suspensions, Can. J. Chem. Eng. 64 (1986) 353–363.

[61] A. Svensson, F. Johnsson, B. Leckner, Fluidization regimes in non-slugging fluidized beds: the influence of pressure drop across the air distributor, Powder Technol. 86 (1996) 299–312. doi:10.1016/0032-5910(95)03055-7.

[62] D. Bai, E. Shibuya, N. Nakagawa, K. Kato, Characterization of gas fluidization regimes using pressure fluctuations, Powder Technol. 87 (1996) 105–111. doi:10.1016/0032-5910(95)03072-7.

[63] Y.T. Makkawi, P.C. Wright, Fluidization regimes in a conventional fluidized bed characterized by means of electrical capacitance tomography, Chem. Eng. Sci. 57 (2002) 2411–2437. doi:10.1016/S0009-2509(02)00138-0.

[64] K.. Lim, J.. Zhu, J.. Grace, Hydrodynamics of gas-solid fluidization, Int. J. Multiph. Flow. 21 (1995) 141–193. doi:10.1016/0301-9322(95)00038-Y.

[65] D. Geldart, Types of gas fluidization, Powder Technol. 7 (1973) 285–292. doi:10.1016/0032-5910(73)80037-3.

[66] D. Kunii, O. Levenspiel, Fluidization engineering, Elsevier, 2013.

[67] K. Dubrawski, S. Tebianian, H.T. Bi, J. Chaouki, N. Ellis, R. Gerspacher, R. Jafari, A. Kantzas, C. Lim, G.S. Patience, T. Pugsley, M.Z. Qi, J.X. Zhu, J.R. Grace, Traveling column for comparison of invasive and non-invasive fluidization voidage measurement techniques, Powder Technol. 235 (2013) 203–220. doi:10.1016/j.powtec.2012.10.031.

[68] J.R. van Ommen, R.F. Mudde, Measuring the Gas-Solids Distribution in Fluidized Beds -- A Review, Int. J. Chem. React. Eng. 6 (2008).

doi:10.2202/1542-6580.1796.

[69] J. Sun, Y. Yan, Non-intrusive measurement and hydrodynamics characterization of gas–solid fluidized beds: a review, Meas. Sci. Technol. 27 (2016) 112001. doi:10.1088/0957-0233/27/11/112001.

[70] D. Wilkinson, Determination of minimum fluidization velocity by pressure fluctuation measurement, Can. J. Chem. Eng. 73 (1995) 562–565. doi:10.1002/cjce.5450730416.

[71] C.A.S. Felipe, S.C.S. Rocha, Prediction of minimum fluidization velocity of gas–solid fluidized beds by pressure fluctuation measurements — Analysis of the standard deviation methodology, Powder Technol. 174 (2007) 104–113. doi:10.1016/j.powtec.2007.01.015.

[72] D. Escudero, T.J. Heindel, Bed height and material density effects on fluidized bed hydrodynamics, Chem. Eng. Sci. 66 (2011) 3648–3655. doi:10.1016/j.ces.2011.04.036.

[73] J. van der Schaaf, J.C. Schouten, C.M. van den Bleek, Origin, propagation and attenuation of pressure waves in gas—solid fluidized beds, Powder Technol. 95 (1998) 220–233. doi:10.1016/S0032-5910(97)03341-X.

[74] J. van der Schaaf, J.C. Schouten, F. Johnsson, C.M. van den Bleek, Non-intrusive determination of bubble and slug length scales in fluidized beds by decomposition of the power spectral density of pressure time series, Int. J. Multiph. Flow. 28 (2002) 865–880. doi:10.1016/S0301-9322(01)00090-8.

[75] M. Liu, Y. Zhang, H. Bi, J.R. Grace, Y. Zhu, Non-intrusive determination of bubble size in a gas–solid fluidized bed: An evaluation, Chem. Eng. Sci. 65

(2010) 3485–3493. doi:10.1016/j.ces.2010.02.049.

[76] D. Geldart, J. Baeyens, The design of distributors for gas-fluidized beds, Powder Technol. 42 (1985) 67–78. doi:10.1016/0032-5910(85)80039-5.

[77] X. Fan, Z. Yang, D.J. Parker, B. Armstrong, Prediction of bubble behaviour in fluidised beds based on solid motion and flow structure, Chem. Eng. J. 140 (2008) 358–369. doi:10.1016/j.cej.2007.10.013.

[78] J.A. Laverman, I. Roghair, M. van S. Annaland, H. Kuipers, Investigation into the hydrodynamics of gas–solid fluidized beds using particle image velocimetry coupled with digital image analysis, Can. J. Chem. Eng. 86 (2008) 523–535. doi:10.1002/cjce.20054.

[79] T.C. Chandrasekera, A. Wang, D.J. Holland, Q. Marashdeh, M. Pore, F. Wang, A.J. Sederman, L.S. Fan, L.F. Gladden, J.S. Dennis, A comparison of magnetic resonance imaging and electrical capacitance tomography: An air jet through a bed of particles, Powder Technol. 227 (2012) 86–95. doi:10.1016/j.powtec.2012.03.005.

[80] C. Rautenbach, R.F. Mudde, X. Yang, M.C. Melaaen, B.M. Halvorsen, A comparative study between electrical capacitance tomography and time-resolved X-ray tomography, Flow Meas. Instrum. 30 (2013) 34–44. doi:10.1016/j.flowmeasinst.2012.11.005.

[81] Y. Tsuji, T. Kawaguchi, T. Tanaka, Discrete particle simulation of two-dimensional fluidized bed, Powder Technol. 77 (1993) 79–87. doi:10.1016/0032-5910(93)85010-7.

[82] B.P.B. Hoomans, J.A.M. Kuipers, W.J. Briels, W.P.M. van Swaaij, Discrete

particle simulation of bubble and slug formation in a two-dimensional gas-fluidised bed: A hard-sphere approach, Chem. Eng. Sci. 51 (1996) 99–118. doi:10.1016/0009-2509(95)00271-5.

[83] J.J. Nieuwland, Hydrodynamic Modelling of Gas-Solid Two-Phase Flows, University of Twente, 1995.

[84] C.R. Müller, S.A. Scott, D.J. Holland, B.C. Clarke, A.J. Sederman, J.S. Dennis, L.F. Gladden, Validation of a discrete element model using magnetic resonance measurements, Particuology. 7 (2009) 297–306. doi:10.1016/j.partic.2009.04.002.

[85] H.R. Norouzi, N. Mostoufi, Z. Mansourpour, R. Sotudeh-Gharebagh, J. Chaouki, Characterization of solids mixing patterns in bubbling fluidized beds, Chem. Eng. Res. Des. 89 (2011) 817–826. doi:10.1016/j.cherd.2010.10.014.

[86] M. Karimi, N. Mostoufi, R. Zarghami, R. Sotudeh-Gharebagh, A new method for validation of a CFD–DEM model of gas–solid fluidized bed, Int. J. Multiph. Flow. 47 (2012) 133–140. doi:10.1016/j.ijmultiphaseflow.2012.07.009.

[87] H.A. Elghannay, D.K. Tafti, DEM Predictions of NETL Small Scale Challenge Problem, in: ASME 2014 4th Jt. US-European Fluids Eng. Div. Summer Meet. Collocated with ASME 2014 12th Int. Conf. Nanochannels, Microchannels, Minichannels, Am. Soc. Mech. Eng., 2014: p. V01CT23A001. doi:10.1115/FEDSM2014-21032.

[88] D. Tafti, Genidlest a parallel high performance computational infrastructure for simulating complex turbulent flow and heat transfer, in: APS Div. Fluid Dyn. Meet. Abstr., 2002.

[89] Z. Peng, E. Doroodchi, C. Luo, B. Moghtaderi, Influence of void fraction calculation on fidelity of CFD-DEM simulation of gas-solid bubbling fluidized beds, AIChE J. 60 (2014) 2000–2018. doi:10.1002/aic.14421.

[90] A. Busciglio, G. Vella, G. Micale, L. Rizzuti, Analysis of the bubbling behaviour of 2D gas solid fluidized beds: Part II. Comparison between experiments and numerical simulations via Digital Image Analysis Technique, Chem. Eng. J. 148 (2009) 145–163. doi:10.1016/j.cej.2008.11.010.

[91] F. Hernández-Jiménez, S. Sánchez-Delgado, A. Gómez-García, A. Acosta-Iborra, Comparison between two-fluid model simulations and particle image analysis & velocimetry (PIV) results for a two-dimensional gas–solid fluidized bed, Chem. Eng. Sci. 66 (2011) 3753–3772. doi:10.1016/j.ces.2011.04.026.

[92] V. Verma, J.T. Padding, N.G. Deen, J.A.M.H. Kuipers, F. Barthel, M. Bieberle, M. Wagner, U. Hampel, Bubble dynamics in a 3-D gas-solid fluidized bed using ultrafast electron beam X-ray tomography and two-fluid model, AIChE J. 60 (2014) 1632–1644. doi:10.1002/aic.14393.

[93] N. Almohammed, F. Alobaid, M. Breuer, B. Epple, A comparative study on the influence of the gas flow rate on the hydrodynamics of a gas–solid spouted fluidized bed using Euler–Euler and Euler–Lagrange/DEM models, Powder Technol. 264 (2014) 343–364. doi:10.1016/j.powtec.2014.05.024.

[94] R. Garg, J. Galvin, T. Li, S. Pannala, Documentation of open-source MFIX – DEM software for gas-solids, (2012). https://mfix.netl.doe.gov/download/mfix/mfix_current_documentation/dem_doc_2012-1.pdf.

[95] R. Garg, J. Galvin, T. Li, S. Pannala, Open-source MFIX-DEM software for

gas–solids flows: Part I—Verification studies, Powder Technol. 220 (2012) 122–137. doi:10.1016/j.powtec.2011.09.019.

[96] T. Li, R. Garg, J. Galvin, S. Pannala, Open-source MFIX-DEM software for gas-solids flows: Part II — Validation studies, Powder Technol. 220 (2012) 138–150. doi:10.1016/j.powtec.2011.09.020.

[97] T. Li, P. Gopalakrishnan, R. Garg, M. Shahnam, CFD–DEM study of effect of bed thickness for bubbling fluidized beds, Particuology. 10 (2012) 532–541. doi:10.1016/j.partic.2012.02.006.

[98] F. Dioguardi, P. Dellino, D. Mele, Integration of a new shape-dependent particle–fluid drag coefficient law in the multiphase Eulerian–Lagrangian code MFIX-DEM, Powder Technol. 260 (2014) 68–77. doi:10.1016/j.powtec.2014.03.071.

[99] F. Hernández-Jiménez, T. Li, E. Cano-Pleite, W. Rogers, A. Acosta-Iborra, Characterization of the particle–wall frictional forces in pseudo-2D fluidized beds using DEM, Chem. Eng. Sci. 116 (2014) 136–143. doi:10.1016/j.ces.2014.04.033.

[100] K. Luo, F. Wu, S. Yang, J. Fan, CFD–DEM study of mixing and dispersion behaviors of solid phase in a bubbling fluidized bed, Powder Technol. 274 (2015) 482–493. doi:10.1016/j.powtec.2015.01.046.

[101] Z. Mansourpour, S. Karimi, R. Zarghami, N. Mostoufi, R. Sotudeh-Gharebagh, Insights in hydrodynamics of bubbling fluidized beds at elevated pressure by DEM–CFD approach, Particuology. 8 (2010) 407–414. doi:10.1016/j.partic.2010.03.017.

[102] B.H. Xu, A.B. Yu, Numerical simulation of the gas-solid flow in a fluidized bed by combining discrete particle method with computational fluid dynamics, Chem. Eng. Sci. 52 (1997) 2785–2809. doi:10.1016/S0009-2509(97)00081-X.

[103] D.S. Boyalakuntla, Simulation of granular and gas–solid flows using Discrete Element Method, Carnegie Mellon University, PhD thesis, 2003.

[104] A. Zaltzman, R. Feller, A. Mizrach, Z. Schmilovitch, Separating Potatoes from Clods and Stones in a Fluidized Bed Medium, Trans. ASAE. 26 (1983) 0987–0990. doi:10.13031/2013.34061.

[105] P. Salatino, R. Solimene, Mixing and segregation in fluidized bed thermochemical conversion of biomass, Powder Technol. 316 (2017) 29–40. doi:10.1016/j.powtec.2016.11.058.

[106] B. Paudel, Z.-G. Feng, Prediction of minimum fluidization velocity for binary mixtures of biomass and inert particles, Powder Technol. 237 (2013) 134–140. doi:10.1016/j.powtec.2013.01.031.

[107] T. R. Rao, J.. Ram. Bheemarasetti, Minimum fluidization velocities of mixtures of biomass and sands, Energy. 26 (2001) 633–644. doi:10.1016/S0360-5442(01)00014-7.

[108] C. Si, Q. Guo, Fluidization Characteristics of Binary Mixtures of Biomass and Quartz Sand in an Acoustic Fluidized Bed, Ind. Eng. Chem. Res. 47 (2008) 9773–9782. doi:10.1021/ie801070z.

[109] T.J.P. Oliveira, C.R. Cardoso, C.H. Ataíde, Bubbling fluidization of biomass and sand binary mixtures: Minimum fluidization velocity and particle segregation, Chem. Eng. Process. Process Intensif. 72 (2013) 113–121.

doi:10.1016/j.cep.2013.06.010.

[110] A.C. Hoffmann, L.P.B.M. Janssen, J. Prins, Particle segregation in fluidised binary mixtures, Chem. Eng. Sci. 48 (1993) 1583–1592. doi:10.1016/0009-2509(93)80118-A.

[111] S.Y. Wu, J. Baeyens, Segregation by size difference in gas fluidized beds, Powder Technol. 98 (1998) 139–150. doi:10.1016/S0032-5910(98)00026-6.

[112] A. Marzocchella, P. Salatino, V. Di Pastena, L. Lirer, Transient fluidization and segregation of binary mixtures of particles, AIChE J. 46 (2000) 2175–2182. doi:10.1002/aic.690461110.

[113] M.J.V. Goldschmidt, J.M. Link, S. Mellema, J.A.M. Kuipers, Digital image analysis measurements of bed expansion and segregation dynamics in dense gas-fluidised beds, Powder Technol. 138 (2003) 135–159. doi:10.1016/j.powtec.2003.09.003.

[114] J. Huang, Y. Lu, H. Wang, A new quantitative measurement method for mixing and segregation of binary-mixture fluidized bed by capacitance probe, Chem. Eng. J. 326 (2017) 99–108. doi:10.1016/j.cej.2017.05.126.

[115] R. Girimonte, B. Formisani, V. Vivacqua, The relationship between fluidization velocity and segregation in two-component gas fluidized beds: Density- or size-segregating mixtures, Chem. Eng. J. 335 (2018) 63–73. doi:10.1016/j.cej.2017.10.135.

[116] R.J. Hill, D.L. Koch, A.J.C. Ladd, The first effects of fluid inertia on flows in ordered and random arrays of spheres, J. Fluid Mech. 448 (2001) 213–241. doi:10.1017/S0022112001005948.

[117] R.J. Hill, D.L. Koch, A.J.C. Ladd, Moderate-Reynolds-number flows in ordered and random arrays of spheres, J. Fluid Mech. 448 (2001) 243–278. doi:10.1017/S0022112001005936.

[118] L. Huilin, Z. Yunhua, J. Ding, D. Gidaspow, L. Wei, Investigation of mixing/segregation of mixture particles in gas–solid fluidized beds, Chem. Eng. Sci. 62 (2007) 301–317. doi:10.1016/j.ces.2006.08.031.

[119] R. Fan, R.O. Fox, Segregation in polydisperse fluidized beds: Validation of a multi-fluid model, Chem. Eng. Sci. 63 (2008) 272–285. doi:10.1016/j.ces.2007.09.038.

[120] S.R. Dahl, C.M. Hrenya, Size segregation in gas–solid fluidized beds with continuous size distributions, Chem. Eng. Sci. 60 (2005) 6658–6673. doi:10.1016/j.ces.2005.05.057.

[121] A. Di Renzo, F.P. Di Maio, R. Girimonte, B. Formisani, DEM simulation of the mixing equilibrium in fluidized beds of two solids differing in density, Powder Technol. 184 (2008) 214–223. doi:10.1016/j.powtec.2007.11.031.

[122] F. Fotovat, A. Abbasi, R.J. Spiteri, H. de Lasa, J. Chaouki, A CPFD model for a bubbly biomass–sand fluidized bed, Powder Technol. 275 (2015) 39–50. doi:10.1016/j.powtec.2015.01.005.

[123] L. Shen, J. Xiao, F. Niklasson, F. Johnsson, Biomass mixing in a fluidized bed biomass gasifier for hydrogen production, Chem. Eng. Sci. 62 (2007) 636–643. doi:10.1016/j.ces.2006.09.033.

[124] A.W. Laputz, Particle mixing and segregation in a conical fluidized bed., University of Nevada, 2000.

[125] B. Formisani, G.D. Cristofaro, R. Girimonte, A fundamental approach to the phenomenology of fluidization of size segregating binary mixtures of solids, Chem. Eng. Sci. 56 (2001) 109–119. doi:10.1016/S0009-2509(00)00426-7.

[126] L. Huilin, H. Yurong, D. Gidaspow, Y. Lidan, Q. Yukun, Size segregation of binary mixture of solids in bubbling fluidized beds, Powder Technol. 134 (2003) 86–97. doi:10.1016/S0032-5910(03)00126-8.

[127] P.U. Foscolo, L.G. Gibilaro, S.P. Waldram, A unified model for particulate expansion of fluidised beds and flow in fixed porous media, Chem. Eng. Sci. 38 (1983) 1251–1260. doi:10.1016/0009-2509(83)80045-1.

[128] L.G. Gibilaro, R. Di Felice, S.P. Waldram, P.U. Foscolo, Generalized friction factor and drag coefficient correlations for fluid-particle interactions, Chem. Eng. Sci. 40 (1985) 1817–1823. doi:10.1016/0009-2509(85)80116-0.

[129] R. Di Felice, The voidage function for fluid-particle interaction systems, Int. J. Multiph. Flow. 20 (1994) 153–159. doi:10.1016/0301-9322(94)90011-6.

[130] N. Yang, W. Wang, W. Ge, J. Li, CFD simulation of concurrent-up gas–solid flow in circulating fluidized beds with structure-dependent drag coefficient, Chem. Eng. J. 96 (2003) 71–80. doi:10.1016/j.cej.2003.08.006.

[131] K. Agrawal, P.N. Loezos, M. Syamlal, S. Sundaresan, The role of meso-scale structures in rapid gas–solid flows, J. Fluid Mech. 445 (2001) 151–185. doi:10.1017/S0022112001005663.

[132] A.T. Andrews IV, P.N. Loezos, S. Sundaresan, Coarse-Grid Simulation of Gas-Particle Flows in Vertical Risers, Ind. Eng. Chem. Res. 44 (2005) 6022–6037. doi:10.1021/ie0492193.

[133] Y. Igci, A.T. Andrews IV, S. Sundaresan, S. Pannala, T. O'Brien, Filtered two-fluid models for fluidized gas-particle suspensions, AIChE J. 54 (2008) 1431–1448. doi:10.1002/aic.11481.

[134] S. Tenneti, R. Garg, C.M. Hrenya, R.O. Fox, S. Subramaniam, Direct numerical simulation of gas–solid suspensions at moderate Reynolds number: Quantifying the coupling between hydrodynamic forces and particle velocity fluctuations, Powder Technol. 203 (2010) 57–69. doi:10.1016/j.powtec.2010.03.042.

[135] S. Tenneti, R. Garg, S. Subramaniam, Drag law for monodisperse gas–solid systems using particle-resolved direct numerical simulation of flow past fixed assemblies of spheres, Int. J. Multiph. Flow. 37 (2011) 1072–1092. doi:10.1016/j.ijmultiphaseflow.2011.05.010.

[136] X. Gao, C. Wu, Y. Cheng, L. Wang, X. Li, Experimental and numerical investigation of solid behavior in a gas–solid turbulent fluidized bed, Powder Technol. 228 (2012) 1–13. doi:10.1016/j.powtec.2012.04.025.

[137] C. Loha, H. Chattopadhyay, P.K. Chatterjee, Assessment of drag models in simulating bubbling fluidized bed hydrodynamics, Chem. Eng. Sci. 75 (2012) 400–407. doi:10.1016/j.ces.2012.03.044.

[138] B. Estejab, F. Battaglia, Assessment of Drag Models for Geldart A Particles in Bubbling Fluidized Beds, J. Fluids Eng. 138 (2016) 031105. doi:10.1115/1.4031490.

[139] E. Ghadirian, H. Arastoopour, CFD simulation of a fluidized bed using the EMMS approach for the gas-solid drag force, Powder Technol. 288 (2016) 35–44. doi:10.1016/j.powtec.2015.10.034.

[140] Y.Q. Feng, A.B. Yu, Assessment of Model Formulations in the Discrete Particle Simulation of Gas−Solid Flow, Ind. Eng. Chem. Res. 43 (2004) 8378–8390. doi:10.1021/ie049387v.

[141] F. Vejahati, N. Mahinpey, N. Ellis, M.B. Nikoo, CFD simulation of gas-solid bubbling fluidized bed: A new method for adjusting drag law, Can. J. Chem. Eng. 87 (2009) 19–30. doi:10.1002/cjce.20139.

[142] S. Benzarti, H. Mhiri, H. Bournot, Drag models for Simulation Gas-Solid Flow in the Bubbling Fluidized Bed of FCC Particles, World Acad. Sci. Eng. Technol. 6 (2012) 1138–1143. http://www.waset.org/publications/12716.

[143] A. Di Renzo, F. Cello, F.P. Di Maio, Simulation of the layer inversion phenomenon in binary liquid--fluidized beds by DEM–CFD with a drag law for polydisperse systems, Chem. Eng. Sci. 66 (2011) 2945–2958. doi:10.1016/j.ces.2011.03.035.

[144] Y. Zhang, Y. Zhao, L. Lu, W. Ge, J. Wang, C. Duan, Assessment of polydisperse drag models for the size segregation in a bubbling fluidized bed using discrete particle method, Chem. Eng. Sci. 160 (2017) 106–112. doi:10.1016/j.ces.2016.11.028.

[145] J.A.H. De Jong, J.F. Nomden, Homogeneous gas—solid fluidization, Powder Technol. 9 (1974) 91–97. doi:10.1016/0032-5910(74)85012-6.

[146] O. Molerus, Interpretation of Geldart's type A, B, C and D powders by taking into account interparticle cohesion forces, Powder Technol. 33 (1982) 81–87. doi:10.1016/0032-5910(82)85041-9.

[147] D. Geldart, N. Harnby, A.C. Wong, Fluidization of cohesive powders, Powder

Technol. 37 (1984) 25–37. doi:10.1016/0032-5910(84)80003-0.

[148] M.J. Rhodes, X.S. Wang, M. Nguyen, P. Stewart, K. Liffman, Use of discrete element method simulation in studying fluidization characteristics: influence of interparticle force, Chem. Eng. Sci. 56 (2001) 69–76. doi:10.1016/S0009-2509(00)00427-9.

[149] M. Ye, M.. van der Hoef, J.A.. Kuipers, A numerical study of fluidization behavior of Geldart A particles using a discrete particle model, Powder Technol. 139 (2004) 129–139. doi:10.1016/j.powtec.2003.10.012.

[150] J.B. Joshi, Solid-liquid fluidised beds: some design aspects., Chem. Eng. Res. Des. 61 (1983) 143–161. https://www.scopus.com/inward/record.uri?eid=2-s2.0-0020752625&partnerID=40&md5=482cfed8ee25228c1f1f947d56cdee1b.

[151] A.B. Pandit, J.B. Joshi, Pressure drop in fixed, expanded and fluidized beds, packed column and static mixers - A unified approach, Rev. Chem. Eng. 14 (1998) 321–371. doi:10.1515/REVCE.1998.14.4-5.321.

[152] W.L. McCabe, J.C. Smith, P. Harriott, Unit operations of chemical engineering, 1976.

[153] G.G. Stokes, On the Effect of the Internal Friction of Fluids on the Motion of Pendulums, in: Math. Phys. Pap., Cambridge University Press, Cambridge, 1905: pp. 1–10. doi:10.1017/CBO9780511702266.002.

[154] A.R. Khan, J.F. Richardson, The Resistance to Motion of a Solid Sphere in a Fluid, Chem. Eng. Commun. 62 (1987) 135–150. doi:10.1080/00986448708912056.

[155] L. Schiller, A.Z. Nauman, No Title, Ver. Deut. Ins. 77 (1933) 318.

[156] J.M. DallaValle, Micromeritics, the technology of fine particles, 2d ed., Pitman Pub. Corp., New York, 1948.

[157] M. Syamlal, T.J. O'Brien, Fluid dynamic simulation of O3 decomposition in a bubbling fluidized bed, AIChE J. 49 (2003) 2793–2801. doi:10.1002/aic.690491112.

[158] M.T. Shah, R.P. Utikar, M.O. Tade, V.K. Pareek, G.M. Evans, Verification of EMMS formulation using lattice Boltzmann simulations, Powder Technol. 257 (2014) 30–39. doi:10.1016/j.powtec.2014.02.038.

[159] S. Limtrakul, A. Chalermwattanatai, K. Unggurawirote, Y. Tsuji, T. Kawaguchi, W. Tanthapanichakoon, Discrete particle simulation of solids motion in a gas–solid fluidized bed, Chem. Eng. Sci. 58 (2003) 915–921. doi:10.1016/S0009-2509(02)00625-5.

[160] Y. Zhang, B. Jin, W. Zhong, Fluidization, Mixing and Segregation of a Biomass-Sand Mixture in a Fluidized Bed, Int. J. Chem. React. Eng. 6 (2008). doi:10.2202/1542-6580.1809.

[161] Y.Q. Feng, A.B. Yu, Microdynamic modelling and analysis of the mixing and segregation of binary mixtures of particles in gas fluidization, Chem. Eng. Sci. 62 (2007) 256–268. doi:10.1016/j.ces.2006.08.015.

[162] S. Gorji-Kandi, S.M. Alavi-Amleshi, N. Mostoufi, A solids mixing rate correlation for small scale fluidized beds, Particuology. 21 (2015) 55–64. doi:10.1016/j.partic.2014.10.003.

[163] M.J. Rhodes, X.. Wang, M. Nguyen, P. Stewart, K. Liffman, Study of mixing

in gas-fluidized beds using a DEM model, Chem. Eng. Sci. 56 (2001) 2859–2866. doi:10.1016/S0009-2509(00)00524-8.

[164] J. Sánchez-Prieto, F. Hernández-Jiménez, L.M. Garcia-Gutierrez, A. Soria-Verdugo, Experimental study on the characteristic mixing time of solids and its link with the lateral dispersion coefficient in bubbling fluidized beds, Chem. Eng. J. 307 (2017) 113–121. doi:10.1016/j.cej.2016.08.075.

[165] N. Mostoufi, J. Chaouki, Local solid mixing in gas–solid fluidized beds, Powder Technol. 114 (2001) 23–31. doi:10.1016/S0032-5910(00)00258-8.

[166] A.W. Nienow, P.N. Rowe, L.Y.-L. Cheung, A quantitative analysis of the mixing of two segregating powders of different density in a gas-fluidised bed, Powder Technol. 20 (1978) 89–97. doi:10.1016/0032-5910(78)80013-8.

[167] R.W. Rice, J.F. Brainovich, Mixing/segregation in two- and three-dimensional fluidized beds: Binary systems of equidensity spherical particles, AIChE J. 32 (1986) 7–16. doi:10.1002/aic.690320103.

[168] T. McKeen, T. Pugsley, Simulation and experimental validation of a freely bubbling bed of FCC catalyst, Powder Technol. 129 (2003) 139–152. doi:10.1016/S0032-5910(02)00294-2.

[169] B. Du, W. Warsito, L.-S. Fan, ECT Studies of Gas−Solid Fluidized Beds of Different Diameters, Ind. Eng. Chem. Res. 44 (2005) 5020–5030. doi:10.1021/ie049025n.

[170] C. Rautenbach, M.C. Melaaen, B.M. Halvorsen, Statistical diagnosis of a gas–solid fluidized bed using Electrical Capacitance Tomography, Int. J. Multiph. Flow. 49 (2013) 70–77. doi:10.1016/j.ijmultiphaseflow.2012.10.002.

[171] T.C. Chandrasekera, Y. Li, D. Moody, M.A. Schnellmann, J.S. Dennis, D.J. Holland, Measurement of bubble sizes in fluidised beds using electrical capacitance tomography, Chem. Eng. Sci. 126 (2015) 679–687. doi:10.1016/j.ces.2015.01.011.

[172] Q. Guo, S. Meng, D. Wang, Y. Zhao, M. Ye, W. Yang, Z. Liu, Investigation of gas-solid bubbling fluidized beds using ECT with a modified Tikhonov regularization technique, AIChE J. (2017). doi:10.1002/aic.15879.

[173] C.G. Xie, S.M. Huang, M.S. Beck, B.S. Hoyle, R. Thorn, C. Lenn, D. Snowden, Electrical capacitance tomography for flow imaging: system model for development of image reconstruction algorithms and design of primary sensors, IEE Proc. G Circuits, Devices Syst. 139 (1992) 89–98. doi:10.1049/ip-g-2.1992.0015.

[174] W.Q. Yang, D.M. Spink, T.A. York, H. McCann, An image-reconstruction algorithm based on Landweber's iteration method for electrical-capacitance tomography, Meas. Sci. Technol. 10 (1999) 1065–1069. doi:10.1088/0957-0233/10/11/315.

[175] A.N. Tikhonov, A. V. Goncharsky, V. V. Stepanov, A.G. Yagola, Numerical Methods for the Solution of Ill-Posed Problems, Springer Netherlands, Dordrecht, 1995. doi:10.1007/978-94-015-8480-7.

[176] L. Peng, H. Merkus, B. Scarlett, Using Regularization Methods for Image Reconstruction of Electrical Capacitance Tomography, Part. Part. Syst. Charact. 17 (2000) 96–104. doi:10.1002/1521-4117(200010)17:3<96::AID-PPSC96>3.0.CO;2-8.

[177] W.Q. Yang, L. Peng, Image reconstruction algorithms for electrical capacitance

tomography, Meas. Sci. Technol. 14 (2003) R1–R13. doi:10.1088/0957-0233/14/1/201.

[178] S. Bangliang, Z. Yiheng, P. Lihui, Y. Danya, Z. Baofen, The use of simultaneous iterative reconstruction technique for electrical capacitance tomography, Chem. Eng. J. 77 (2000) 37–41. doi:10.1016/S1385-8947(99)00134-5.

[179] W. Warsito, L.-S. Fan, Neural network based multi-criterion optimization image reconstruction technique for imaging two- and three-phase flow systems using electrical capacitance tomography, Meas. Sci. Technol. 12 (2001) 2198–2210. doi:10.1088/0957-0233/12/12/323.

[180] Q. Marashdeh, W. Warsito, L.-S. Fan, F.L. Teixeira, A nonlinear image reconstruction technique for ECT using a combined neural network approach, Meas. Sci. Technol. 17 (2006) 2097–2103. doi:10.1088/0957-0233/17/8/007.

[181] Z. Huang, B. Wang, H. Li, Dynamic voidage measurements in a gas solid fluidized bed by electrical capacitance tomography, Chem. Eng. Commun. 190 (2003) 1395–1410. doi:10.1080/00986440302155.

[182] J. Ye, H. Wang, W. Yang, A sparsity reconstruction algorithm for electrical capacitance tomography based on modified Landweber iteration, Meas. Sci. Technol. 25 (2014) 115402. doi:10.1088/0957-0233/25/11/115402.

[183] H. Yan, Y.F. Wang, Y.G. Zhou, Y.H. Sun, 3D ECT reconstruction by an improved Landweber iteration algorithm, Flow Meas. Instrum. 37 (2014) 92–98. doi:10.1016/j.flowmeasinst.2014.03.006.

[184] T.C. Chandrasekera, Y. Li, J.S. Dennis, D.J. Holland, Total variation image

reconstruction for electrical capacitance tomography, in: 2012 IEEE Int. Conf. Imaging Syst. Tech. Proc., IEEE, 2012: pp. 584–589. doi:10.1109/IST.2012.6295573.

[185] Z. Cui, Q. Wang, Q. Xue, W. Fan, L. Zhang, Z. Cao, B. Sun, H. Wang, W. Yang, A review on image reconstruction algorithms for electrical capacitance/resistance tomography, Sens. Rev. 36 (2016) 429–445. doi:10.1108/SR-01-2016-0027.

[186] J.S. Halow, P. Nicoletti, Observations of fluidized bed coalescence using capacitance imaging, Powder Technol. 69 (1992) 255–277. doi:10.1016/0032-5910(92)80017-Q.

[187] J.S. Halow, G.E. Fasching, P. Nicoletti, J.L. Spenik, Observations of a fluidized bed using capacitance imaging, Chem. Eng. Sci. 48 (1993) 643–659. doi:10.1016/0009-2509(93)80133-B.

[188] R.B. White, Using electrical capacitance tomography to monitor gas voids in a packed bed of solids, Meas. Sci. Technol. 13 (2002) 1842–1847. doi:10.1088/0957-0233/13/12/306.

[189] R.B. White, Using Electrical Capacitance Tomography to Investigate Gas Solid Contacting, Can. J. Chem. Eng. 83 (2005) 64–67. doi:10.1002/cjce.5450830111.

[190] W.Q. Yang, S. Liu, Role of tomography in gas/solids flow measurement, Flow Meas. Instrum. 11 (2000) 237–244. doi:10.1016/S0955-5986(00)00023-6.

[191] Y.T. Makkawi, P.C. Wright, Optimization of experiment span and data acquisition rate for reliable electrical capacitance tomography measurement in

fluidization studies a case study, Meas. Sci. Technol. 13 (2002) 1831–1841. doi:10.1088/0957-0233/13/12/305.

[192] Y.T. Makkawi, P.C. Wright, Electrical capacitance tomography for conventional fluidized bed measurements—remarks on the measuring technique, Powder Technol. 148 (2004) 142–157. doi:10.1016/j.powtec.2004.09.006.

[193] J. Ye, H. Wang, W. Yang, Characterization of a multi-plane electrical capacitance tomography sensor with different numbers of electrodes, Meas. Sci. Technol. 27 (2016) 035103. doi:10.1088/0957-0233/27/3/035103.

[194] W. Warsito, Q. Marashdeh, L.S. Fan, 3D and real time electrical capacitance volume-tomography sensor design and image reconstruction, US 8614707 B2, 2013. https://www.google.com/patents/US8614707.

[195] F. Johnsson, R.. Zijerveld, J.. Schouten, C.. van den Bleek, B. Leckner, Characterization of fluidization regimes by time-series analysis of pressure fluctuations, Int. J. Multiph. Flow. 26 (2000) 663–715. doi:10.1016/S0301-9322(99)00028-2.

[196] D. Geldart, The effect of particle size and size distribution on the behaviour of gas-fluidised beds, Powder Technol. 6 (1972) 201–215. doi:10.1016/0032-5910(72)83014-6.

[197] S. Mori, C.Y. Wen, Estimation of bubble diameter in gaseous fluidized beds, AIChE J. 21 (1975) 109–115. doi:10.1002/aic.690210114.

[198] J. Werther, Effect of gas distributor on the hydrodynamics of gas fluidized beds, Ger. Chem. Eng. 1 (1978) 166–174.

[199] J. Choi, J. Son, S. Kim, Generalized Model for Bubble Size and Frequency in Gas-Fluidized Beds, Ind. Eng. Chem. Res. 37 (1998) 2559–2564. doi:10.1021/ie970915v.

[200] R. Beetstra, J. Nijenhuis, N. Ellis, J.R. van Ommen, The influence of the particle size distribution on fluidized bed hydrodynamics using high-throughput experimentation, AIChE J. 55 (2009) 2013–2023. doi:10.1002/aic.11790.

[201] C. Rautenbach, M.C. Melaaen, B.M. Halvorsen, Investigating the influence of fines in fluidized bed reactors using 3D ECT images, in: WIT Trans. Eng. Sci., 2011: pp. 141–151. doi:10.2495/MPF110121.

[202] G.C. Brouwer, E.C. Wagner, J.R. van Ommen, R.F. Mudde, Effects of pressure and fines content on bubble diameter in a fluidized bed studied using fast X-ray tomography, Chem. Eng. J. 207–208 (2012) 711–717. doi:10.1016/j.cej.2012.07.040.

[203] J.F. Davidson, D. Harrison, R. Jackson, Fluidized particles: Cambridge University Press, 1963. 155 pp. 35s, (1964).

[204] R.J. Dry, M.R. Judd, T. Shingles, Bubble Velocities in Fluidized Beds of Fine, Dense Powders, Powder Technol. 39 (1984) 69–75. doi:10.1016/0032-5910(84)85021-4.

[205] S. Liu, Q. Chen, H.G. Wang, F. Jiang, I. Ismail, W.Q. Yang, Electrical capacitance tomography for gas–solids flow measurement for circulating fluidized beds, Flow Meas. Instrum. 16 (2005) 135–144. doi:10.1016/j.flowmeasinst.2005.02.013.

Every reasonable effort has been made to acknowledge the owners of copyright material. I would be pleased to hear from any copyright owner who has been omitted or incorrectly acknowledged.